SANDIA REPORT
SAND2024-14886
Printed October 2024

Sandia National Laboratories

Validation of HyRAM+ Version 5.1 Physics Models

Michael C. Devin, Brian D. Ehrhart, and Ethan S. Hecht

Prepared by
Sandia National Laboratories
Albuquerque, New Mexico 87185
Livermore, California 94550

Issued by Sandia National Laboratories, operated for the United States Department of Energy by National Technology & Engineering Solutions of Sandia, LLC.

NOTICE: This report was prepared as an account of work sponsored by an agency of the United States Government. Neither the United States Government, nor any agency thereof, nor any of their employees, nor any of their contractors, subcontractors, or their employees, make any warranty, express or implied, or assume any legal liability or responsibility for the accuracy, completeness, or usefulness of any information, apparatus, product, or process disclosed, or represent that its use would not infringe privately owned rights. Reference herein to any specific commercial product, process, or service by trade name, trademark, manufacturer, or otherwise, does not necessarily constitute or imply its endorsement, recommendation, or favoring by the United States Government, any agency thereof, or any of their contractors or subcontractors. The views and opinions expressed herein do not necessarily state or reflect those of the United States Government, any agency thereof, or any of their contractors.

Printed in the United States of America. This report has been reproduced directly from the best available copy.

Available to DOE and DOE contractors from

U.S. Department of Energy
Office of Scientific and Technical Information
P.O. Box 62
Oak Ridge, TN 37831

Telephone: (865) 576-8401
Facsimile: (865) 576-5728
E-Mail: reports@osti.gov
Online ordering: http://www.osti.gov/scitech

Available to the public from

U.S. Department of Commerce
National Technical Information Service
5301 Shawnee Road
Alexandria, VA 22312

Telephone: (800) 553-6847
Facsimile: (703) 605-6900
E-Mail: orders@ntis.gov
Online order: https://classic.ntis.gov/help/order-methods



ABSTRACT

The Hydrogen Plus Other Alternative Fuels Risk Assessment Models (HyRAM+) software has seen various improvements and additional physics capabilities since validation against experimental data was last published for HyRAM v3.1. Notably, HyRAM+ now includes four models allowing for the calculation of overpressure resulting from vapor cloud explosions from unconfined jet releases. As with the previous HyRAM validation report, validation data was gathered from available published literature and tested against HyRAM+ capabilities. The validation comparisons include tank blowdown, unignited dispersion jet plume, ignited jet flame, and enclosed accumulation and overpressure. The unconfined overpressure calculations in HyRAM+ v5.1.1 generally show good agreement with many of the experimental data sets for all four unconfined overpressure models, though HyRAM+ overpredicts the experimental data for small and cryogenic hydrogen releases. The comparisons for the other HyRAM+ physics models are largely unchanged from the previously published validation report.

This page intentionally left blank.

ACKNOWLEDGMENT

This work was supported by the U.S. Department of Energy (DOE), Office of Energy Efficiency and Renewable Energy (EERE), Hydrogen and Fuel Cell Technologies Office (HFTO) Safety Codes and Standards sub-program under the direction of Laura Hill. The authors would like to thank Marina Miletic, Kristin Hertz, and Chris LaFleur from Sandia National Laboratories for reviewing this report.

This page intentionally left blank.

CONTENTS

Acknowledgements 5

Acronyms and Terms 17

1. Introduction 19
   1.1. Background and Motivation 19
   1.2. Overview of Changes 19
      1.2.1. Unconfined Overpressure Calculations 19
      1.2.2. Updated Validation 20

2. Methodology 23

3. Results and Discussion 25
   3.1. Blowdowns 25
      3.1.1. Ekoto et al. (2012) 25
      3.1.2. Schefer et al. (2007) 26
      3.1.3. Proust et al. (2011) 27
      3.1.4. Schefer et al. (2006) 28
      3.1.5. Blowdowns Summary 29
   3.2. Unignited Jet Plumes 30
      3.2.1. Molkov (2012) 30
      3.2.2. Houf and Schefer (2008) 32
      3.2.3. Ruggles and Ekoto (2012) 34
      3.2.4. Han et al. (2013) 35
      3.2.5. Unignited Jet Plumes Summary 38
   3.3. Ignited Jet Fires 39
      3.3.1. Ekoto et al. (2014) 39
      3.3.2. Schefer et al. (2006) 39
      3.3.3. Houf and Schefer (2007) 41
      3.3.4. Imamura et al. (2008) 41
      3.3.5. Mogi et al. (2005) 42
      3.3.6. Proust et al. (2011) 43
      3.3.7. Ignited Jet Fires Summary 44
   3.4. Accumulation and Overpressure in Enclosures 46
      3.4.1. Ekoto et al. (2012) 46
      3.4.2. Giannissi et al. (2015) 48
      3.4.3. Merilo et al. (2011) 49
      3.4.4. Bernard-Michel and Houssin-Agbomson (2017) 50
      3.4.5. Accumulation and Overpressure in Enclosures Summary 51
   3.5. Cryogenic Releases 52
      3.5.1. Blowdowns 52
         3.5.1.1. Friedrich et al. (2019) 52
         3.5.1.2. Cryogenic Blowdowns Summary 57

3.5.2. Unignited Jet Plumes . . . 58
3.5.2.1. Xiao et al. (2011) . . . 58
3.5.2.2. Friedrich et al. (2012) . . . 59
3.5.2.3. Hecht and Panda (2019) . . . 59
3.5.2.4. Friedrich et al. (2019) . . . 62
3.5.2.5. Cryogenic Unignited Jet Plumes Summary . . . 66
3.5.3. Ignited Jet Fires . . . 67
3.5.3.1. Panda and Hecht (2017) . . . 67
3.6. Unconfined Overpressure from Jet Releases . . . 69
3.6.1. Bauwens and Dorofeev (2019) . . . 69
3.6.2. Kobayashi et al. (2020) . . . 70
3.6.3. Jallais et al. (2018) . . . 73
3.6.4. Royle and Willoughby (2011) . . . 74
3.6.5. Takeno et al. (2007) . . . 75
3.6.6. Huéscar Medina et al. (2020) . . . 76
3.6.7. Unconfined Overpressure Summary . . . 79

4. Conclusions . . . 81

References . . . 83

Appendix A. Validation Data Input Parameters . . . 87
A.1. Blowdown Input Parameters . . . 87
A.2. Unignited Jets/Gas Plumes Input Parameters . . . 88
A.3. Ignited Jet Fires Input Parameters . . . 92
A.4. Indoor Accumulation and Overpressure Input Parameters . . . 97
A.5. Cryogenic Hydrogen Input Parameters . . . 106
A.5.1. Blowdown . . . 106
A.5.2. Unignited Jet Plumes . . . 107
A.5.3. Ignited Jet Fires . . . 109
A.6. Unconfined Overpressure Input Parameters . . . 110

LIST OF FIGURES

Figure 3-1. Flow rate data during blowdown from Ekoto et al. [21] compared to HyRAM+ model 26
Figure 3-2. Pressure data during blowdown from Schefer et al. [22] compared to HyRAM+ 27
Figure 3-3. Tank pressures and temperatures during blowdown from Proust et al. [23] compared to HyRAM+ model 28
Figure 3-4. Mass flow rate data for a blowdown from Schefer et al. [24] compared to HyRAM predictions 29
Figure 3-5. Centerline mass fractions from data compiled by Molkov [25]. In the legends, T denotes temperature (K), d denotes diameter (mm), and P denotes pressure (MPa). On the x-axis, which is dimensionless, x denotes downstream distance (mm) and ρ denotes density. Solid lines are results from HyRAM+, with the same colors as the conditions in the legends. 32
Figure 3-6. Radial profiles of mass fraction at several downstream locations reported by Houf and Schefer [10] (circles) compared to HyRAM+ (lines). In the legend, z denotes downstream distance and D denotes orifice diameter. 33
Figure 3-7. Inverse centerline mole fraction as a function of downstream distance as reported by Houf and Schefer [10] (circles) and predicted by HyRAM+ (lines) . . 34
Figure 3-8. Inverse centerline mass fraction and half-width as a function of normalized downstream distance from Ruggles and Ekoto [26] (circles) compared to HyRAM+ (lines). z denotes downstream distance from the virtual origin (mm) and r is the radius of the orifice (mm). 35
Figure 3-9. Data for 100–400 bar jets, as reported by Han et al. [27] compared to HyRAM+ 36
Figure 3-10. Inverse centerline mole fraction as reported by Han et al. [27] compared to HyRAM+ 37
Figure 3-11. Heat flux during a blowdown as reported by Schefer et al. [24] (symbols) and predicted by HyRAM+ (lines). x is the downstream distance from the orifice and L_{vis} is the length of the visible flame. 40
Figure 3-12. Data from Houf and Schefer [34] compared to HyRAM+ 41
Figure 3-13. Data from Imamura et al. [35] compared to HyRAM+ 42
Figure 3-14. Radiative heat flux values for different mass flowrates from Mogi et al. [36] compared to HyRAM+, in which d is the diameter of the orifice and L is the distance between the detector and flame axis 43
Figure 3-15. Data from Proust et al. [23] during a 900 bar blowdown compared to HyRAM+ 44
Figure 3-16. Hydrogen mole fraction measurements from different sensors at the ceiling over multiple experiments with and without ventilation from Ekoto et al. [21] compared to HyRAM+ predictions 47
Figure 3-17. Overpressure values from Ekoto et al. [21] (thin, dashed lines) for igniting hydrogen mixtures 3 seconds after the start of the release (ignition at time 0) compared to the predictions from HyRAM+ (thick, solid lines). 47
Figure 3-18. Hydrogen concentration measurements along the ceiling from Giannissi et al. [37] compared with HyRAM+ predictions 48

Figure 3-19. Hydrogen concentrations at different heights over time for tests with different hydrogen flow rates and garage open space from Merilo et al. [38] compared to HyRAM+ predictions. The lower right frame has 0.1 m^3/s mechanical ventilation, which all other frames have only natural ventilation. 49
Figure 3-20. Data from Bernard-Michel and Houssin-Agbomson [39] compared to HyRAM+, showing maximum hydrogen concentration values for different release flow rates and orifice sizes in two enclosures 50
Figure 3-21. Pressure during discharge for vessel (blue) and nozzle (orange) for various pressures, temperatures, and nozzle diameters from Friedrich et al. [42] (solid lines) compared to HyRAM+ (dashed lines) 53
Figure 3-22. Temperature during discharge for vessel top (blue), vessel center (orange), vessel bottom (green), and nozzle (red) as measured by sheathed (thick line) and unsheathed (thin line) thermocouples for varied pressures, temperatures, and nozzle diameters from Friedrich et al. [42] (solid lines) compared to HyRAM+ (dashed lines) 55
Figure 3-23. Tank mass during discharge from Friedrich et al. [42] (solid lines) compared to HyRAM+ (dashed lines) 56
Figure 3-24. Data from Xiao et al. [40] (open circles) compared to HyRAM+ (solid lines) showing inverse centerline mole fraction as a function of normalized downstream distance for four release scenarios, including two cryogenic (80 K) releases. S denotes downstream distance and D_0 denotes the orifice diameter. . 58
Figure 3-25. Data from Friedrich et al. [41] (circles) compared to HyRAM+ (lines) showing centerline mole fraction as a function of normalized downstream distance. z denotes downstream distance, d denotes the orifice diameter, ρ_{amb} denotes ambient fluid density, ρ_0 denotes stagnation density, and ρ_{noz} is the nozzle density. 59
Figure 3-26. Comparison of mole fraction calculated by HyRAM+ (thin, solid lines) to cryogenic hydrogen dispersion data reported by Hecht and Panda [44] and Ehrhart et al. [15] (thick, dashed lines and background shading). In many cases, data was limited to the near-nozzle region, and areas with a white background indicate that there is no experimental data. Mole fractions are indicated on the contours. 60
Figure 3-27. Comparison of temperatures calculated by HyRAM+ (thin, solid lines) to cryogenic hydrogen dispersion data reported by Hecht and Panda [44] and Ehrhart et al. [15] (thick, dashed lines and background shading). In many cases, data was limited to the near-nozzle region, and areas with a white background indicate that there is no experimental data. Temperatures (K) are indicated on the contours. 61
Figure 3-28. Correlation of data to HyRAM+ for all diameters, pressures, temperatures shown in Figures 3-26 and 3-27 (each point for counting purposes is a 0.5 mm $\times$ 0.5 mm pixel) 62

Figure 3-29. Data from Friedrich et al. [42] (solid lines) compared to HyRAM+ (dashed lines) showing molar concentrations during discharge. Each color indicates a different (r, z) location, where r is the distance from the centerline and z is the downstream distance: (0 cm, 150 cm) in blue, (0 cm, 100 cm) in orange, (0 cm, 50 cm) in light gray, and (10 cm, 100 cm) in dark gray. The thin light gray line denotes a different cut on the extraction probe at the (0 cm, 50 cm) location. . . 63
Figure 3-30. Data from Friedrich et al. [42] (solid lines) compared to HyRAM+ (dashed lines) showing temperatures outside the vessel during discharge. Each color indicates a different (r, z) location, Each color indicates a different (r, z) location, where r is the distance from the centerline and z is the downstream distance: (2 cm, 20 cm) in dark blue, (0 cm, 25 cm) in orange, (5 cm, 50 cm) in light gray, (5 cm, 50 cm) in dark gray, and (0 cm, 175 cm) in light blue. 65
Figure 3-31. Comparison of flame length calculated by HyRAM+ to those measured by Panda and Hecht [43] 67
Figure 3-32. Comparison of heat flux (Q) at various distances calculated by HyRAM+ and measured by Panda and Hecht [43] 68
Figure 3-33. Peak unconfined overpressure predictions for different sensors from experiments cited in Bauwens and Dorofeev [18] (circles) compared to HyRAM+ predictions (lines) 70
Figure 3-34. Peak unconfined overpressure predictions comparing sensors in Kobayashi et al. [45] (circles) to HyRAM+ predictions (lines) 71
Figure 3-35. Peak unconfined overpressure predictions comparing calculations from Jallais et al. [19] matching the Jallais method (circles) to HyRAM+ predictions (lines) 73
Figure 3-36. Peak unconfined overpressure predictions comparing sensors in Takeno et al. [47] (circles) to HyRAM+ predictions (lines) for 1.0 mm and 2.0 mm nozzle diameters 75
Figure 3-37. Peak unconfined overpressure predictions comparing sensors in Takeno et al. [47] (circles) to HyRAM+ predictions (lines) for 5.0 mm and 10.0 mm nozzle diameters 76
Figure 3-38. Visualization of the sensor positions and the measured and calculated peak overpressures (circles) with the gray triangle showing the release direction; data from Huéscar Medina et al. [48] 78

This page intentionally left blank.

LIST OF TABLES

Table 3-1. Blowdown Validation Data Sources 25
Table 3-2. Unignited Jet Validation Data Sources 30
Table 3-3. Flame Validation Data Sources 39
Table 3-4. Flame Length and Heat Flux Results from Ekoto et al. [13] compared to HyRAM+ 39
Table 3-5. Overpressure/Accumulation Validation Data Sources 46
Table 3-6. Cryogenic Blowdown Validation Data Sources 52
Table 3-7. Cryogenic Unignited Jet Plumes Validation Data Sources 58
Table 3-8. Cryogenic Ignited Jet Plumes Validation Data Sources 67
Table 3-9. Unconfined Overpressure Validation Data Sources 69
Table 3-10. Comparison of distances to a 1 kPa overpressure found in Kobayashi et al. [45] to the unconfined overpressure methods in HyRAM+. The HyRAM+ calculations use the calculated origin assumption. These data exclude the Bauwens method, which is unable to calculate overpressure for these inputs 72
Table 3-11. Comparison of peak unconfined overpressure (abbreviated as "OP") predictions from tests in Royle and Willoughby [46] with HyRAM+ calculations. The HyRAM+ calculations consider both the "origin at orifice" (OAO) and "calculated origin" (CO) options for origin location, separated by a "|" 74
Table A-1. Ekoto et al. [21] Figure 3 Input Parameters 87
Table A-2. Schefer et al. [22] Figure 4 Input Parameters 87
Table A-3. Proust et al. [23] Figure 4 Input Parameters 87
Table A-4. Schefer et al. [24] Figure 3b Input Parameters 87
Table A-5. Molkov [25] Table 5-3 Input Parameters 88
Table A-6. Houf and Schefer [10] Figure 5 Input Parameters 88
Table A-7. Houf and Schefer [10] Figure 8 Input Parameters 89
Table A-8. Houf and Schefer [10] Figure 9 Input Parameters 89
Table A-9. Ruggles and Ekoto [26] Figure 7 Input Parameters 89
Table A-10. Han et al. [27] Figure 3 Input Parameters 90
Table A-11. Han et al. [27] Figure 6 Input Parameters 90
Table A-12. Han et al. [27] Figure 7 Input Parameters 90
Table A-13. Han et al. [27] Figure 8 Input Parameters 91
Table A-14. Ekoto et al. [13] Table 2 Input Parameters 92
Table A-15. Schefer et al. [24] Figure 8 Input Parameters 93
Table A-16. Houf and Schefer [34] Figure 5 Input Parameters 93
Table A-17. Houf and Schefer [34] Figure 6 Input Parameters 94
Table A-18. Imamura et al. [35] Table 2 Input Parameters 95
Table A-19. Imamura et al. [35] Table 2 Input Parameters 95
Table A-20. Mogi et al. [36] Figure 9 Input Parameters 96
Table A-21. Proust et al. [23] Figure 8 Input Parameters 96
Table A-22. Proust et al. [23] Figure 10 Input Parameters 96
Table A-23. Ekoto et al. [21] Figure 9 Input Parameters 97
Table A-24. Ekoto et al. [21] Figure 9 Sensor Locations 98
Table A-25. Ekoto et al. [21] Figure 14 Input Parameters 99

Table A-26. Giannissi et al. [37] Figure 7 Input Parameters 100
Table A-27. Merilo et al. [38] Figure 2 Overall Input Parameters 101
Table A-28. Merilo et al. [38] Figure 2 Sub-Figure Specific Input Parameters 102
Table A-29. Merilo et al. [38] Figure 6a Input Parameters 103
Table A-30. Bernard-Michel and Houssin-Agbomson [39] Figure 7 Input Parameters 104
Table A-31. Bernard-Michel and Houssin-Agbomson [39] Figure 9 Input Parameters 105
Table A-32. Friedrich et al. [42] Dataset Input Parameters 106
Table A-33. Xiao et al. [40] Figure 3 Input Parameters 107
Table A-34. Friedrich et al. [41] Figure 5 Input Parameters 107
Table A-35. Hecht and Panda [44] Figure 10 Input Parameters 108
Table A-36. Panda and Hecht [43] Table 3 Input Parameters 109
Table A-37. Bauwens and Dorofeev [18] Figure 9 Input Parameters 110
Table A-38. Kobayashi et al. [45] Figure 8 Input Parameters 110
Table A-39. Kobayashi et al. [45] Table 1 Input Parameters (orifice properties and locations provided in Table 3-10) 111
Table A-40. Royle and Willoughby [46] Table 1 Input Parameters (orifice diameters provided in Table 3-11) 111
Table A-41. Huéscar Medina et al. [48] Figure 148 Input Parameters 111
Table A-42. Jallais et al. [19] Figure 22 & Table 2 Input Parameters 112
Table A-43. Takeno et al. [47] Figures 13 & 16 Input Parameters, 1.0 & 2.0mm Nozzles . . . 113
Table A-44. Takeno et al. [47] Figures 13 & 16 Input Parameters, 5.0 & 10.0mm Nozzles . . 114

EXECUTIVE SUMMARY

The Hydrogen Plus Other Alternative Fuels Risk Assessment Models (HyRAM+) software version 5.1 features changes to its physics capabilities since the last validation report was published following the release of HyRAM version 3.1. Two significant physics additions have been made during this time:

- Assessment of alternative fuels besides hydrogen, including methane, propane, and blends of multiple fuels
- Calculating the overpressure resulting from delayed ignition of jet releases in unconfined environments

As the HyRAM/HyRAM+ code base has evolved since HyRAM 3.1 to accommodate this additional functionality, this report updates the previous HyRAM validation efforts by rerunning and analyzing validation tests using the current version of the software. These validation data sets include HyRAM+ physics models for tank blowdown, unignited dispersion jet plume, ignited jet flame, and accumulation and overpressure inside an enclosure. Additionally, a new section has been added to this report to validate the four unconfined overpressure physics models added to HyRAM+ since the previous validation report: the Baker-Strehlow-Tang (BST) method, the TNT equivalence method, the Bauwens method, and the Jallais method. These models are compared to experimental data from literature in an analogous manner to the other sections of the report to demonstrate and compare the accuracy of the models.

The blowdown (emptying) of high-pressure, room-temperature tanks predicted by HyRAM+ are compared to four literature sources in Section 3.1. Data was gathered for hydrogen tanks with initial pressures of 13.45 MPa, 15.5 MPa, 43.1 MPa, and 90 MPa. HyRAM+ predicts very similar times to empty compared to the experiments, though flow rates are initially overpredicted slightly before leveling off to line up with the experimental data. The tank temperature was also monitored in one experiment, and HyRAM+ predicted much lower tank temperatures than the experimental measurements. This is likely due to gas mixing within the tank and heat loss through the tank walls, which are neglected in HyRAM+.

Mean concentrations (mole and mass fractions) during the dispersion of hydrogen are compared for a range of release scenarios in Section 3.2. HyRAM+ predicts the mean centerline mole fractions with very good agreement with experimental data, though HyRAM+ predicts far narrower Gaussian dispersion profiles compared to experiments. Improved tuning of empirical parameter values within the HyRAM+ model may improve this agreement, but this needs to be explored further.

Flame lengths and heat fluxes for ignited high-pressure hydrogen diffusion flames are predicted and compared to a variety of literature data in Section 3.3. HyRAM+ accurately predicts the flame lengths of hydrogen diffusion flames up to 900 bar, with some minor conservatism for the corresponding heat flux predictions, particularly for releases from larger nozzles.

Accumulation within an enclosure and the overpressure that would result if the accumulated hydrogen were to ignite are compared to several literature sources in Section 3.4. HyRAM+

predicts concentrations and overpressures that are similar to literature data, but there is a fairly wide variability in accuracy depending on the experimental setup. HyRAM+ also conservatively predicts the overpressure that would result from the ignition of an accumulated mixture within an enclosure both with and without ventilation, though there was only a single literature source for this comparison.

HyRAM+ is compared to literature data for cryogenic releases of hydrogen in Section 3.5. Similar to the room-temperature blowdown simulations, HyRAM+ fairly accurately predicts the pressure decay as a tank is emptied, but predicts temperatures in the tank that are much lower than the measured experimental data. HyRAM+ also predicts significant differences in the pressure and temperature at the orifice versus the tank, while the pressure and temperature measured at the orifice and tank in the experiments were similar. HyRAM+ predicts centerline concentration decay and even two-dimensional near-field concentration fields of unignited jets accurately. HyRAM+ tends to slightly overpredict concentration in most cases, while some experimental temperature measurements were higher and some lower than those predicted by HyRAM+. In most of the experiments, the temperature measurements had more uncertainty than the concentration measurements. Similar to the warm releases, HyRAM+ also predicts slightly longer visible flame lengths and heat fluxes than were measured experimentally.

Finally, overpressures resulting from the ignition of unconfined jet releases of hydrogen are compared to literature in Section 3.6. The test conditions from the experiments vary considerably, complicating comparisons across literature sources and to HyRAM+ results. However, HyRAM+ generally shows moderate overprediction against the majority of the validation data, providing some conservatism to the calculations. HyRAM+ severely overpredicts overpressure within about 5 m of the ignition point and for some releases from nozzles less than 1.0 mm in diameter, though the latter finding is based on a small number of data sources and requires further investigation. The Bauwens method generally performs the best except for very small nozzle sizes, while the TNT equivalence method consistently has the greatest amount of overprediction. HyRAM+ also shows larger differences for most overpressures for very short delay ignitions (< 1 s) due to the assumption that the jet is fully developed at time of ignition.

Overall, the validation results are generally unchanged between HyRAM 3.1 and HyRAM+ 5.1 for the physics models published in the previous HyRAM validation report. The new unconfined overpressure models generally provide a reasonable amount of conservatism compared to most experimental test data, though there are more significant differences for predictions with very short ignition delays and/or within about 5 m of the ignition location. Further validation and model improvements should be performed as additional literature emerges for these releases to reduce the amount of conservatism and provide greater precision in the software for its users.

ACRONYMS AND TERMS

BST Baker-Strehlow-Tang

DOE Department of Energy

EERE Office of Energy Efficiency and Renewable Energy

HFTO Hydrogen and Fuel Cell Technologies Office

HyRAM Hydrogen Risk Assessment Models

HyRAM+ Hydrogen Plus Other Alternative Fuels Risk Assessment Models

LFL lower flammability limit

NIST National Institute of Standards and Technology

PreSLHy Prenormative Research for Safe Use of Liquid Hydrogen

REFPROP Reference Fluid Thermodynamic and Transport Properties Database

This page intentionally left blank.

1. INTRODUCTION

1.1. Background and Motivation

The Hydrogen Risk Assessment Models (HyRAM) software and its documentation was originally published in 2015 (version 1.0) [1], updated in 2017 (version 1.1) [2], 2019 (version 2.0) [3], 2020 (version 3.0) [4], and 2021 (version 3.1) [5]. More recent versions, rebranded as Hydrogen Plus Other Alternative Fuels Risk Assessment Models (HyRAM+), to represent new software capabilities, were published in 2021 (version 4.0) [6], 2022 (versions 4.1 and 5.0) [7, 8], and 2023 (version 5.1) [9].The software features both quantitative risk assessment and physics models for releases of hydrogen, methane, propane, or a blended fuel mixture (e.g., natural gas, natural gas and hydrogen blends). The physics models can be used to simulate the behavior of a gaseous, saturated vapor, or saturated liquid release for unignited jet plumes, ignited jet flames, accumulation in an enclosure followed by ignition, and the ignition of an unconfined buoyant jet. The unignited and ignited jets are based on models developed, validated, and published at Sandia National Laboratories, although many of the underlying models were developed elsewhere. Specifically, the unignited jet plume follows a one-dimensional model described by Houf and Schefer [10] (versions $\leq$ 2.0) and Houf and Winters [11, 12]. A similar model to the jet/plume is used to simulate a flame as described by Ekoto et al. [13]. The heat flux from curved flames uses a weighted multi-source model, similar to that described by Hankinson and Lowesmith [14], to calculate the total heat flux at each point along the flame length. Since version 3.0, HyRAM/HyRAM+ uses a real gas equation of state to relate pressure, temperature, and volume in regions where real gas effects are present. This equation of state is accurate for high pressures and low temperatures, with good agreement between experimental data and simulations.

With the addition of alternative fuels, fuel mixtures, and unconfined overpressure capabilities, there have been substantial physics modifications to the HyRAM+ source code since the last validation report was published following the release of HyRAM version 3.1 [15]. The comparisons to the experimental data published in the previous validation report have been added as automated regression tests to ensure future changes to the source code do not reduce the accuracy of the physics modules compared to experimental data. Validation of the models for propane and methane as alternative fuels in HyRAM+ version 4.0 has been performed previously, and can be found in Guo et al. [16]. This report presents an update to [15] for HyRAM+ version 5.1, including all of the comparisons to the experimental data included in the prior validation report updated for the newer version of the software. Additionally, Section 3.6 has been added to validate the unconfined overpressure module introduced in HyRAM+ version 4.0 against data published in the literature.

1.2. Overview of Changes

1.2.1. Unconfined Overpressure Calculations

Research shows that overpressures can be observed if a fuel ignites following a delay after release, even if the release is unconfined; i.e., a vapor cloud explosion. HyRAM+ currently has three

physics models for estimating overpressure from vapor cloud explosions available to users, and a fourth method in the Python backend:

- The Baker-Strehlow-Tang (BST) method. This method uses the flame speed and blast curve lines relative to scaled distance to map the overpressure and impulse of the explosion. In HyRAM+, the flame speed relative to the Mach number is a user input. The blast curves included in HyRAM+ and a more detailed description of the method are found in Tang and Baker [17].
- The TNT equivalence method. This method calculates the power of the explosion, and therefore the resultant overpressure, as being proportionate to the amount of ignited fuel and the corresponding energy released from TNT. The equivalency factor, F_{equiv}, is an optional user input that is set to 3% by default.
- The method derived in Bauwens and Dorofeev [18] is referred to as the "Bauwens method" hereafter. Derived specifically for the ignition of hydrogen jets, it is based on research identifying far reduced mass participating in detonation due to critical conditions required to propagate detonation waves. This method analyzes the cell size of the propagating detonation wave to calculate the number of transverse waves it is able to sustain to assess the stability of the waves, which provides a more precise means of calculating the fuel concentration being consumed in the explosion.
- An extension of the BST method derived in the "simple engineering model" from Jallais et al. [19] is referred to as the "Jallais method" hereafter. This method uses the BST method above, but was tuned for hydrogen by calculating the flammable mass from limits that are not the flammability limits, but rather 10-75% by volume, and relating the Mach flame speed to the release flow rate with three cutoffs: 100 m/s, $\dot{m} < 0.5$ kg/s; 140 m/s, $0.5 \leq \dot{m} < 1$ kg/s; 240 m/s, $\dot{m} \geq 1$ kg/s. Note this method is only available in the Python backend of HyRAM+, and the modifications to the BST are not documented specifically in [9]. However, the method is included in the automated regression tests in HyRAM+, and is added to this section for completeness.

These methods are described in greater detail in the HyRAM+ version 5.1 Technical Reference Manual, Section 3.4.5 [9].

1.2.2. Updated Validation

This report updates the validation comparison effort performed previously [15] to version 5.1 of HyRAM+. All the prior tests against validation data in the previous report are repeated here with the newer release of HyRAM+, including tank blowdown, unignited dispersion jet plume, ignited jet flame, and accumulation and overpressure inside an enclosure.

The previous validation report focused on comparing results from HyRAM version 2 to version 3 due to the change from the Abel-Noble equation of state to the real gas equation of state. The intent of this report is to compare the HyRAM+ physics models to experimental data without explicitly comparing versions of HyRAM+. Except for Section 3.6 documenting the new unconfined

overpressure tests, much of the language in this report that was previously included in [15] has only been lightly modified from the earlier report unless noteworthy changes are evident.

This page intentionally left blank.

2. METHODOLOGY

Literature sources of experimental data for validation comparison were identified for each of the different physics models within HyRAM/HyRAM+. These sources include the original validation data listed in the HyRAM/HyRAM+ technical reference manuals [1, 2, 4, 5, 7–9] and the sources cited therein. A literature search was also performed to identify additional sources, including those that were not published when the original model validations were performed (prior to HyRAM version 1.0). Once the literature data sources for each different physics model were identified, the data from the graphs were digitized using an online tool, WebPlotDigitizer [20]. Input values for the HyRAM+ models were determined from descriptions in literature sources. All of the input parameter values for all comparisons are given in Appendix A.

Key outputs from each model were compared to the experimental results. For the blowdown model, the mass flow rate, pressure drop, and temperature in the tank as a function of time were compared. The plume/jet model predicts two-dimensional fields of velocity, mole/mass fractions, and temperatures. Experimental data is commonly plotted as centerline (or inverse centerline) mole/mass fraction and/or velocity, and radial profiles of mole/mass fraction and/or velocity. The HyRAM+ flame model predicts the trajectory and temperature of a flame, including the flame length. The radiant heat flux from a flame is also calculated by the flame model, which is a key parameter in estimating the risk from a hydrogen leak. The indoor accumulation and overpressure model predicts the concentration within a uniform layer at the ceiling of an enclosure as a function of time, along with the overpressure generated in the enclosure following ignition of that mixture. The unconfined overpressure models predict the concentration as a function of straight-line distance with respect to the position from the orifice. Each of these key parameters were compared to experimental data.

Comparisons were made against HyRAM+ version 5.1.1. The source code for HyRAM+ v5.1.1 is available on the public GitHub repository at
`https://github.com/sandialabs/hyram/releases/tag/v5.1.1`.

This page intentionally left blank.

3. RESULTS AND DISCUSSION

This section shows comparisons of HyRAM+ 5.1.1 to relevant experimental data available in published literature to demonstrate the level of agreement. The following sub-sections include comparisons from multiple literature sources with different models within HyRAM+, including blowdown/mass flow, unignited plumes, ignited jet fires, accumulation/overpressure in an enclosure, and unconfined overpressure.

3.1. Blowdowns

A "blowdown" is the process of a pressure vessel emptying due to a leak or release. After the validation plots were identified and digitized, the input parameters for each table or figure was identified from each reference. Table 3-1 lists the tables and figures that were digitized and used as validation for the blowdown model in the listed corresponding report sections.

Table 3-1 Blowdown Validation Data Sources

Author(s)	Year	Figure Number	Report Section
Ekoto et al. [21]	2012	Figure 3	3.1.1
Schefer et al. [22]	2007	Figure 4	3.1.2
Proust et al. [23]	2011	Figure 4	3.1.3
Schefer et al. [24]	2006	Figure 3b	3.1.4

3.1.1. Ekoto et al. (2012)

Blowdown conditions described in the Ekoto et al. [21] paper included a hydrogen tank release with initial conditions: tank volume 3.63 L, tank pressure 13.45 MPa, tank temperature 297 K, hydrogen mass 0.00363 kg, release diameter 3.56 mm, and a discharge coefficient of 0.75. An apparatus was designed and constructed to mimic a hydrogen forklift release. The release enclosure was 34.3 cm long, 34.3 cm wide, and 43.5 cm high and elevated 6.4 cm off the facility floor. The release area within the enclosure was a 13.1 cm by 13.1 cm square. The experiment was a blowdown of a commercial six-pack of hydrogen tanks. The full experimental setup is described in Section 3.4. A comparison to HyRAM+ is shown in Figure 3-1.

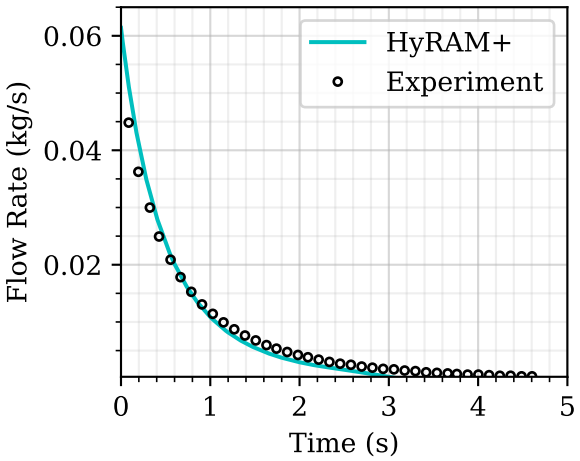


Figure 3-1 Flow rate data during blowdown from Ekoto et al. [21] compared to HyRAM+ model

The mass flow rate is plotted as a function of time. HyRAM+ predicts initial flow rates of approximately 0.06 kg/s, with a blowdown time just over 3 seconds. The initial experimental data-point is approximately 0.45 kg/s, and the blowdown lasts nearly 5 seconds. Overall, the HyRAM+ predicted mass flow rates and blowdown time are similar to the experiment, with differences likely due to the assumption of isentropic flow from an adiabatic tank in HyRAM+.

3.1.2. Schefer et al. (2007)

The experimental setup described by Schefer et al. [22] was designed to characterize high pressure, under-expanded hydrogen jet flames. Eight hydrogen tanks totaling 174.4 ft^3 (4938 L) contained a nominal pressure of 431 bar each. Only two hydrogen tanks were used for the blowdown and three flame tests, the remaining six tanks remained closed. The exit diameter was 0.508 cm. Hydrogen was released vertically using a stagnation chamber. Cameras were used to measure the visible flame length, which were placed 14 and 15 meters away from the jet centerline. Radiometers were places around the flame to measure the radiative flux of the flame. The tank pressure as a function of time is shown in Figure 3-2. It should be noted that the data for the full figure and zoomed axis in Figure 3-2 appear to be different. This is because the source figure for these data in Schefer et al. [22] does not clearly show data near a time of 0 seconds in the main figure, but the data are more clearly visible in the zoomed axis for the first 10 seconds of release.

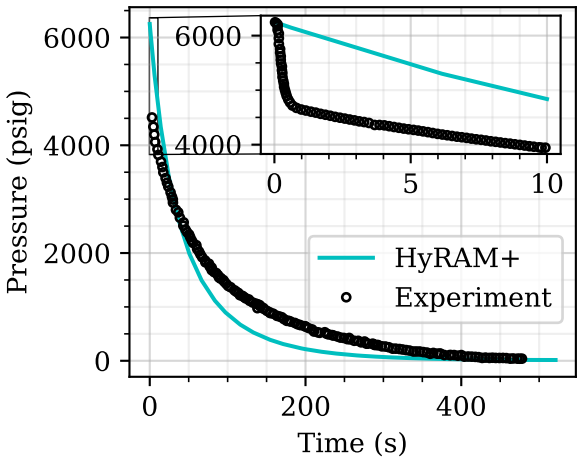


Figure 3-2 Pressure data during blowdown from Schefer et al. [22] compared to HyRAM+

As shown in the smaller zoomed axis of the first 10 seconds of the release, both HyRAM+ and the experiment start at approximately 6200 psig (42.7 MPag), but the experiment shows a rapid drop in pressure over the first 0.5 seconds to around 4500 psig (31.0 MPag), while the HyRAM+ pressure drop is more moderate. The authors [22] speculate that this initial rapid pressure drop is due to the flow entering the stagnation chamber, an aspect not captured in the HyRAM+ model. Overall, both the experiment and HyRAM+ predict the blowdown to last for around 500 seconds exhibit similar rates of pressure decrease.

3.1.3. Proust et al. (2011)

Proust et al. [23] performed horizontal release experiments using a 25 L hydrogen tank reservoir with release diameters between 1 mm and 3 mm. A blowdown was reported with an initial pressure of 90 MPa through a 2 mm diameter orifice. The full experimental setup is described in Section 3.3. A comparison of the experimental blowdown to the HyRAM+ models is shown in Figure 3-3.

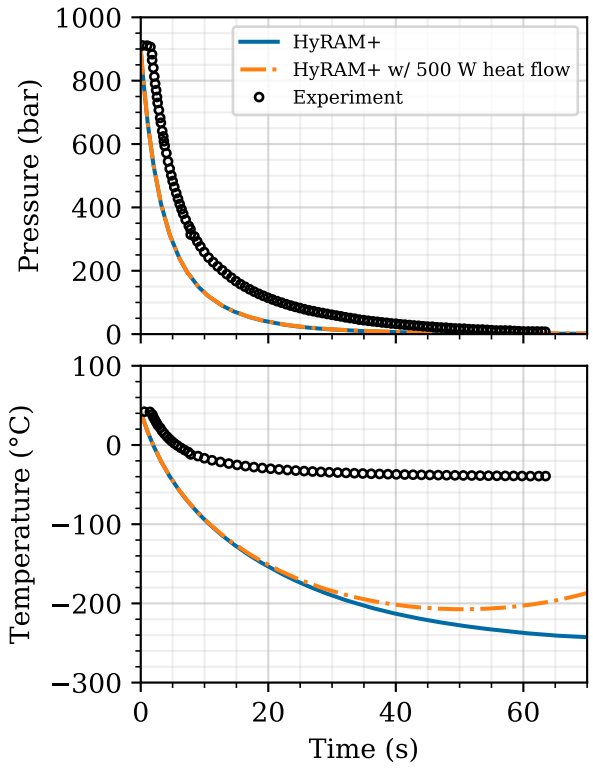


Figure 3-3 Tank pressures and temperatures during blowdown from Proust et al. [23] compared to HyRAM+ model

The experiment and models show the pressure dropping from 900 bar to atmospheric pressure over approximately 65 seconds, with HyRAM+ predicting a faster initial pressure drop. The bottom frame of Figure 3-3 shows temperatures predicted by HyRAM+ are much lower than those measured experimentally, with minimum temperature near -200°C and -30°C respectively. HyRAM+ assumes the tank to be adiabatic in this comparison, which is a potential reason for this discrepancy. To test this, we added a heat flux of 500 W to the tank definition in HyRAM+ and reran the simulation. However, the predicted tank temperatures are still well below those measured experimentally even with the added heat flux. The temperature was measured just upstream of the orifice, and it is possible that the gas in the reservoir was not well-mixed in the experiment, which is an assumption made by HyRAM+. These differences between the data and predictions indicate that while HyRAM+ predicts mass flow rates and pressure histories during a blowdown accurately, it is not accurate at predicting tank temperatures. Gas temperatures inside a tank during a blowdown are generally not used in risk or hazard assessments, so this is not expected to significantly affect hazard analyses.

3.1.4. Schefer et al. (2006)

Schefer et al. [24] report a tank blowdown starting at a total pressure of 2250 psia (15.5 MPaa) through a 3.175 mm orifice diameter. Other experimental details are included in Section 3.3.

Comparisons of the blowdown to HyRAM+ are shown in Figure 3-4.

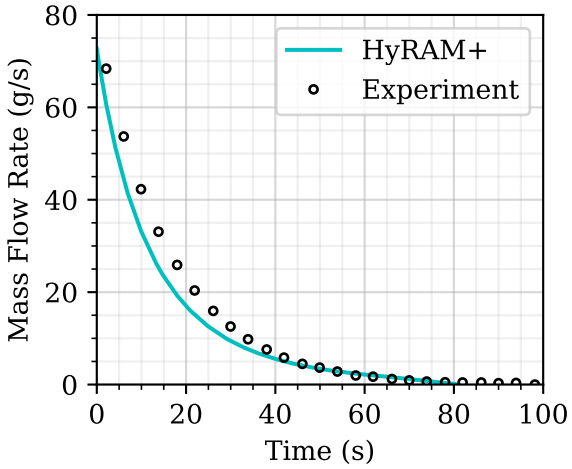


Figure 3-4 Mass flow rate data for a blowdown from Schefer et al. [24] compared to HyRAM predictions

The mass flow rates predicted by HyRAM+ are very similar to those reported in the paper, though HyRAM+ predicts slightly faster decasy at the start of the blowdown compared to the experiment. HyRAM+ predicts a total blowdown duration of just over 80 s compared to 100 s for the experimental blowdown.

3.1.5. Blowdowns Summary

Overall, the blowdown model in HyRAM+ predicts similar flow rate and pressure decay compared to experimental measurements. The model is unable to capture the tank temperatures that were experimentally measured by Proust et al. [23] likely due to the model assumption of a well-mixed, adiabatic (or constant heat flux) tank. More complex modeling is required to accurately capture tank blowdown physics (i.e., computational fluid dynamics). The HyRAM+ models can be used confidently to predict pressure and mass flow histories during a blowdown.

3.2. Unignited Jet Plumes

Table 3-2 lists the tables and figures that were used as validation for the unignited jet model in HyRAM+ and their corresponding report sections.

Table 3-2 Unignited Jet Validation Data Sources

Author(s)	Year	Figure/Table Number	Report Section
Molkov [25]	2012	Table 5-3	3.2.1
Houf and Schefer [10]	2008	Figures 5, 8, 9	3.2.2
Ruggles and Ekoto [26]	2012	Figure 7	3.2.3
Han et al. [27]	2013	Figures 3, 6, 7, 8	3.2.4

3.2.1. Molkov (2012)

Molkov [25] compiled data from experiments conducted by other researchers to assess the similarity law for expanded and under-expanded jets. A brief description of the original works are provided here; more details can be found in Section 5.3.3 of the book *Fundamentals of Hydrogen Safety Engineering I* by Molkov [25]. Six previous experiments were compared:

- Chaineaux et al. [28] conducted experiments to measure the axial concentration decay of hydrogen and methane horizontal jets. The tank volume was 0.12 m^3 with an initial pressure of 10 MPa released 2.2 m above the ground, with orifice diameters of 5 mm, 12 mm, and 24 mm for various tests.
- Kuznetsov [29] conducted experiments to analyze hydrogen distribution of horizontal jets inside a compartment of total volume of 160 m^3. The test initial pressures ranged from 2–26 MPa and orifice diameters ranging between 0.16 mm to 1 mm. A flow rate controller was used to keep a constant mass flow rate. Hydrogen concentration and flow velocity measurements were captured at 0.75 m, 1.5 m, and 2.25 m from the nozzle for eight different experimental setups.
- Okabayashi et al. [30] conducted five different experiments to measure the average volumetric concentrations of hydrogen along the jet. The releases were conducted horizontally 1 m above the ground, with various orifice diameters and pressures. The orifice diameters include 0.25 mm, 0.5 mm, and 1 mm at and initial pressure of 40 MPa. For the 2 mm release two initial pressures of 20 MPa and 40 MPa were used. Concentrations were measured at 4 m, 6 m, 8 m, 11 m, 15 m, 20 m, 30 m, and 50 m from the release point. Not all data points from these experiments are captured in Table 5-3 of Molkov's book [25], so our comparison uses the data points directly from Okabayashi et al. [30], which include the minimum and maximum results for each experimental setup as well as intermediate results for the 1 mm and 2 mm orifices at 40 MPa.
- Ruffin et al. [31] conducted experiments measuring the axial concentration decay of sub-sonic hydrogen and methane jets. Ruffin conducted four experiments with orifice diameters of 25 mm, 50 mm, 75 mm, and 100 mm on a 5 m^3 tank with an initial pressure of

4 MPa and an initial temperature of 288 K. The data points were collected at 2 seconds after the release at pressures of 1.79 MPa, 0.746 MPa, and 0.257 MPa.

- Shirvill et al. [32] conducted experiments for hydrogen concentration with a high pressure system at 17.3 MPa. The experiments were conducted with discharge pressures of 1.1–15.1 MPa and orifice diameters of 1–12 mm. The releases were conducted horizontally at 1.5 m above the ground. Hydrogen concentrations were measured at 1.0 m, 1.5 m, and 2.0 m along the jet, with the maximum and minimum concentrations at each position included in Table 5-3 of Molkov.
- Veser et al. [33] conducted experiments to determine the hydrogen distribution of horizontal hydrogen jets, with orifice diameters of 1 mm, 2 mm, or 4 mm and initial pressures between 0.5 MPa and 6.0 MPa, released at 0.9 m above the ground. Gas was released at temperatures of 35 K, 65 K, 80 K, and 298 K, and the temperature and concentration were measured along the jet.

The centerline mass fractions reported by Molkov [25] based on different literature experiments are shown in Figure 3-5. Note that some subfigures in Figure 3-5 have overlapping solid lines for HyRAM+, making them difficult to distinguish.

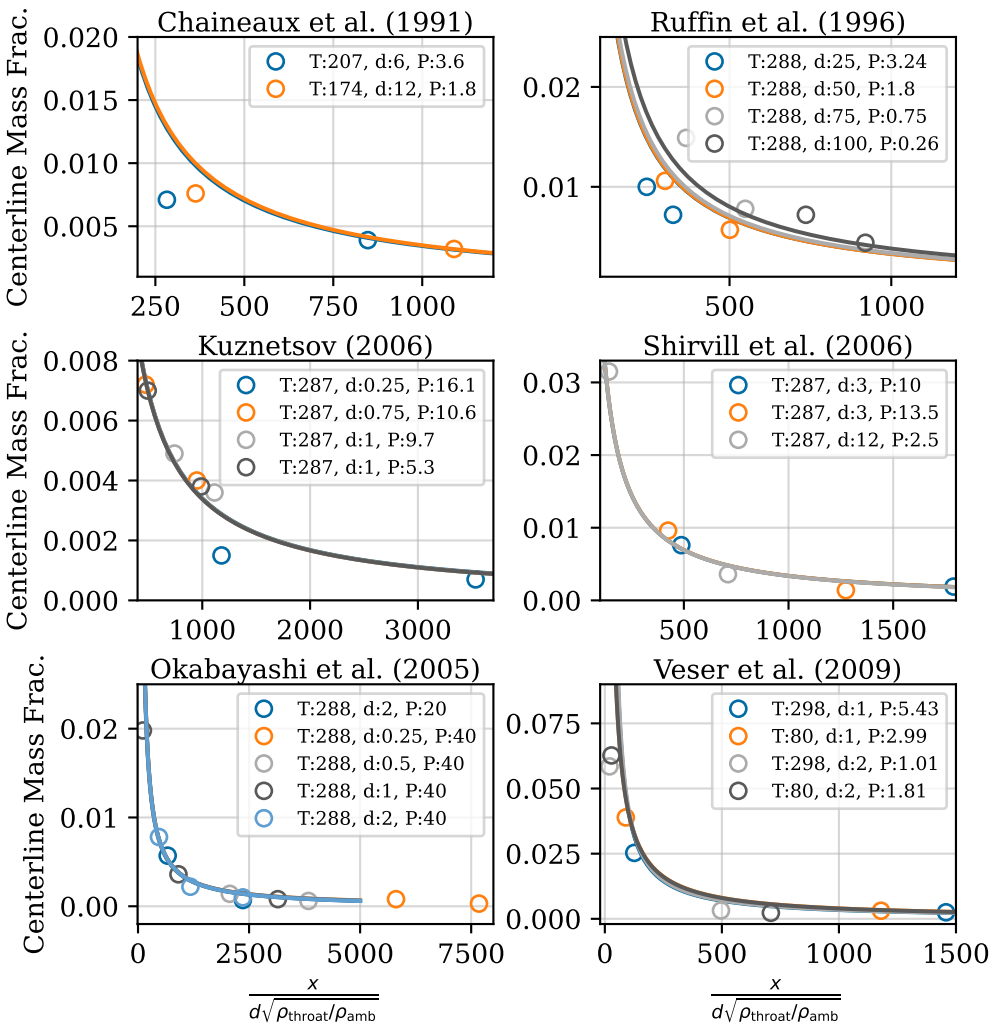


Figure 3-5 Centerline mass fractions from data compiled by Molkov [25]. In the legends, T denotes temperature (K), d denotes diameter (mm), and P denotes pressure (MPa). On the x-axis, which is dimensionless, x denotes downstream distance (mm) and ρ denotes density. Solid lines are results from HyRAM+, with the same colors as the conditions in the legends.

The temperature of these releases range from 80 K to 288 K, with pressures from 1 MPa to 40 MPa. HyRAM+ agrees with the experimental data well, though the model slightly underpredicts the centerline mass fractions for some of the Ruffin et al. [31] and Kuznetsov [29] data.

3.2.2. Houf and Schefer (2008)

Houf and Schefer [10] designed an experiment to measure the leak rate, buoyant jet shape, and concentration field for slow leaks. A planar laser-Rayleigh scattering diagnostic was used to measure hydrogen leak flow. The leak diameter of 1.905 mm was used and the hydrogen was released vertically. The flow conditions were at ambient temperature (294 K) and pressure

(100 kPa). Figure 3-6 shows a comparison of mass fraction cross-sections at various normalized downstream distances.

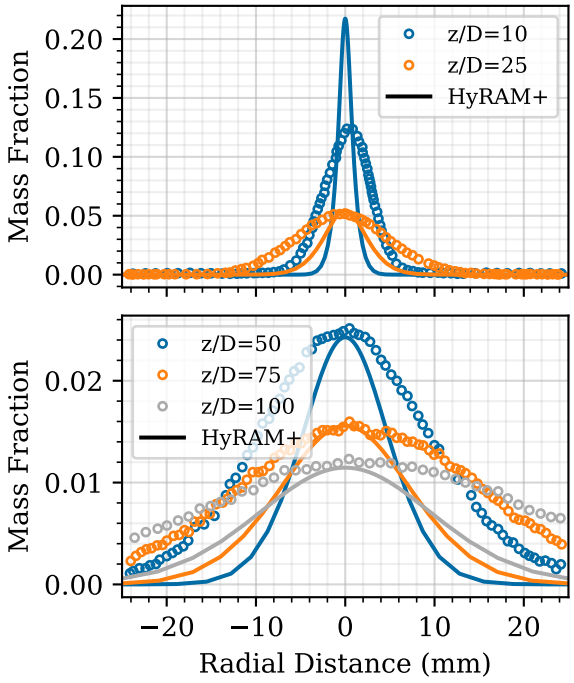
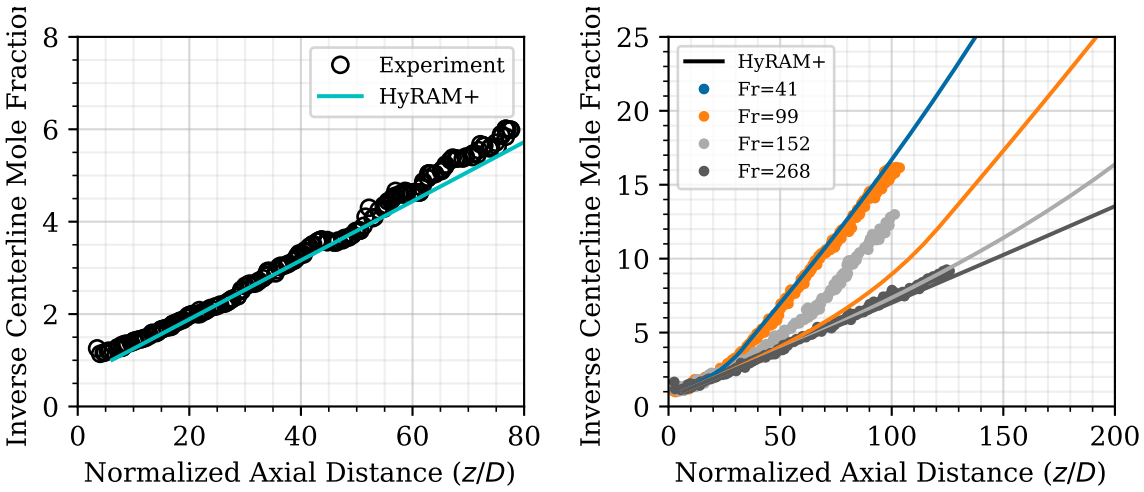


Figure 3-6 Radial profiles of mass fraction at several downstream locations reported by Houf and Schefer [10] (circles) compared to HyRAM+ (lines). In the legend, z denotes downstream distance and D denotes orifice diameter.

HyRAM+ overpredicts the centerline mass fraction significantly downstream at $z/D = 10$, though the centerline mass fractions align more closely for further downstream distances. There is some discrepancy between the radial profile in HyRAM+ to the experimental data for all downstream distances. Predictions for radial profiles could be improved with better tuning of the empirical parameters for entrainment and spreading ratio in the HyRAM+ model, which will be explored in a future version of the software.

Centerline inverse mole fractions are shown as a function of distance, for a Froude number of 268 in Figure 3-7a. The centerline concentrations is well predicted across all axial distances.



(a) Zoomed view for a densimetric Froude number of 268

(b) Several densimetric Froude numbers

Figure 3-7 Inverse centerline mole fraction as a function of downstream distance as reported by Houf and Schefer [10] (circles) and predicted by HyRAM+ (lines)

In Figure 3-7b, inverse centerline mole fractions for a Froude number of 268, as well as several lower Froude numbers are shown. In the case of the smaller Froude numbers, buoyancy begins to play a role in the decay of the centerline concentration. While Houf and Schefer [10] report that the data is for Froude numbers of 99, 152, and 268, we suspect that Figure 9 in their work may have been mislabeled, as the paper also discusses releases with a smaller Froude number of 41. The HyRAM+ simulation for the Froude number of 41 agree well with the data reported for a Froude number of 99, which is buoyancy dominated, with a higher slope of the inverse mole fraction near the point of release. The releases with Froude numbers 152 and 268 transition from momentum dominated (small slope) to buoyancy dominated (higher slope) downstream of the release, matching HyRAM+ results predicting similar concentration decay both near and far from the release point. Additional buoyancy-affected release data is needed to assess whether the transition from momentum-dominated to buoyancy-dominated releases is properly predicted, or whether the data in the Houf and Schefer [10] paper was mislabeled.

3.2.3. Ruggles and Ekoto (2012)

Experiments by Ruggles and Ekoto [26] were designed to investigate the flammability factor concept to predict ignition boundaries for releases from compressed bulk hydrogen leaks. The team designed and integrated a high-pressure stagnation chamber to produce pressure ratios up to 60:1 to investigate under-expanded hydrogen jets. Dynamic feedback was used to maintain a steady pressure ratio throughout the tests of 10:1 (stagnation to ambient pressure). The experimental conditions of the stagnation chamber were a 0.75 mm release radius, a pressure of 983.2 kPa, a temperature of 295.4 K, a density of 0.796 kg/m^3, and a 0.979 discharge coefficient.

The atmospheric conditions were 296 K and 98.37 kPa. Figure 3-8 shows the inverse centerline mass fraction and the jet half-width as a function of normalized distance.

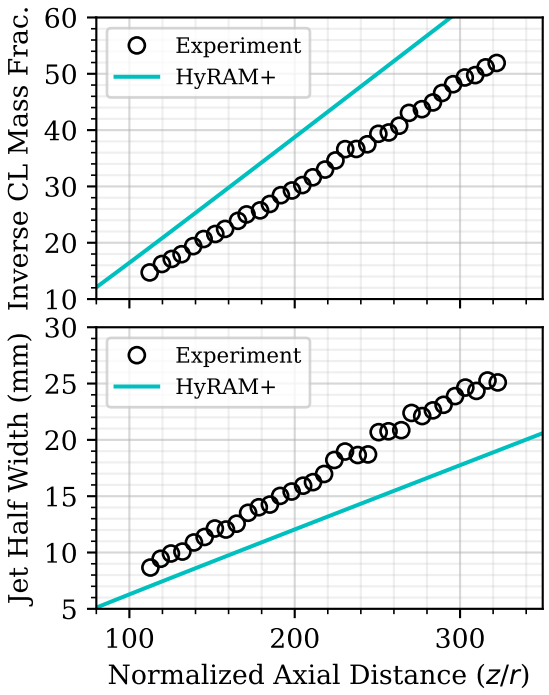
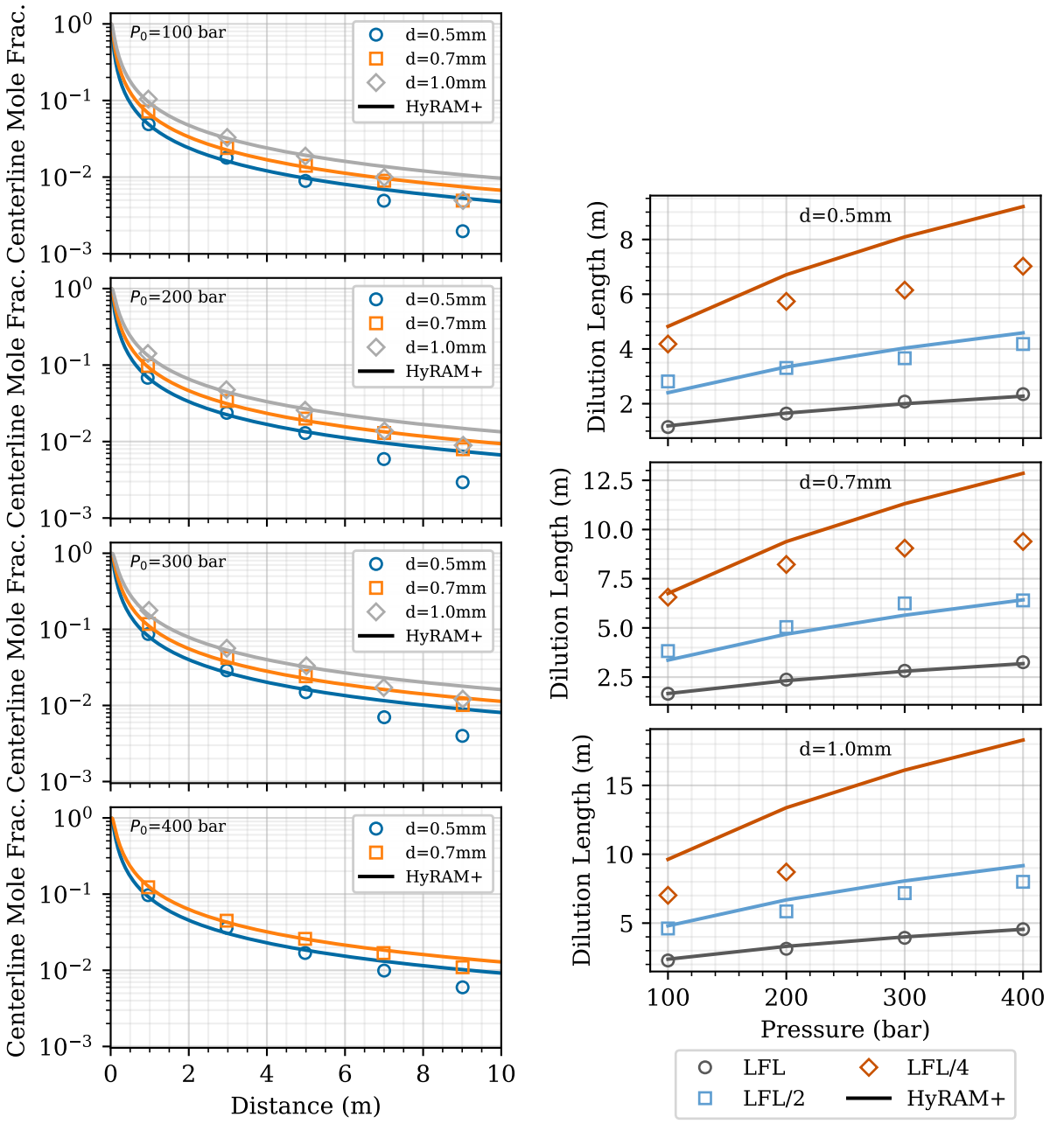


Figure 3-8 Inverse centerline mass fraction and half-width as a function of normalized downstream distance from Ruggles and Ekoto [26] (circles) compared to HyRAM+ (lines). z denotes downstream distance from the virtual origin (mm) and r is the radius of the orifice (mm).

HyRAM+ tends to overpredict the inverse centerline mass fraction and underpredict the jet half-width, which is the the distance to the point where the mass fraction is half of the centerline value. The jet half-width increases as a function of downstream distance as air is entrained in the jet. HyRAM+ predicts thinner profiles than the experimental data with lower centerline concentrations.

3.2.4. Han et al. (2013)

Han et al. [27] investigated the concentration distribution of hydrogen leaking from high pressure sources with leak diameters smaller than 1.0 mm. Hydrogen concentrations were measured at 1 m, 3 m, 5 m, 7 m, and 9 m away from the jet exit for initial tank pressures of 100 bar, 200 bar, 300 bar, and 400 bar and exit diameters of 0.5 mm, 0.7 mm, and 1.0 mm. Figure 3-9a shows the centerline mole fraction as a function of downstream distance.



(a) Centerline mole fractions

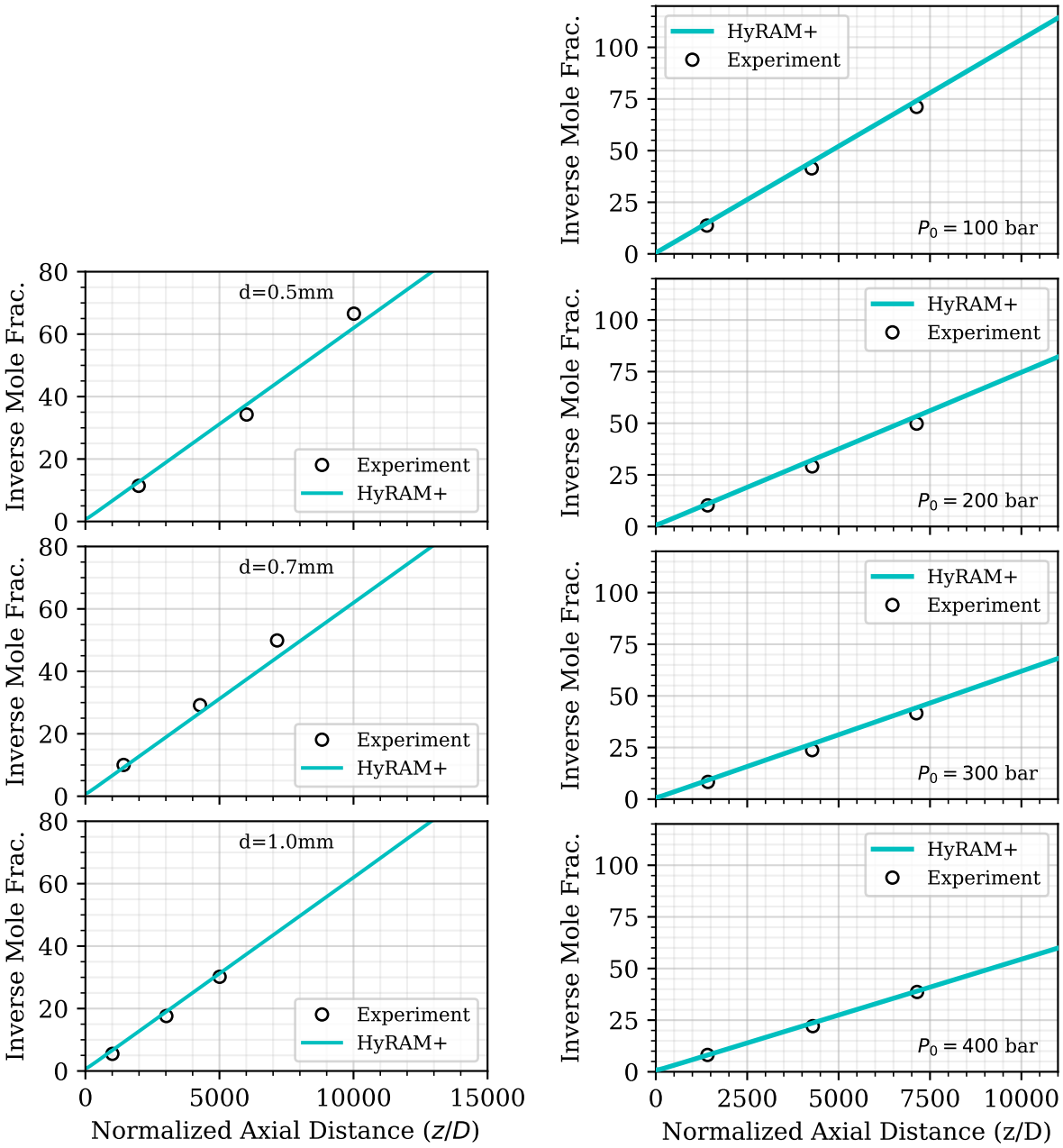
(b) Dilution length (centerline distance to fraction of LFL)

Figure 3-9 Data for 100–400 bar jets, as reported by Han et al. [27] compared to HyRAM+

Overall, HyRAM+ agrees very well with many of the data points, though overpredicts the concentrations at large axial distances. The dilution length is the distance to a certain fraction of the flammability limit, which is critical to safety, and shown in Figure 3-9b. This figure makes it easier to assess the magnitude of overprediction in mole fraction for low concentrations. HyRAM+ shows good agreement with the distances measured experimentally for all of the conditions shown for the lower flammability limit (LFL) (mole fraction of 0.04 for hydrogen in air) and half of the LFL, though overpredicts the dilution length for 1/4 of the LFL (mole fraction

of 0.01 for hydrogen in air).

Figure 3-10 provides another comparison of the centerline mole fractions measured by Han et al. [27] for the high pressure hydrogen jets.



(a) Different diameters for a pressure of 300 bar

(b) Different pressures for a 0.7 mm nozzle

Figure 3-10 Inverse centerline mole fraction as reported by Han et al. [27] compared to HyRAM+

Both groupings of the data show HyRAM+ agrees with the data very well, predicting the magnitude and linear slope of the inverse mole fraction as a function of normalized axial

distance.

3.2.5. Unignited Jet Plumes Summary

Overall, HyRAM+ predicts unignited centerline concentrations well for the data given, while also capturing buoyancy effects. The HyRAM+ model predicts narrower radial profiles than those measured experimentally. Potential model parameters that could lead to improved predictions are the relative velocity to mass-fraction spreading ratio, empirical constants within the entrainment models, or adjustment of the notional nozzle model physics.

3.3. Ignited Jet Fires

Table 3-3 lists the tables and figures that were used as validation for the HyRAM+ jet flame model with their corresponding report sections.

Table 3-3 Flame Validation Data Sources

Author(s)	Year	Figure/Table Number	Report Section
Ekoto et al. [13]	2014	Table 2	3.3.1
Schefer et al. [24]	2006	Figure 8	3.1.4
Houf and Schefer [34]	2007	Figures 5, 6	3.3.3
Imamura et al. [35]	2008	Table 2	3.3.4
Mogi et al. [36]	2005	Figure 9	3.3.5
Proust et al. [23]	2011	Figures 8, 10	3.3.6

3.3.1. Ekoto et al. (2014)

Ekoto et al. [13] performed experiments measuring the length and heat flux from two large scale jet flames. The experiments were conducted outside using compressed hydrogen at 60 barg stagnation pressure released horizontally. The two tests were conducted with orifice diameters of 20.9 mm and 52.5 mm. Full boundary conditions are provided in Table 1 in the paper. Two cameras were used to measure the visible flame lengths and a radiometer measure the heat flux at a single location for each flame. The experimental results were compared to various notional nozzle models in Table 2 of the paper based on flame length and the radiative heat flux for both straight and curved flames. Experimental results are compared to HyRAM+ predictions in Table 3-4.

Table 3-4 Flame Length and Heat Flux Results from Ekoto et al. [13] compared to HyRAM+

d_{orifice} [mm]	Length [m]		Heat Flux [kW/m^2]	
	Measured	HyRAM+	Measured	HyRAM+
20.9	17.4	19.9	4.7	6.3
52.5	45.9	47.7	23.9	27.2

As shown, HyRAM+ somewhat overpredicts the measured visible flame length and heat flux compared to the experiments.

3.3.2. Schefer et al. (2006)

The experimental setup for Schefer et al. [24] was designed to measure the flame length of a high pressure hydrogen leak ignited at the source. Two high pressure hydrogen cylinders were used with an average pressure of 2250 psia (15.5 MPaa) per full cylinder. The tests released hydrogen

vertically from the cylinders with a 3.175 mm orifice diameter, which flowed through a 7.94 mm tube sustaining the flame. A tank blowdown starting at a total pressure of 2250 psia (15.5 MPaa) was conducted to identify the mass flow rate of the release. Infrared and ultraviolet emissions were used to characterize the structure, length, and width of the flame. The radiative flux was measured using thermopile detectors both along the flame and at perpendicular radial distances. It should be noted that in this paper [24], the radial distance of the radiometers is reported as half the visible flame length, while in a subsequent paper [34], the radial distance is reported as 1.82 m. The HyRAM+ simulations assume the radial distance of the radiometers was 1.82 m, as the visible flame length is not clearly defined for a blowdown[1], and using half of the visible flame length predicts heat fluxes very different from the measurements.

Figure 3-11 shows measurements of heat flux at different distances away from the leak point (normalized to visible flame length) for different times and compares these to HyRAM+ predictions.

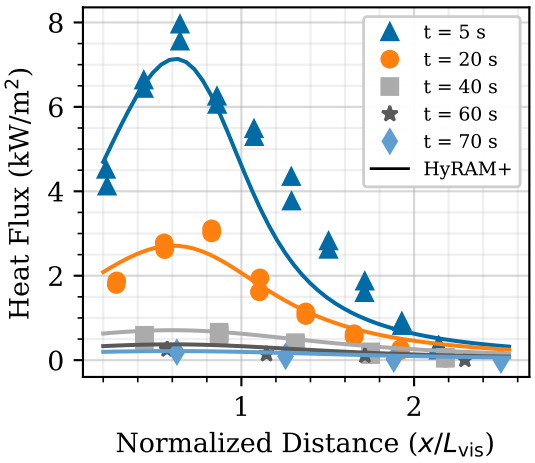


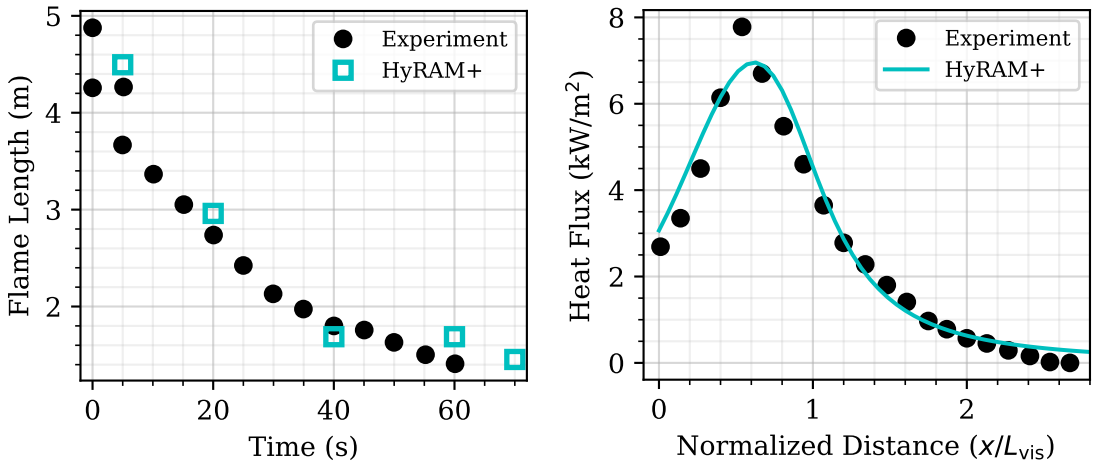
Figure 3-11 Heat flux during a blowdown as reported by Schefer et al. [24] (symbols) and predicted by HyRAM+ (lines). x is the downstream distance from the orifice and L_{vis} is the length of the visible flame.

As expected, the heat flux decreases as the pressure in the tank reduces due to discharge over time. This is captured by both the simulations and the experimental data. Both the experiments and HyRAM+ simulations predict similar shapes of the heat flux along the flame length, with a peak in heat flux around 70% of the visible flame length. HyRAM+ predicts a slightly lower peak heat flux and a faster drop-off at radiometer distances above 70% of the visible flame length compared to experimental measurements, particularly at 5 seconds after the start of the release. HyRAM+ predictions match the heat flux measurements well for 20–70 seconds after the release.

[1] We assume that the authors did not move the radiometers to a set location for each of the times in the blowdown that were reported.

3.3.3. *Houf and Schefer (2007)*

In a subsequent publication, Houf and Schefer [34] reported additional flame lengths and heat fluxes from their previous experimental campaign [24]. Figure 3-12 shows the flame length as a function of time and the radiation heat flux at different distances (normalized by visible flame length) as compared to HyRAM+ predictions.



(a) Flame length over time

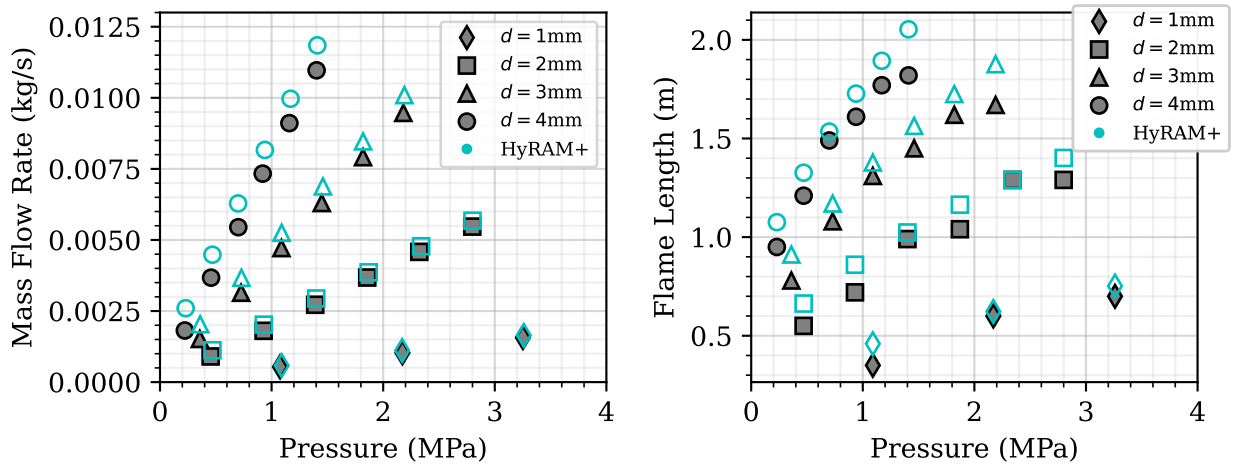
(b) Radiative heat flux vs. axial distance 5 seconds after the start of the release

Figure 3-12 Data from Houf and Schefer [34] compared to HyRAM+

As shown in Figure 3-12a, the flame lengths predicted by HyRAM+ are slightly longer than the measured flame lengths. The decay of the flame length is accurately captured, though the flames were simulated based on the mass flow rate and jet velocities reported in the paper [24], not the blowdown model in HyRAM+. Figure 3-12b is similar to Figure 3-11, although the experimentally reported heat fluxes in this paper [34] drop off faster at larger axial distances than reported previously [24] at 5 seconds. In these simulations, HyRAM+ agrees with the data very well along the length of the flame, though it predicts peak heat fluxes slightly below those measured experimentally.

3.3.4. *Imamura et al. (2008)*

Imamura et al. [35] used a regulated hydrogen spouting system to measure pressure near the nozzle, flame shapes, and temperature profiles for four nozzle diameters between 1–4 mm and spouting pressures of 0.5–3.0 MPa. Figure 3-13a shows the measured mass flow rates at different spouting pressures and nozzle diameters compared to HyRAM+ predictions.



(a) Mass flow rates

(b) Flame lengths

Figure 3-13 Data from Imamura et al. [35] compared to HyRAM+

The HyRAM+ mass flow rates, calculated using the measured pressures, are slightly higher than those reported experimentally. Using the HyRAM+ calculated mass flow rates, the flame lengths of these ignited releases were calculated. Figure 3-13b shows flame length measurements for the different spouting pressures and nozzle diameters as compared to HyRAM+ predictions. The flame lengths predicted by HyRAM+ are slightly longer than the experimental measurements, especially for the larger nozzle diameters . Some of this error is due to challenges in defining and measuring the visible flame length.

3.3.5. Mogi et al. (2005)

The shape and radiative heat flux of high pressure hydrogen jet flames were measured by Mogi et al. [36]. The experimental setup included high pressure hydrogen cylinders with a maximum pressure of 45 MPa and a total capacity of 0.184 m^3. Flame lengths and widths were measured at various spouting pressures ranging between 0.01 MPa and 40 MPa for orifice diameters between 0.4 mm and 4 mm. Flame lengths were also measured at various orifice diameters between 1–5 mm at different spouting pressures of 10 MPa, 20 MPa, and 35 MPa. Figure 3-14 shows heat flux measurements for various orifice diameters and distances away from the flame against different mass flow rates.

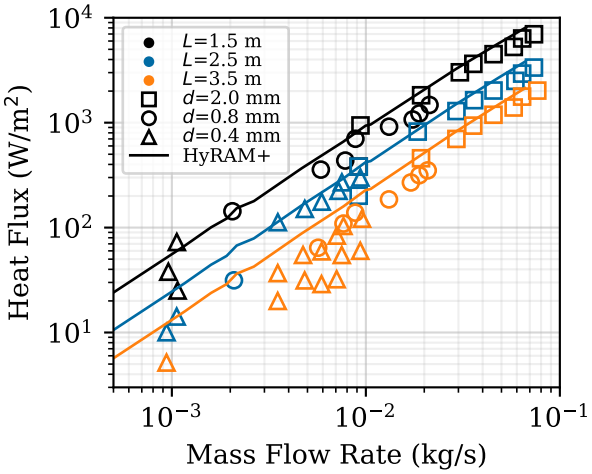
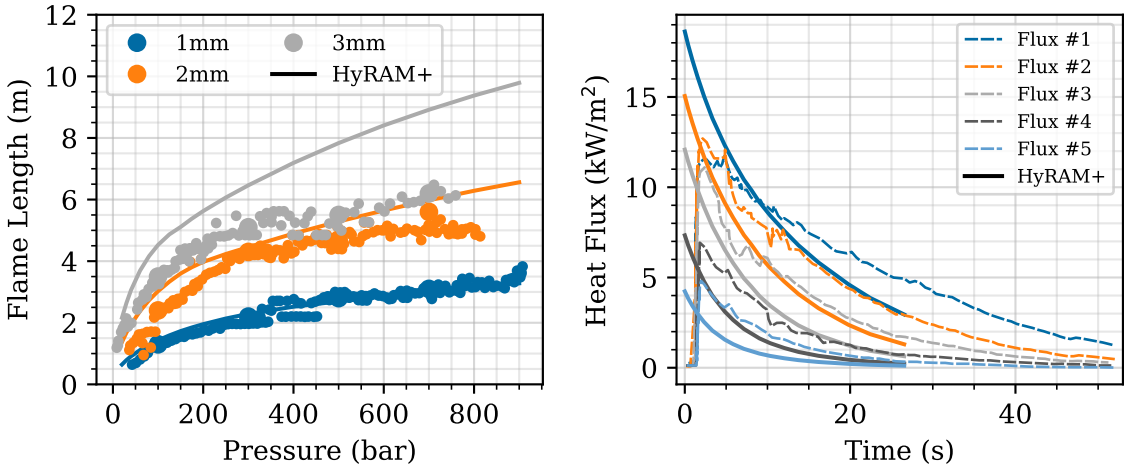


Figure 3-14 Radiative heat flux values for different mass flowrates from Mogi et al. [36] compared to HyRAM+, in which d is the diameter of the orifice and L is the distance between the detector and flame axis

Intuitively, as the distance from the flame axis (L) becomes larger, the heat flux decreases, and the smallest diameter nozzles lead to the lowest mass flow rates and heat fluxes. HyRAM+ predicts heat fluxes that capture the experimental trends well, though some of the individual heat fluxes are overpredicted, particularly at low mass flow rates. Since the risk of harm increases with increased heat flux, HyRAM+ tends to give conservative predictions with its heat flux calculations.

3.3.6. Proust et al. (2011)

Proust et al. [23] measured hydrogen flame characteristics of high pressure horizontal releases. The experiments measured pressure, temperature, and mass flow over the release duration. The hydrogen tank reservoir had a 25 L volume with a varying release diameter between 1–3 mm. To measure the pressure during the release, a piezoresistive sensor was placed on the head of the bottle. To capture the flame temperature, ten thermocouples were placed along the line of the flame. The heat flux was measured by placing five fluxmeters at a 45°-angle horizontal to the flame. Figure 3-15a shows the flame length vs. pressure for the different release orifice diameters.



(a) Flame length vs. pressure

(b) Heat flux over time for a 2 mm orifice

Figure 3-15 Data from Proust et al. [23] during a 900 bar blowdown compared to HyRAM+

As expected, the flame lengths are smaller for smaller pressures and for smaller diameter orifices. The HyRAM+ predictions agree with the data for the 1 mm and 2 mm orifices, but substantially overpredict flame lengths for the 3 mm orifice, especially at higher pressures. The authors explain that the flame lengths were extracted from video records, but do not completely describe the setup or criteria [23]. It is possible that the larger flames, with more luminous output, changed the f-number of the camera system, hence changing the criteria for the definition of length. It is also possible that the width—which in HyRAM+ is set to be 0.17 times the length—increases for larger flames. There are significantly more combustion products for the 3 mm orifice than the 2 mm orifice at the highest pressure, but a modest experimental increase in flame length. While the HyRAM+ models could be improved to give more accurate results, the overprediction of flame length mean that HyRAM+ provides a conservative estimate of flame length, which is of less concern than an underprediction. In other words, hazard or risk assessments using HyRAM+ with larger orifice diameters and higher pressures would result in a more conservative (longer) flame length than in reality.

The time history of the heat flux for the 2 mm blowdown is shown in Figure 3-15b. As expected, at the start of the blowdown when the pressure is the highest, the heat flux is the highest. Experimentally, it takes some time for the radiometers to register the heat flux, but after they begin to register the heat flux, they show a similar decay and magnitude as the HyRAM+ predictions. HyRAM+ does overpredict heat flux at the beginning of the blowdown and underpredicts toward the end of the blowdown. This can be at least partially attributed to the thermal capacitance and response lag of the radiometers, as they take time to register and decay.

3.3.7. Ignited Jet Fires Summary

Overall, HyRAM+ provides accurate predictions of flame length for hydrogen flames up to 900 bar. There is some minor overprediction in the heat flux predictions, which provides some

conservatism to the HyRAM+ calculations.

3.4. Accumulation and Overpressure in Enclosures

Table 3-5 lists the tables and figures that were used as validation for the indoor accumulation and overpressure model in HyRAM+ and the corresponding report sections.

Table 3-5 Overpressure/Accumulation Validation Data Sources

Author(s)	Year	Figure Number	Report Sections
Ekoto et al. [21]	2012	Figures 9, 14	3.4.1
Giannissi et al. [37]	2015	Figure 7	3.4.2
Merilo et al. [38]	2011	Figures 2, 6a	3.4.3
Bernard-Michel and Houssin-Agbomson [39]	2017	Figures 7, 9	3.4.4

3.4.1. Ekoto et al. (2012)

Ekoto et al. [21] performed experiments to study the overpressure in warehouse facilities. The experimental facility was 3.64 m wide, 4.59 m long, and 2.72 m tall with a total volume of 45.4 m^3. Hydrogen was released from a tank with a volume of 3.63 L, a pressure of 13.45 MPa, and a temperature of 297 K. This resulted in a hydrogen mass of 0.00363 kg, which was released through an opening with a diameter of 3.56 mm and a discharge coefficient of 0.75. To mimic a hydrogen release from a forklift, an apparatus was designed to replicate different release conditions. The release enclosure was 34.3 cm long, 34.3 cm wide, and 43.5 cm high, and elevated 6.4 cm off the facility floor. The release area within the enclosure was a 13.1 cm by 13.1 cm square. The release consisted of a blowdown of commercial six-pack of hydrogen tanks. The release enclosure was set towards the center and along the wall of the facility, while thermocouples and pressure sensors were placed across the facility. Various tests were performed with and without a ventilation area, no ventilation, natural ventilation, and forced ventilation. Ignition locations and ignition times varied as well for the thirteen tests measuring hydrogen concentration over time at various locations within the facility and over-pressure values within the facility over time. Figure 3-16 shows the hydrogen mole fraction over time for three different sensors along the ceiling for tests with and without mechanical ventilation, with data reported by Ekoto et al. [21] compared to the HyRAM+ layer mole fraction predictions.

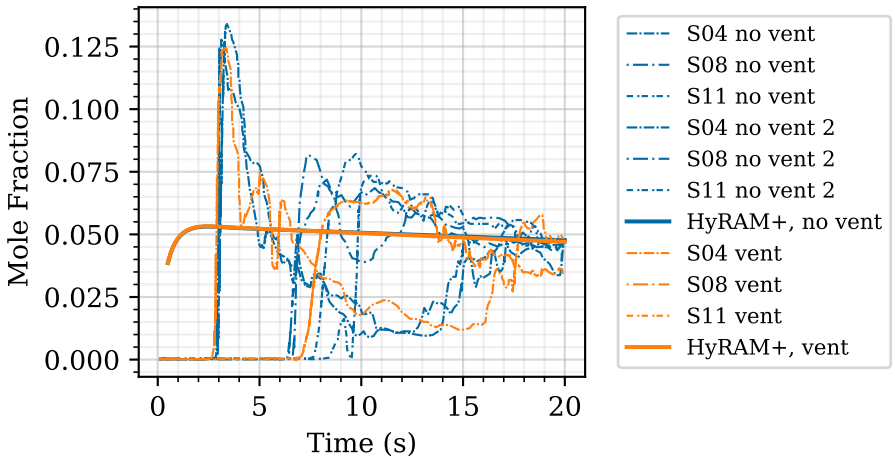


Figure 3-16 Hydrogen mole fraction measurements from different sensors at the ceiling over multiple experiments with and without ventilation from Ekoto et al. [21] compared to HyRAM+ predictions

The mole fraction predictions in HyRAM+, shown by the solid orange and blue lines, are very similar with and without ventilation. The insignificance of ventilation is also shown in the experimental data–Figure 3-16 shows the concentration measurements have only minor differences for each sensor with or without ventilation. The experimental data shows no initial concentration reading for 3–7 seconds, then register a peak and subsequent decrease with significant fluctuations. These fluctuations are likely due to turbulence mixing at the ceiling. The near steady-state (slightly decreasing) mole fraction predicted by HyRAM+ is near the average of the sensor data.

The overpressures when Ekoto et al. [21] ignited the mixtures in the warehouse is shown in Figure 3-17.

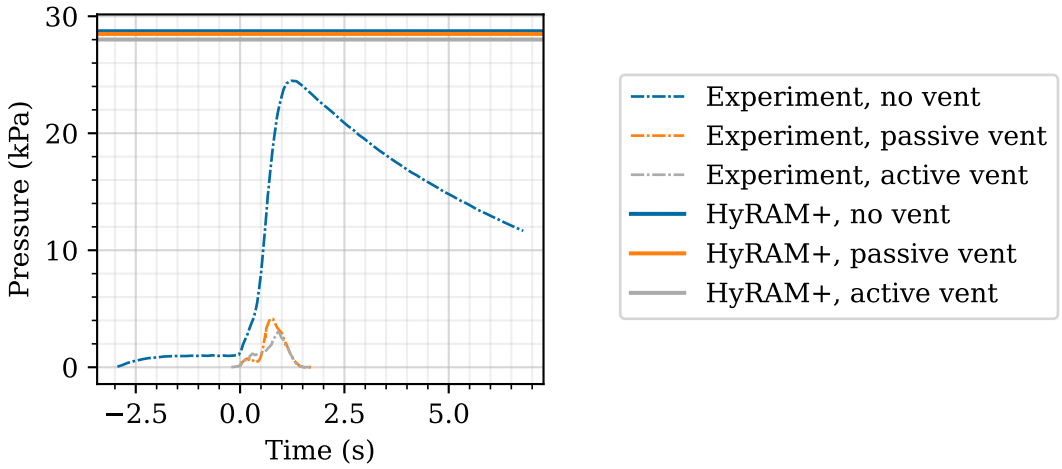


Figure 3-17 Overpressure values from Ekoto et al. [21] (thin, dashed lines) for igniting hydrogen mixtures 3 seconds after the start of the release (ignition at time 0) compared to the predictions from HyRAM+ (thick, solid lines).

The authors ignited each of these releases after 3 seconds, observing the effect of ventilation. The highest overpressure was measured without ventilation, registering on the pressure transducer about 1 second after ignition. Peak overpressure for the passive and active ventilation cases were significantly lower with a slightly shorter delay compared to the case without ventilation. HyRAM+ predicts pressures slightly above the peak overpressure observed experimentally with no ventilation, and well above the peak ovepressures with ventilation. HyRAM+ predicts the highest overpressure without ventilation, and slightly lower overpressures with passive and then active ventilation, providing a estimate for all experimental measurements.

3.4.2. Giannissi et al. (2015)

Giannissi et al. [37] described some of the HyIndoor tests with measurements of the diffusion of hydrogen in a ventilated enclosure under various conditions. The test facility was a rectangular box with a total volume of 31.25 m^3. Various release rates, wind conditions, and vent locations were tested. Twenty-seven oxygen sensors were placed within the facility to measure the hydrogen concentration for each of the different tests. They were placed on vertical planes to gather information on both horizontal and vertical flow. The hydrogen was released vertically from the center of the facility to measure the hydrogen concentration over time. Figure 3-18 shows the hydrogen concentration over time measured by three sensors along the ceiling, as compared to the HyRAM+ predictions.

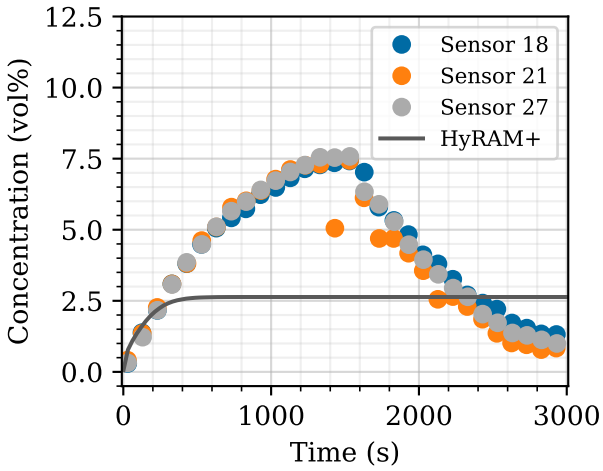


Figure 3-18 Hydrogen concentration measurements along the ceiling from Giannissi et al. [37] compared with HyRAM+ predictions

The experiments show an increase in concentration to 7.5% at about 1500 seconds for all three sensors before starting to reduce. Conversely, HyRAM+ predicts an increase in concentration to about 2.5% (below the flammability limit of hydrogen of 4%), where it remains constant 200 seconds following release. The difference in the predicted vs. measured concentrations is concerning since it is in a non-conservative direction (i.e., HyRAM+ predicts a lower concentration compared to experimental data). This could be because the hydrogen was released

vertically, which would mix inconsistently with the air as it spread along the ceiling where the sensors are located. The simplified model in HyRAM+, however, assumes a perfectly-mixed hydrogen-air mixture along the ceiling. Local levels of higher concentration within this layer (such as from plume impingement) are therefore not captured in the simple layer model in HyRAM+.

3.4.3. Merilo et al. (2011)

Merilo et al. [38] measured hydrogen releases in a model of a typical residential car garage. The experimental facility was 60.4 m^3 in volume and included both mechanical and natural ventilation openings for different tests. Figure 3-19 shows hydrogen concentration measurements at different heights within the enclosure for different release flow rates and vehicle location tests. The bottom-right frame of Figure 3-19 is for a condition with mechanical ventilation, while the other frames are conditions without mechanical ventilation.

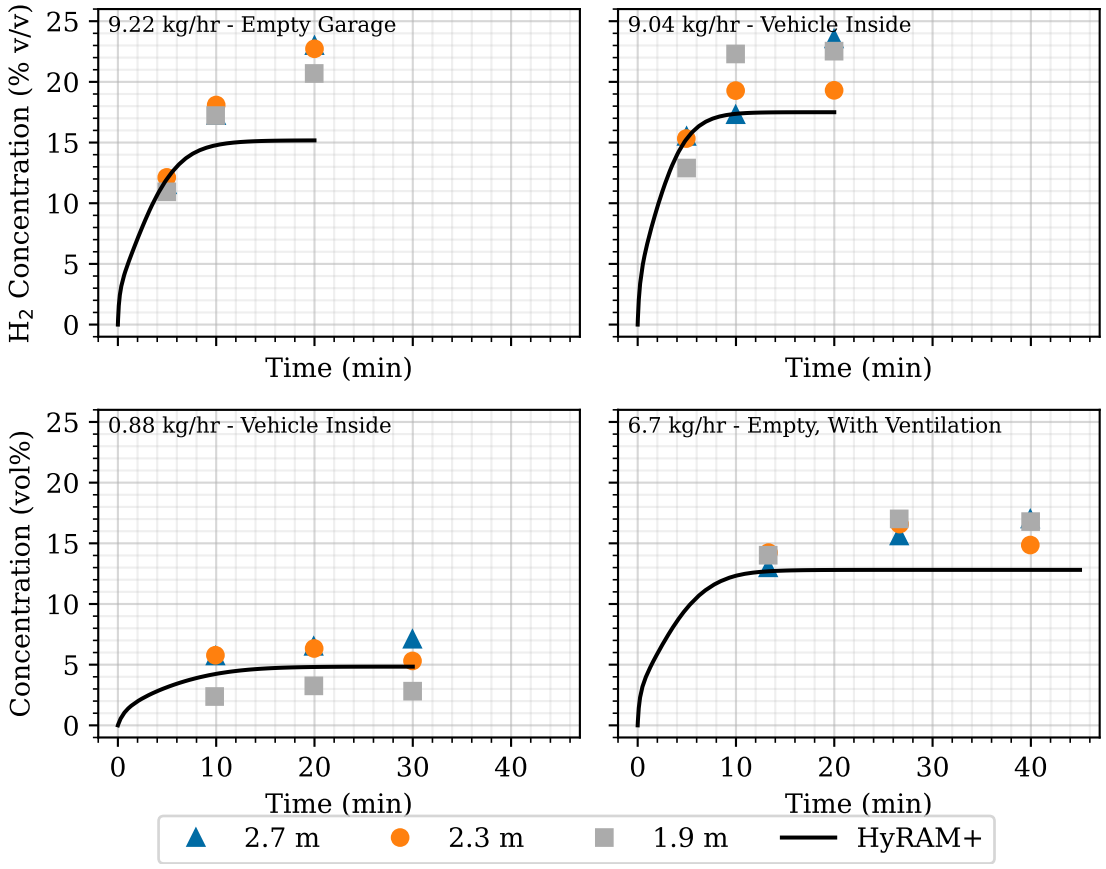


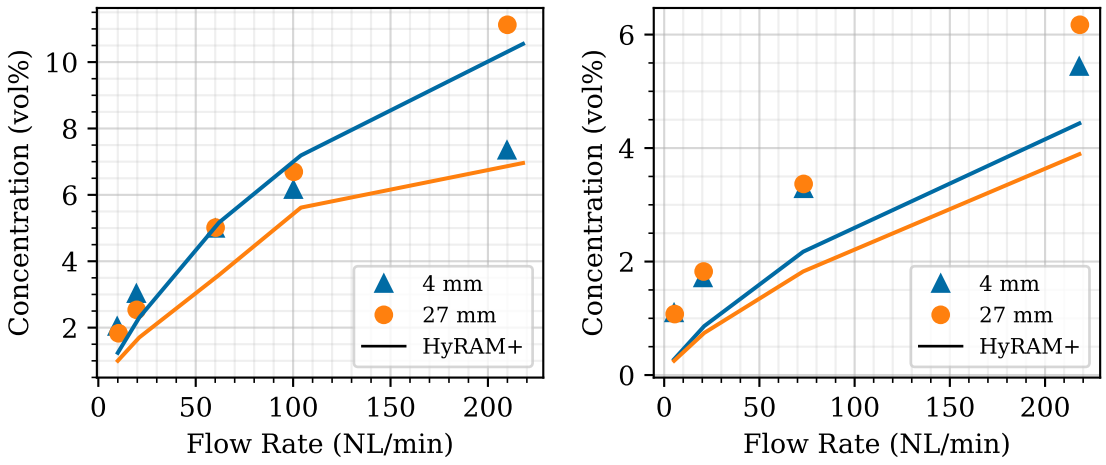
Figure 3-19 Hydrogen concentrations at different heights over time for tests with different hydrogen flow rates and garage open space from Merilo et al. [38] compared to HyRAM+ predictions. The lower right frame has 0.1 m^3/s mechanical ventilation, which all other frames have only natural ventilation.

The rise in concentration predicted by HyRAM+ is similar to that measured experimentally, although HyRAM+ slightly underpredicts the steady-state concentration in almost all cases. There is no clear correlation in the concentration measured by the sensors at different heights, suggesting

that the well-mixed layer model may be acceptable for hydrogen being released into such an enclosure.

3.4.4. Bernard-Michel and Houssin-Agbomson (2017)

Bernard-Michel and Houssin-Agbomson [39] compared releases of helium and hydrogen in enclosures with two ventilation openings. Two enclosures with 1 and 2 m^3 volume were tested with a vent at the bottom for inflow and vent at the top for outflow as depicted in Figure 1 of [39]. Hydrogen or helium was released from the bottom of the enclosure vertically, and the injection height varied between 20 cm and 220 cm within the enclosure. Release diameters of 4 mm or 27.2 mm and flow rates between 5–240 nL/min were tested. The concentration of either hydrogen or helium was measured vertically along the enclosure. Figure 3-20 shows the maximum volume concentration of hydrogen for different release flow rates and different orifice sizes at the top of the 1 m^3 enclosure (Figure 3-20a) and the 2 m^3 enclosure (Figure 3-20b). Approximately 10 minutes of steady state data was recorded, though the specific time of concentration measurements is not provided.



(a) 1 m^3 enclosure **(b)** 2 m^3 enclosure

Figure 3-20 Data from Bernard-Michel and Houssin-Agbomson [39] compared to HyRAM+, showing maximum hydrogen concentration values for different release flow rates and orifice sizes in two enclosures

HyRAM+ has reasonable agreement with the experimental concentrations for the 1 m^3 enclosure, but underpredicts concentrations for the 2 m^3 enclosure. The HyRAM+ model predict higher concentrations for the 4 mm orifice, while the experiments showed higher concentrations for the larger orifice. There is mixing and venting in both the experiments and model, with HyRAM+ assuming a uniform layer concentration within the top of the enclosure. The physics of this mixing and layering is complex and can be more accurately captured using higher fidelity computational fluid dynamics models. Nonetheless, HyRAM+ is fairly accurate using the simplifications that enable less computationally expensive modeling of these scenarios.

3.4.5. Accumulation and Overpressure in Enclosures Summary

Overall, HyRAM+ predicts similar accumulation of hydrogen within enclosures to many of the experiments described in this section, although it underpredicts the accumulation for some. HyRAM+ also conservatively predicts the overpressure that would result from the ignition of an accumulated mixture within an enclosure both with and without ventilation, though there was only a single literature source for this comparison.

3.5. Cryogenic Releases

There are only a handful of groups globally that have reported on experiments with cryogenic hydrogen. In this section, we compare HyRAM+ to the cryogenic hydrogen dispersion, blowdown, and flame data that are currently available. This includes data from the Karlsruhe Institute of Technology and their partners [40–42] and data from researchers at Sandia National Laboratories [43, 44].

3.5.1. Blowdowns

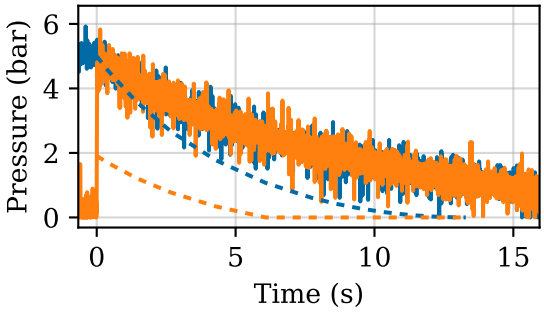
Table 3-6 lists the dataset that was used as validation for the blowdown model for cryogenic releases in HyRAM+ and the corresponding report section.

Table 3-6 Cryogenic Blowdown Validation Data Sources

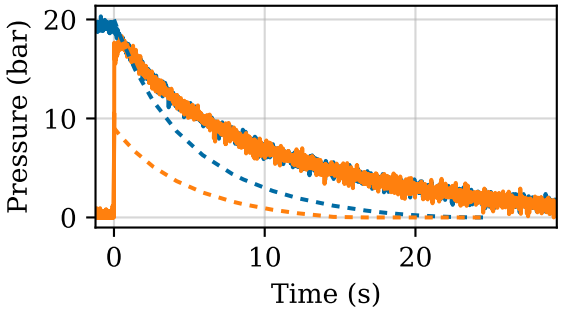
Author(s)	Year	Figure/Table Number	Report Section
Friedrich et al. [42]	2019	Directly from dataset	3.5.1.1

3.5.1.1. Friedrich et al. (2019)

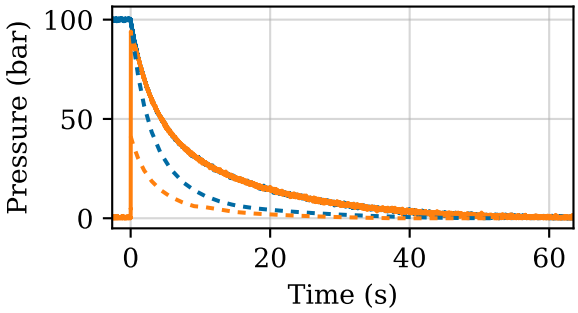
The Pre-normative Research for Safe use of Liquid Hydrogen (PreSLHy) project funded by the European Fuel Cells and Hydrogen Joint Undertaking (FCH JU) studied several aspects of liquid hydrogen behavior. In one series of experiments in Friedrich et al. [42], hydrogen at high pressures (5–200 bar) and ambient to low temperatures (80 K) was discharged through orifices of various sizes. Results from several of these experiments are shown in Figures 3-21–3-23.



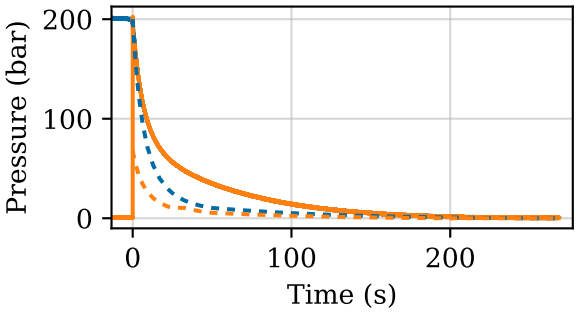
(a) P = 5 bar, T = 80 K, d = 1 mm



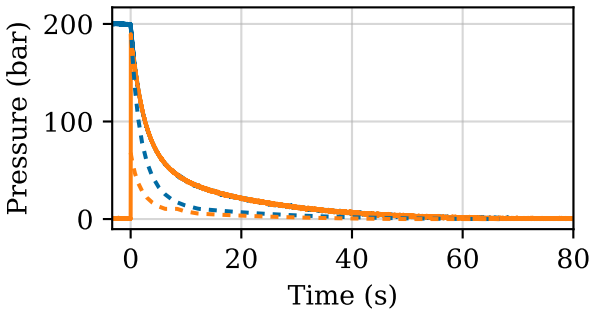
(b) P = 20 bar, T = 80 K, d = 1 mm



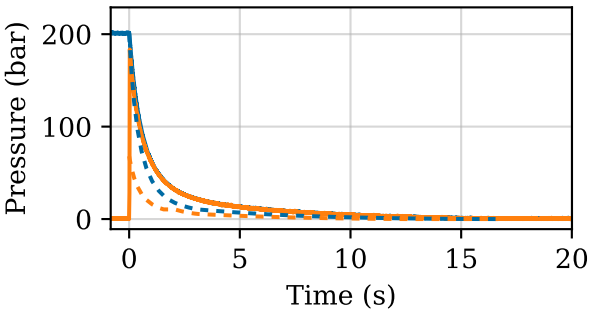
(c) P = 100 bar, T = 80 K, d = 1 mm



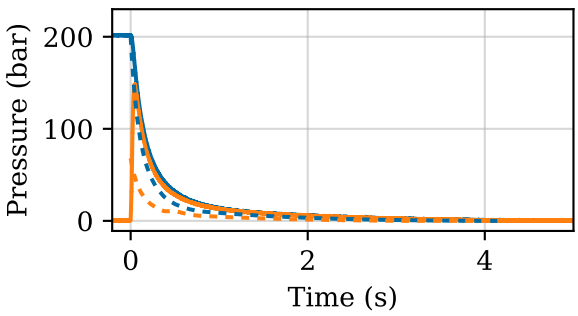
(d) P = 200 bar, T = 80 K, d = 0.5 mm



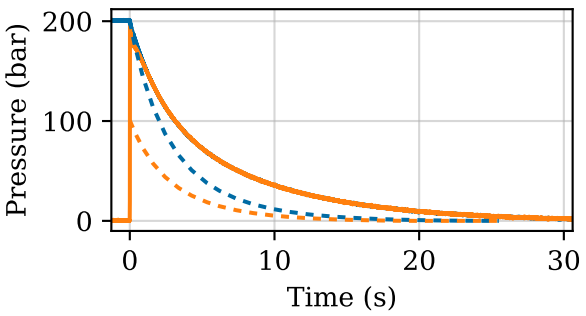
(e) P = 200 bar, T = 80 K, d = 1 mm



(f) P = 200 bar, T = 80 K, d = 2 mm



(g) P = 200 bar, T = 80 K, d = 4 mm

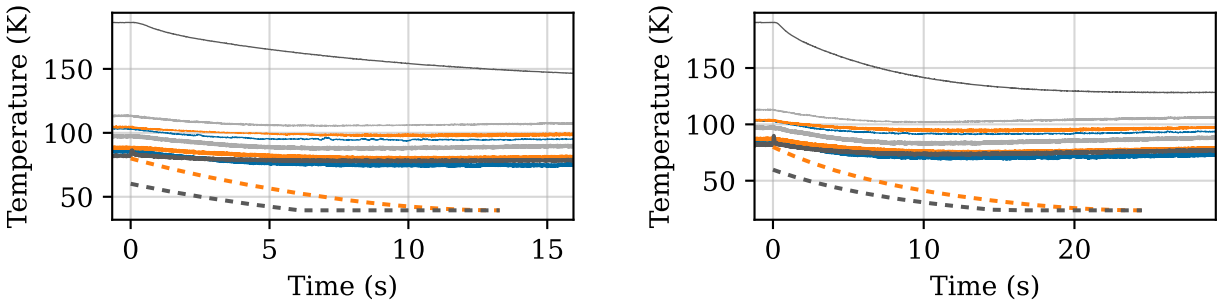


(h) P = 200 bar, T = 300 K, d = 1 mm

Figure 3-21 Pressure during discharge for vessel (blue) and nozzle (orange) for various pressures, temperatures, and nozzle diameters from Friedrich et al. [42] (solid lines) compared to HyRAM+ (dashed lines)

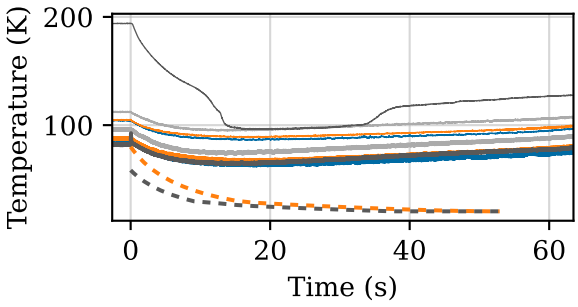
Figure 3-21 shows the pressure decay within the vessel and at the nozzle during the discharge experiments. Note that the solid data lines sometimes overlap, making them difficult to distinguish. HyRAM+ (dashed lines) tends to predict a faster pressure decay compared to the experiments, although the HyRAM+ prediction for vessel pressure decay better matches for the largest nozzle diameter (Figure 3-21g). Experimentally, there was very little pressure difference observed between the nozzle and vessel pressure, while there is a fairly large pressure difference predicted by HyRAM+. The PreSLHy authors [42] do not describe the pressure measurement in detail, and so it is possible that they were measuring the total pressure (which would include a large dynamic pressure due to the high-speed flow) while HyRAM+ ignores dynamic pressure. There are also likely errors in the modeling as HyRAM+ assumes isentropic expansion of the fluid through the nozzle while there will be heat losses in realistic conditions. HyRAM+ also assumes a perfectly insulated (adiabatic) tank, but heat flow into the tank also affects the blowdown pressure. In all cases, the time to empty (time to reach ambient pressure) is slightly faster for the HyRAM+ predictions compared to the experimental data.

Figure 3-22 shows the temperature within the vessel during the discharge. The measurements include three sets of two thermocouples located at the top (blue), center (orange), and bottom (green) of the vessel. In each of the subplots, the temperature measurements for one set of three thermocouples is 10–20 K lower than the other set of thermocouples. The lower temperature measurements are sheathed thermocouples, while the higher temperatures are unsheathed. The open (unsheathed) thermocouple measurements are marked by a thinner line on the plots, which can be seen by close inspection of Figure 3-22. There are also two measurements of the nozzle temperature. The lower (and thicker) red line is a measurement of a sheathed thermocouple that is mounted in a hole in the nozzle aperture with no direct contact with the flow, while the higher temperature (thin line) is from a thermocouple welded into the nozzle line. There are two dashed lines, showing the predicted temperatures by HyRAM+ – the orange dashed line is the temperature in the vessel (there is only one predicted temperature in the vessel by HyRAM+), and the red dashed line is the temperature of the fluid in the nozzle. The sheathed thermocouples agree much better than the open thermocouples with the reported release temperatures at time zero (80 K, or 300 K in Figure 3-22h), and the predicted HyRAM+ temperatures at time zero in all cases. There is some offset for the unsheathed thermocouples. Also in all cases, the temperature drop within the vessel as the fluid is released is predicted to be much greater than the experimentally measured temperature decrease. This could be due to inaccuracies in the measurements due to the heat capacity of the thermocouples or conduction from the vessel wall along the length of the thermocouples, although they were a small diameter (0.36 mm). Some differences are likely from the adiabatic vessel assumption in HyRAM+, which neglects heat loss. HyRAM+ also assumes that the gases in the vessel are instantly and completely well-mixed, while differences in the measured temperatures indicates the gases are not fully mixed. Similar to the pressure calculations in the nozzle, the temperature predictions in the nozzle are also significantly lower than the tank temperature and other measurements that track the tank temperature closely (e.g., the sheathed thermocouple).

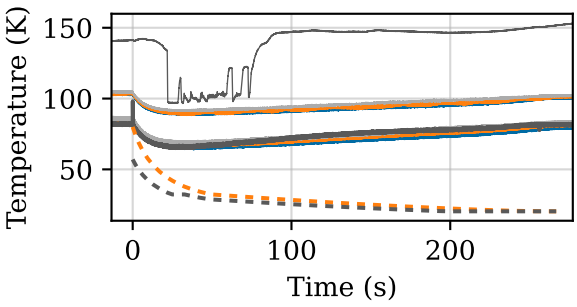


(a) P = 5 bar, T = 80 K, d = 1 mm

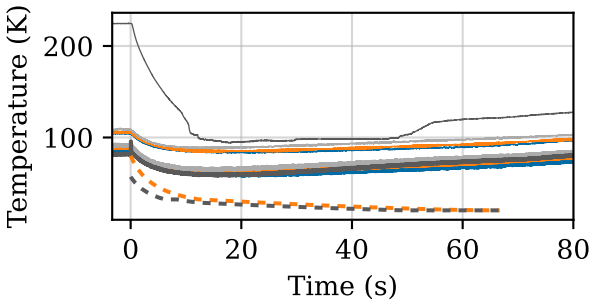
(b) P = 20 bar, T = 80 K, d = 1 mm



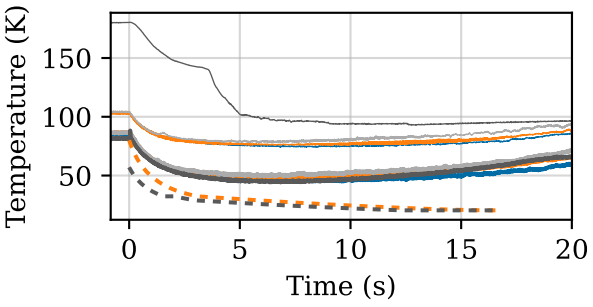
(c) P = 100 bar, T = 80 K, d = 1 mm



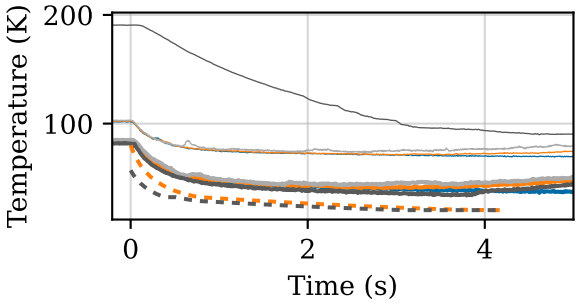
(d) P = 200 bar, T = 80 K, d = 0.5 mm



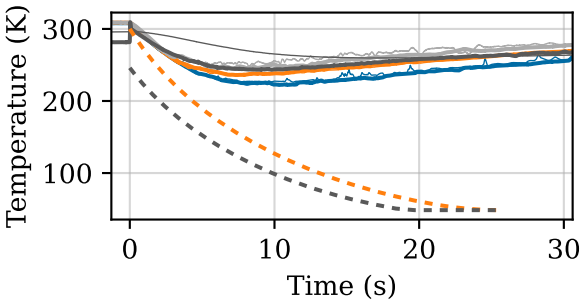
(e) P = 200 bar, T = 80 K, d = 1 mm



(f) P = 200 bar, T = 80 K, d = 2 mm

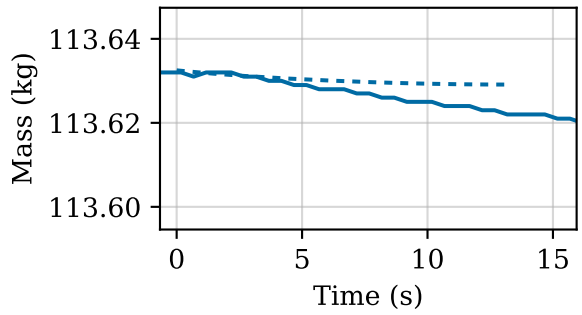


(g) P = 200 bar, T = 80 K, d = 4 mm

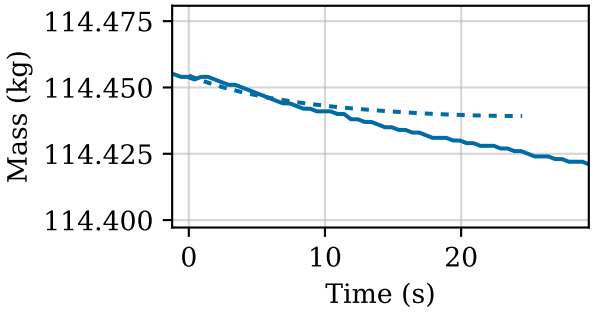


(h) P = 200 bar, T = 300 K, d = 1 mm

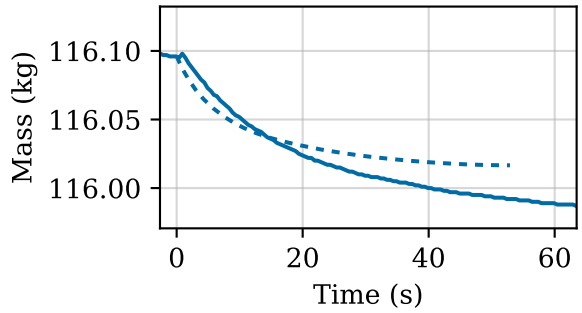
Figure 3-22 Temperature during discharge for vessel top (blue), vessel center (orange), vessel bottom (green), and nozzle (red) as measured by sheathed (thick line) and unsheathed (thin line) thermocouples for varied pressures, temperatures, and nozzle diameters from Friedrich et al. [42] (solid lines) compared to HyRAM+ (dashed lines)



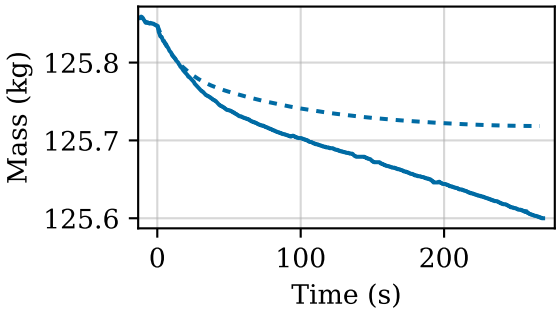
(a) P = 5 bar, T = 80 K, d = 1 mm



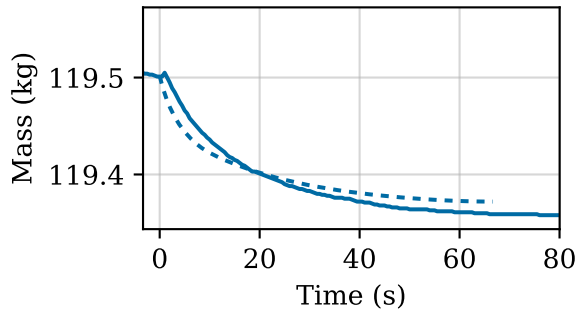
(b) P = 20 bar, T = 80 K, d = 1 mm



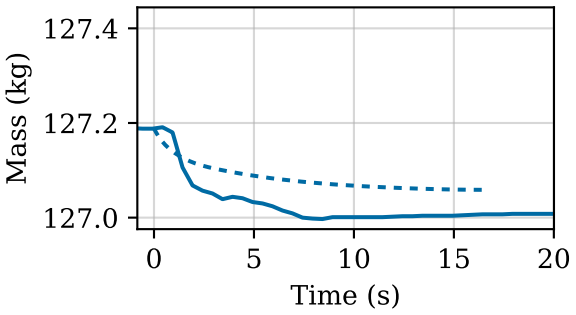
(c) P = 100 bar, T = 80 K, d = 1 mm



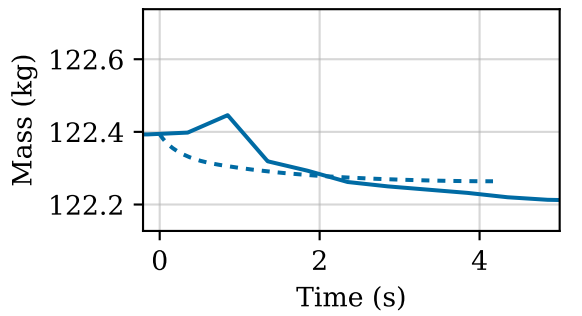
(d) P = 200 bar, T = 80 K, d = 0.5 mm



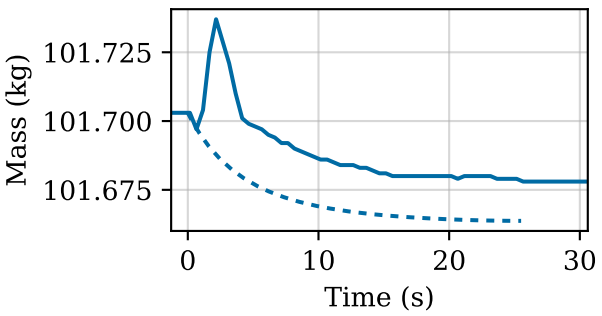
(e) P = 200 bar, T = 80 K, d = 1 mm



(f) P = 200 bar, T = 80 K, d = 2 mm



(g) P = 200 bar, T = 80 K, d = 4 mm



(h) P = 200 bar, T = 300 K, d = 1 mm

Figure 3-23 Tank mass during discharge from Friedrich et al. [42] (solid lines) compared to HyRAM+ (dashed lines)

Figure 3-23 shows the combined mass of both the vessel itself and the hydrogen within the vessel. The HyRAM+ predictions have the weight of the vessel at time zero added to the mass loss predictions, so that the predictions initially agree with the measurements. The highest mass of hydrogen expelled is a little over 0.1 kg (for 200 bar and 80 K), while the overall weight of the vessel is approximately 120 kg. It is remarkable that the scale is able to capture the small weight loss and not surprising that there are some instances of drift or inaccuracies in the mass measurements. Nonetheless, the HyRAM+ simulations agree relatively well with the measurements for all diameters, initial pressures, and initial temperatures.

3.5.1.2. Cryogenic Blowdowns Summary

In summary, HyRAM+ predicts slightly faster blowdowns of 80 K hydrogen than measured in the PreSLHy project [42]. HyRAM+ accurately predicts the mass loss from the vessel, but lower temperatures within the nozzle and vessel than were measured experimentally.

3.5.2. Unignited Jet Plumes

Table 3-7 lists the figures and datasets that were used as validation for the unignited jet plume model for cryogenic releases in HyRAM+.

Table 3-7 Cryogenic Unignited Jet Plumes Validation Data Sources

Author(s)	Year	Figure/Table Number	Report Section
Xiao et al. [40]	2011	Figure 3	3.5.2.1
Friedrich et al. [41]	2012	Figure 5	3.5.2.2
Hecht and Panda [44]	2019	Figure 10, and new data	3.5.2.3
Friedrich et al. [42]	2019	Directly from dataset	3.5.2.4

3.5.2.1. Xiao et al. (2011)

Xiao et al. [40] describe horizontal discharges of room temperature and cryogenic (80 K) hydrogen at pressures from 8.25–68.5 bar. Concentration measurements were taken at several locations downstream of the release point. Table 3-7 lists the tables and figures used as validation for the unignited jet plume model. Figure 3-24 shows the data, along with the calculated inverse mole fraction from HyRAM+.

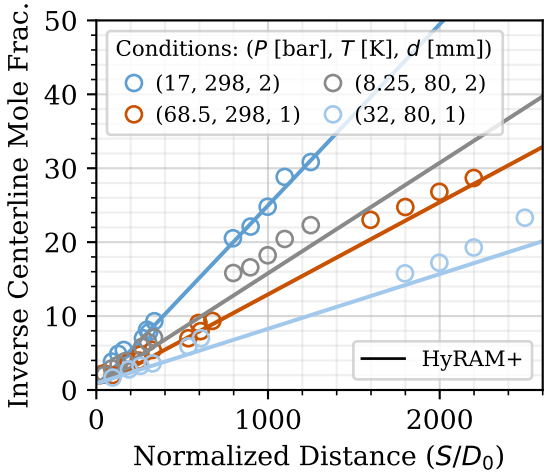
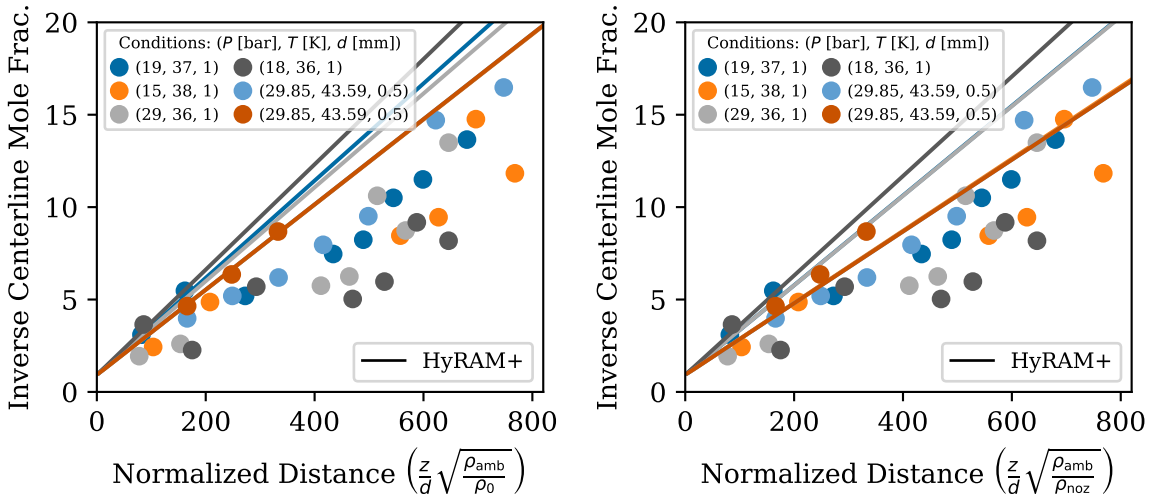


Figure 3-24 Data from Xiao et al. [40] (open circles) compared to HyRAM+ (solid lines) showing inverse centerline mole fraction as a function of normalized downstream distance for four release scenarios, including two cryogenic (80 K) releases. S denotes downstream distance and D_0 denotes the orifice diameter.

For the range of conditions described by Xiao et al. [40], HyRAM+ results in reasonably accurate predictions of mole fraction as the LFL (inverse mole fraction of 25) is approached and exceeded.

3.5.2.2. Friedrich et al. (2012)

] Friedrich et al. [41] describe horizontal discharges of cryogenic (34–65 K) hydrogen at pressures up to 35 bar. Experiments where the hydrogen was ignited are the focus of the paper, but the authors also present some centerline concentration measurements. The normalized jet centerline inverse mole fraction as a function of normalized downstream distance is presented in Figure 3-25.



(a) Normalized by stagnation density

(b) Normalized by nozzle density

Figure 3-25 Data from Friedrich et al. [41] (circles) compared to HyRAM+ (lines) showing centerline mole fraction as a function of normalized downstream distance. z denotes downstream distance, d denotes the orifice diameter, ρ_{amb} denotes ambient fluid density, ρ_0 denotes stagnation density, and ρ_{noz} is the nozzle density.

Figure 3-25a shows that HyRAM+ underpredicts the mole fractions at large distances (i.e., overpredicts the inverse mole fraction), which will result in shorter distances to the LFL than measured experimentally. The authors note in the paper that the concentration decay appears to be slower than for room temperature releases. Since HyRAM+ results agree with room temperature concentration decays (see Section 3.2), this underprediction is not surprising if the authors' observation is true. However, it is possible that the authors incorrectly reported the density used in the normalization of the distance scale. HyRAM+ results normalized by nozzle density are shown in Figure 3-25b, which align more closely with the experimental data than the stagnation density.

3.5.2.3. Hecht and Panda (2019)

Hecht and Panda [44] performed lab-scale releases using 1 mm and 1.25 mm nozzles under conditions of 2–5 bar and 45–82 K cryogenic hydrogen. The average mole fraction and temperature fields of these releases were measured using planar laser Raman imaging. The

concentration fields are shown in Figure 3-26 and the temperature fields are shown in Figure 3-27. Note that in addition to the data reported directly by Hecht and Panda [44], these figures also include additional data from the same experimental series from Ehrhart et al. [15].

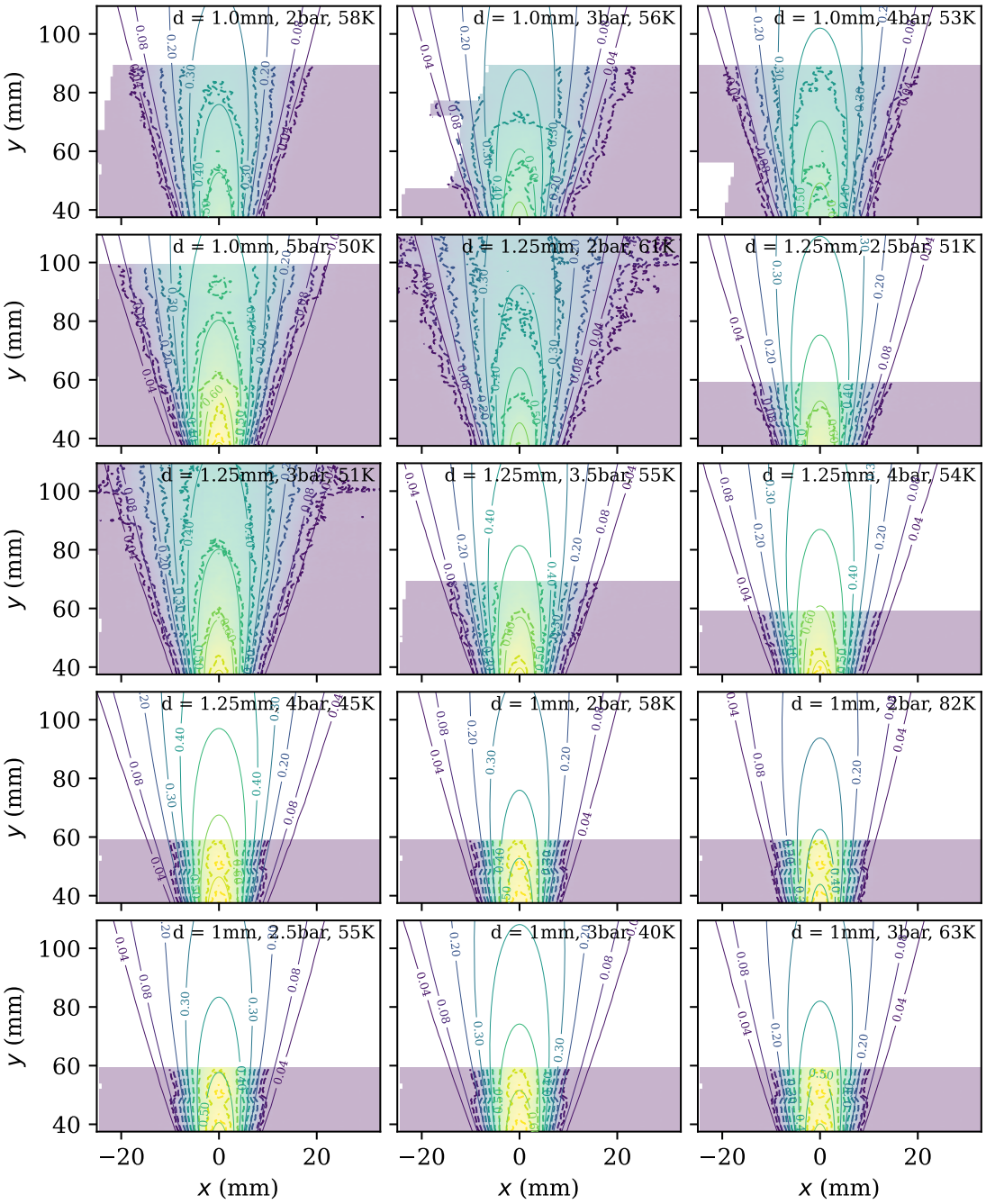


Figure 3-26 Comparison of mole fraction calculated by HyRAM+ (thin, solid lines) to cryogenic hydrogen dispersion data reported by Hecht and Panda [44] and Ehrhart et al. [15] (thick, dashed lines and background shading). In many cases, data was limited to the near-nozzle region, and areas with a white background indicate that there is no experimental data. Mole fractions are indicated on the contours.

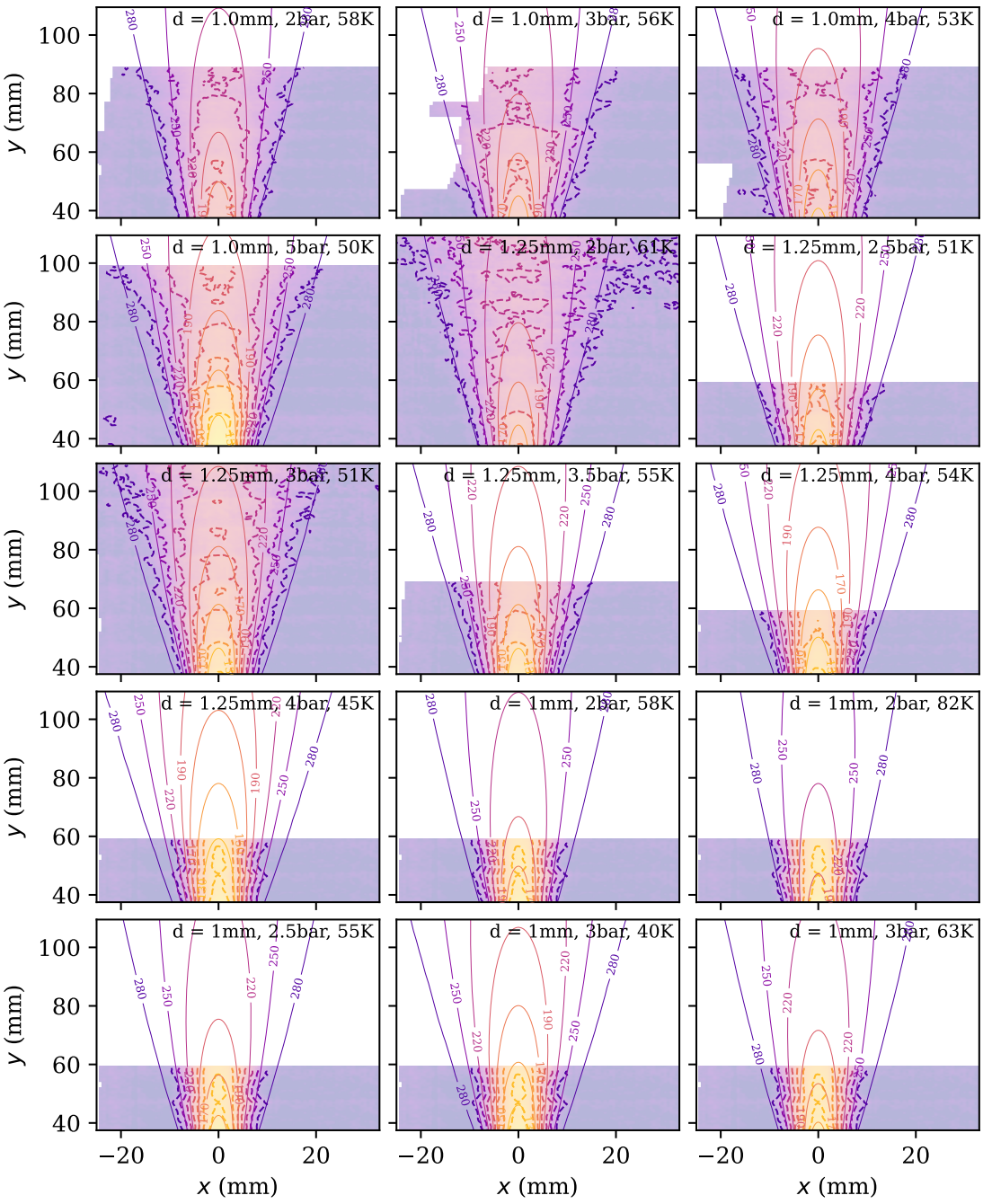
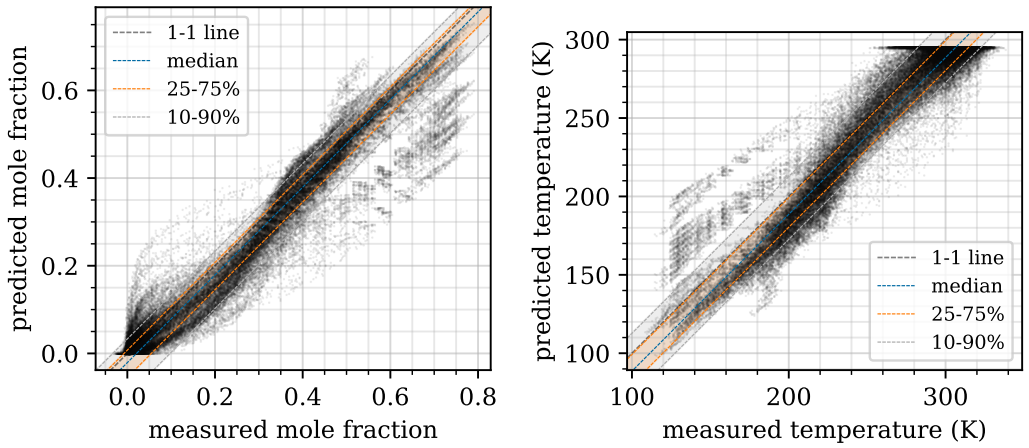


Figure 3-27 Comparison of temperatures calculated by HyRAM+ (thin, solid lines) to cryogenic hydrogen dispersion data reported by Hecht and Panda [44] and Ehrhart et al. [15] (thick, dashed lines and background shading). In many cases, data was limited to the near-nozzle region, and areas with a white background indicate that there is no experimental data. Temperatures (K) are indicated on the contours.

In these figures, the data are shown by the background shading and thick, dashed lines while the HyRAM+ predictions are shown by the thinner, solid lines. While the data is somewhat noisy, HyRAM+ predicts the mole fraction and temperature contours with reasonable accuracy.

The same data from Figures 3-26 and 3-27 are plotted in Figure 3-28. In Figure 3-28, the measured and predicted mole fraction (Figure 3-28a) or temperature (Figure 3-28b) are plotted for each pixel.



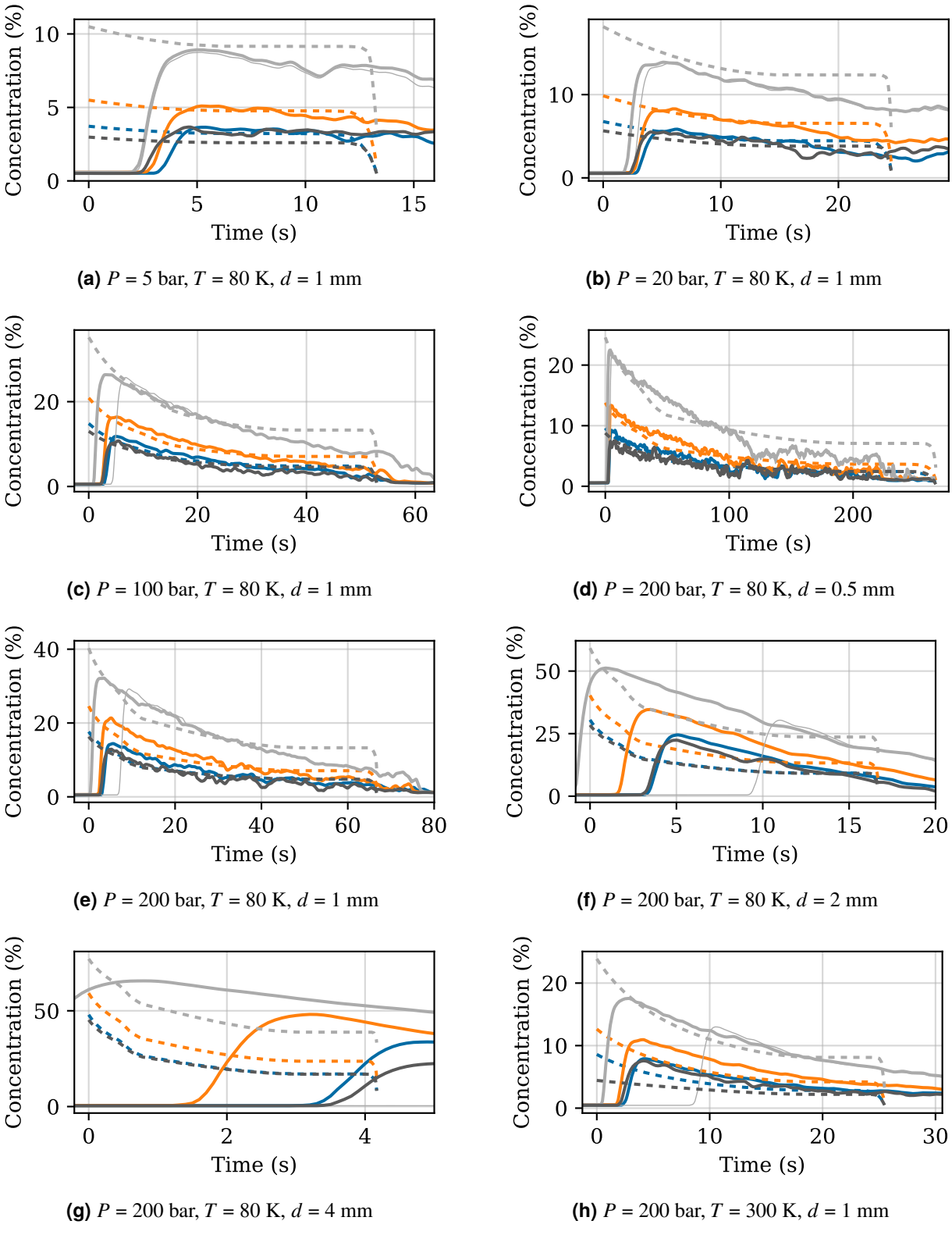
(a) mole fractions **(b)** temperatures

Figure 3-28 Correlation of data to HyRAM+ for all diameters, pressures, temperatures shown in Figures 3-26 and 3-27 (each point for counting purposes is a 0.5 mm × 0.5 mm pixel)

If the mole fraction or temperature were perfectly predicted by HyRAM+, all points would fall exactly on the 1-1 line. The median, quartiles, and 10–90% bins are only for areas where the simulated mole fraction is above 0.001 (0.1%) or the simulated temperatures are below 293 K to prevent data skewing resulting from the large amount of data near a hydrogen mole fraction of zero or room temperature. The median predicted mole fraction is 0.014 (1.4%) lower than the measured mole fraction, while the median predicted temperature is 11.3 K lower than the measured temperature. The middle 50% (25–75%) of the predicted mole fractions are within +0.0046/-0.047 of those measured, while 50% of the temperatures are between 1 K and 19 K lower than the measured temperatures. The middle 80% (10–90%) of the simulated mole fractions are within +0.028/-0.088 of the measured mole fractions, and 80% of the simulated temperatures are within +11/-27 K of the measured temperatures. This demonstrates that in general, both mole fraction and temperature predictions are lower than those measured. This could lead to a slightly non-conservative risk prediction for mole fraction (shorter distance to a given concentration), but the magnitude of the error is acceptable, especially given the experimental accuracy.

3.5.2.4. Friedrich et al. (2019)

The discharge experiments described in Section 3.5.1 performed under the PreSLHy project [42] also included measurements of concentration and temperature at several locations outside the pressure vessel. A series of pseudo-steady state HyRAM+ jet simulations were used to calculate predicted mole fractions and temperatures outside the vessel during these blowdowns.



(a) P = 5 bar, T = 80 K, d = 1 mm

(b) P = 20 bar, T = 80 K, d = 1 mm

(c) P = 100 bar, T = 80 K, d = 1 mm

(d) P = 200 bar, T = 80 K, d = 0.5 mm

(e) P = 200 bar, T = 80 K, d = 1 mm

(f) P = 200 bar, T = 80 K, d = 2 mm

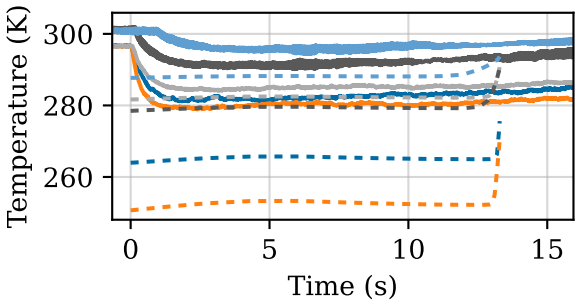
(g) P = 200 bar, T = 80 K, d = 4 mm

(h) P = 200 bar, T = 300 K, d = 1 mm

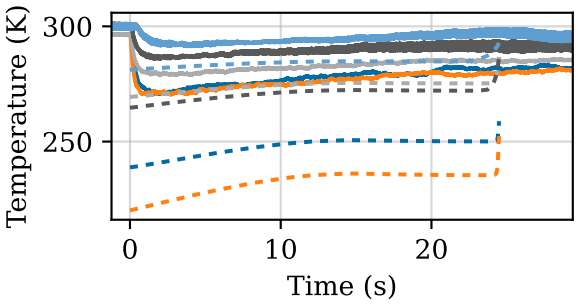
Figure 3-29 Data from Friedrich et al. [42] (solid lines) compared to HyRAM+ (dashed lines) showing molar concentrations during discharge. Each color indicates a different (r, z) location, where r is the distance from the centerline and z is the downstream distance: (0 cm, 150 cm) in blue, (0 cm, 100 cm) in orange, (0 cm, 50 cm) in light gray, and (10 cm, 100 cm) in dark gray. The thin light gray line denotes a different cut on the extraction probe at the (0 cm, 50 cm) location.

Figure 3-29 shows the molar concentration at several locations outside the vessel during the discharge. The HyRAM+ simulations to which these measurements are compared (dashed lines) are a series of pseudo-steady-state simulations using the tank conditions predicted at multiple times during the blowdowns (i.e., steady-state jet models of the conditions are shown by the dashed lines in Figures 3-21 and 3-22). In all cases (including the 300 K release, Figure 3-29h), the concentrations initially peak and then decays back towards zero. There is clearly a time lag in the concentration measurements, as the measured concentrations do not increase exactly at time zero (this is especially evident in Figure 3-29g where the flow time is short). However, generally the mole concentration measurements agree reasonably well with the model, regardless of the orifice diameter, initial pressure, or initial temperature. Figures 3-29f and 3-29g show the poorest agreement with the model, likely due to the short blowdown time and the time lag, low speed data collection, and averaging by the concentration sensors due to transport through the extraction lines and sensor response time.

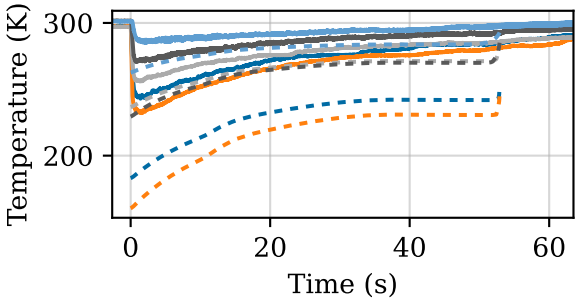
Figure 3-30 shows the temperature at several locations outside the vessel during the discharge. Similar to the concentrations (Figure 3-29), the HyRAM+ simulations to which these measurements are compared (dashed lines) are a series of pseudo-steady-state simulations using the tank conditions predicted at multiple times during the blowdowns. Analogous to the concentration data (Figure 3-29), the temperatures initially drop and then rise back towards ambient, even for the ambient temperature release (Figure 3-30h). The temperatures outside of the vessel measured experimentally are generally higher than those predicted by HyRAM+. However, the level of agreement with the experiment improves as the orifice diameter increases (e.g., Figure 3-30g). This may indicate that the thermal mass/heat capacity of the thermocouples is important, such that the measured temperatures are not indicative of the actual gas temperature for smaller leaks since these correlate with lower pressures or higher initial temperatures. In these situations, there may not be sufficient flow for the thermocouple to register the lower temperatures. The disagreement in measured and predicted temperatures could also arise from the HyRAM+ model assumptions of isentropic flow through the nozzle and an adiabatic tank, as the temperatures in the vessel and nozzle were also predicted to be lower than those measured experimentally (Figure 3-22). This is especially obvious for the orange and blue data lines, which show some of the largest discrepancies between the experiment data and HyRAM+, which indicate the sensor locations closest to the release point ((r, z) = (0 cm, 25 cm) and (2 cm, 20 cm)). The HyRAM+ assumptions leading to lower gas temperature predictions would be most pronounced in these cases, which explains the more pronounced discrepancy.



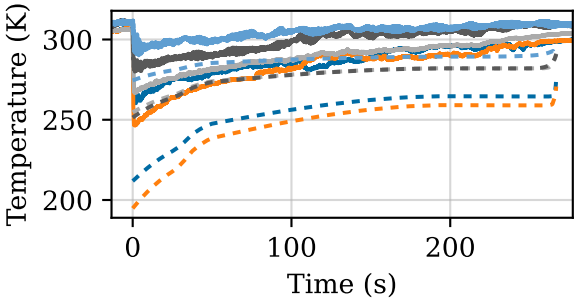
(a) P = 5 bar, T = 80 K, d = 1 mm



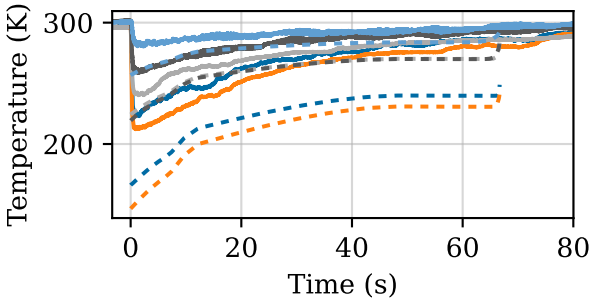
(b) P = 20 bar, T = 80 K, d = 1 mm



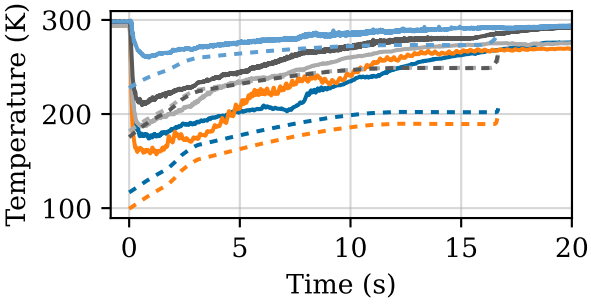
(c) P = 100 bar, T = 80 K, d = 1 mm



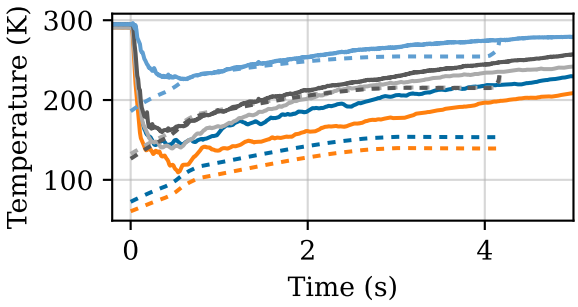
(d) P = 200 bar, T = 80 K, d = 0.5 mm



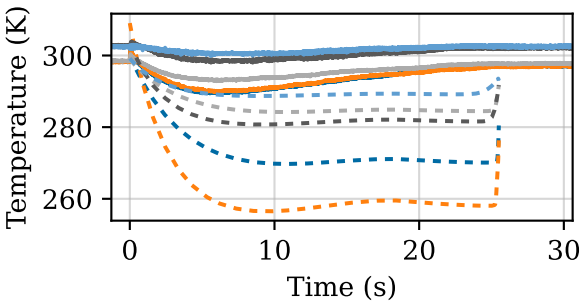
(e) P = 200 bar, T = 80 K, d = 1 mm



(f) P = 200 bar, T = 80 K, d = 2 mm



(g) P = 200 bar, T = 80 K, d = 4 mm



(h) P = 200 bar, T = 300 K, d = 1 mm

Figure 3-30 Data from Friedrich et al. [42] (solid lines) compared to HyRAM+ (dashed lines) showing temperatures outside the vessel during discharge. Each color indicates a different (r, z) location, Each color indicates a different (r, z) location, where r is the distance from the centerline and z is the downstream distance: (2 cm, 20 cm) in dark blue, (0 cm, 25 cm) in orange, (5 cm, 50 cm) in light gray, (5 cm, 50 cm) in dark gray, and (0 cm, 175 cm) in light blue.

3.5.2.5. Cryogenic Unignited Jet Plumes Summary

In general, HyRAM+ accurately predicts the concentrations and concentration decay for unignited jet plumes from cryogenic releases, but predicts lower temperatures than those measured experimentally.

3.5.3. Ignited Jet Fires

Table 3-8 lists the table that was used as validation for the ignited jet fire model for cryogenic releases in HyRAM+.

Table 3-8 Cryogenic Ignited Jet Plumes Validation Data Sources

Author(s)	Year	Figure/Table Number	Report Section
Panda and Hecht [43]	2017	Table 3	3.5.3.1

3.5.3.1. Panda and Hecht (2017)

Panda and Hecht [43] measured lab scale hydrogen flames with release temperatures from 46–295 K, nozzles from 0.75–1.25 mm, and pressures from 1–5 barg. Table 3-8 lists the tables and figures used as validation for the blowdown model. The HyRAM+ predicted flame lengths are shown relative to the measured flame lengths in Figure 3-31.

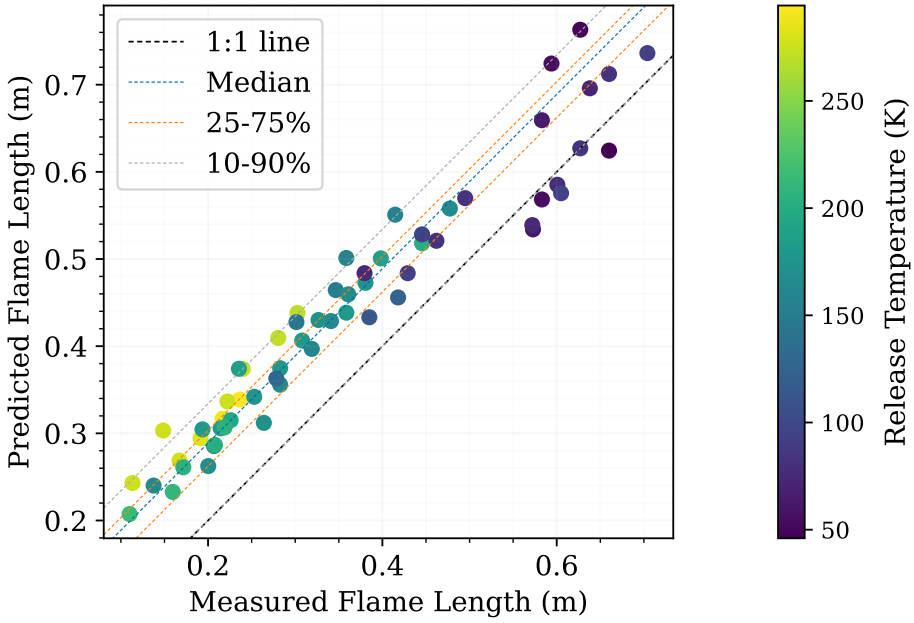


Figure 3-31 Comparison of flame length calculated by HyRAM+ to those measured by Panda and Hecht [43]

Similar to Figures 3-26 and 3-27, the median, middle 50% and middle 80% of the data are also shown in Figure 3-31. Most of the predicted flame lengths are above the measured flame lengths; The median predicted length is 9 cm longer, the length of the middle 50% of the data are 6–10 cm longer, and the middle 80% of the data are 0–13 cm longer. These longer predicted flame lengths will result in conservative predictions of risk.

Panda and Hecht [43] also measured the radiant heat flux from cryogenic hydrogen flames, with the conditions listed previously (diameters of 0.75–1.25 mm at 46–295 K and 1–5 barg). Calculated heat fluxes for each of the radiometers used in the experiments are shown as a function of the measured heat flux in Figure 3-32.

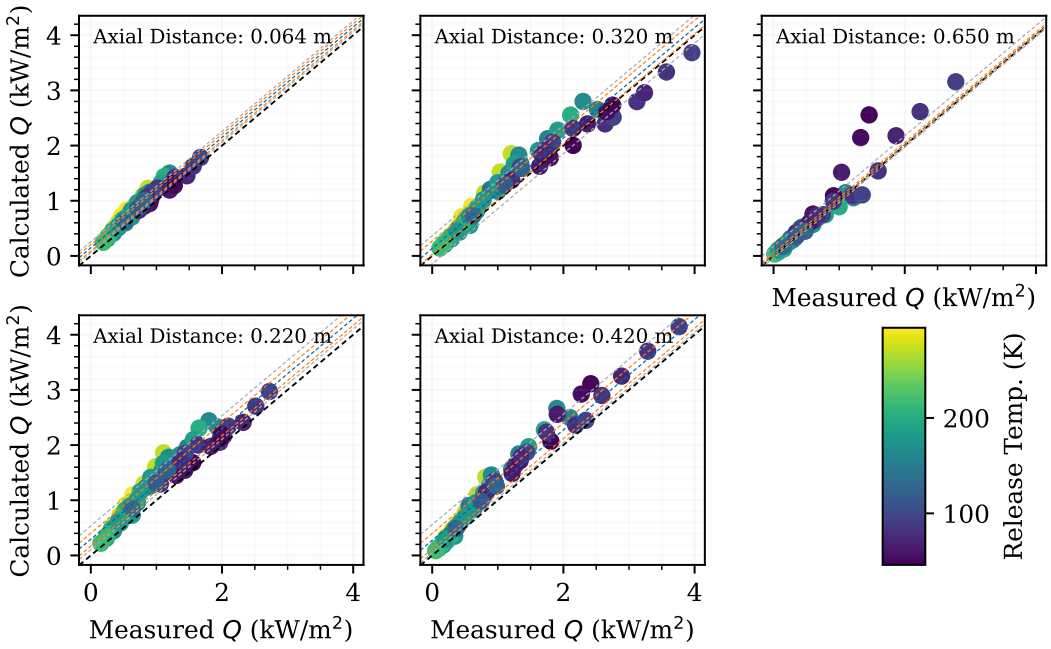


Figure 3-32 Comparison of heat flux (Q) at various distances calculated by HyRAM+ and measured by Panda and Hecht [43]

The majority of the heat fluxes calculated by HyRAM+ are larger than the values in the literature, including the median values. The middle 50% of the heat fluxes from HyRAM+ are larger than the measured values, and only at axial distances of 0.32 m and 0.65 m are more than 10% of the HyRAM+ heat fluxes lower than the measured heat fluxes (the lowest teal data points are slightly below the 1:1 lines). Similar to the flame lengths, a larger calculated heat flux will result in a conservative estimate when assessing the hazard of a cryogenic hydrogen flame.

3.6. Unconfined Overpressure from Jet Releases

Table 3-9 lists the tables and figures that were used as validation for the unconfined overpressure model in HyRAM+.

Table 3-9 Unconfined Overpressure Validation Data Sources

Author(s)	Year	Figure/Table Number	Report Section
Bauwens and Dorofeev [18]	2019	Figure 9	3.6.1
Jallais et al. [19]	2018	Figure 22, Table 2	3.6.3
Kobayashi et al. [45]	2020	Figure 8, Table 1	3.6.2
Royle and Willoughby [46]	2011	Table 1	3.6.4
Takeno et al. [47]	2007	Figures 13, 16	3.6.5
Huéscar Medina et al. [48]	2020	Figure 148	3.6.6

The unconfined overpressure models in HyRAM+ calculate the peak overpressure as a function of distance from some origin of the overpressure blast wave. HyRAM+ currently has two options available in its overpressure calculations: setting the origin of the overpressure event at the orifice of the jet release, or calculating the origin location as half the distance to the lower flammability limit along the jet streamline. The latter results in shorter distances between the origin and overpressure measurement locations. When assuming the same distance from the origin, this results in higher overpressure values compared to origins at the orifice. Unless the literature is unambiguous about the origin point, this report presents the overpressure results from both of these options in the figures and tables below, designated as "origin at orifice" and "calculated origin" respectively.

3.6.1. Bauwens and Dorofeev (2019)

Bauwens and Dorofeev [18] defined the Bauwens method described above and compared the results of the prediction method to data from Miller et al. [49]. The Miller et al. experiment measured the overpressure when hydrogen was released from a tank at a pressure of 600 kPa at a temperature of 300 K after a two second ignition delay through a horizontal vent pipe. Figure 3-33 compares the peak overpressure from the Bauwens data to the method predicted in HyRAM+.

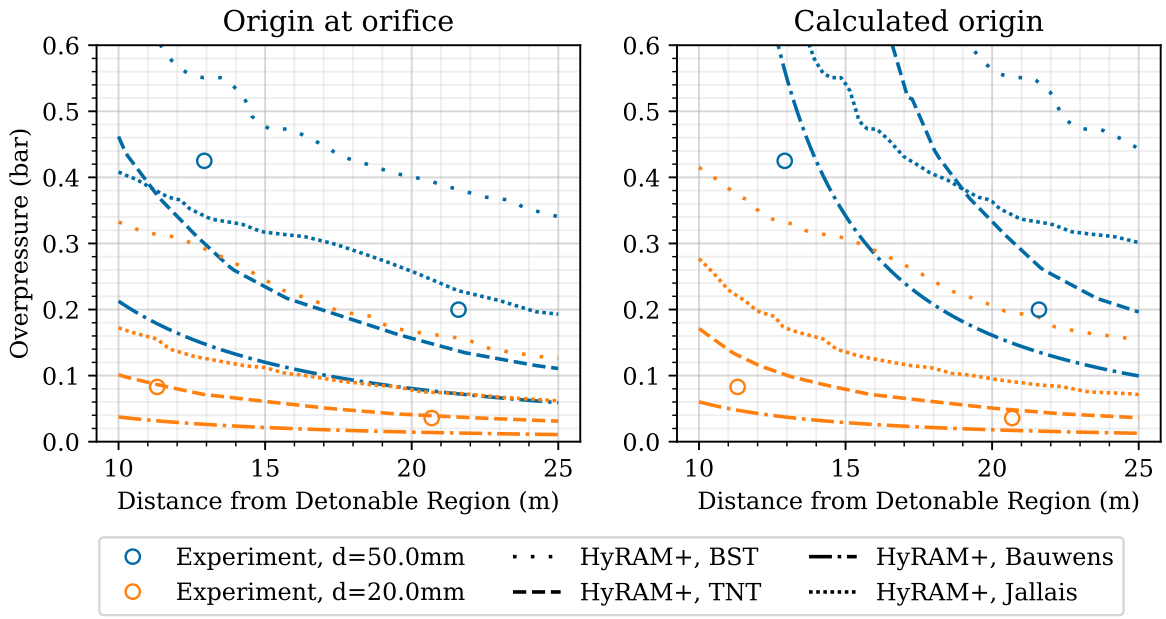


Figure 3-33 Peak unconfined overpressure predictions for different sensors from experiments cited in Bauwens and Dorofeev [18] (circles) compared to HyRAM+ predictions (lines)

For the results with the origin at the orifice, the TNT equivalence and Jallais methods are the closest to the data, the BST method overpredicts, and the Bauwens method underpredicts. The scaling of the errors of each method is similar for both nozzle diameters tested; e.g., the Bauwens method predicts about half of the overpressure compared to experiments across all sensor locations when the origin is located at the orifice. The calculated origin results show much improved agreement with the Bauwens method, while all other methods overpredict the experimental data, particularly the BST method.

3.6.2. Kobayashi et al. (2020)

Kobayashi et al. [45] performed experiments assessing the unconfined ignition of releases from fuel cell vehicle tanks. The experiment leaked hydrogen from a cryogenic 80 MPa tank. Four leak nozzle sizes were used, ranging from 0.2 mm to 1.0 mm. Only results from the middle igniter position (0.520 m from nozzle) are assessed here, as overpressures from the other igniter positions were not reported in the literature. Given the distance from the nozzle to the igniter, the overpressure origin is calculated by HyRAM+, and the "origin at orifice" option is ignored. Figure 3-34 shows the comparison of the data in Figure 8 from [45] to the methods in HyRAM+, which only shows data from the 0.7 mm nozzle.

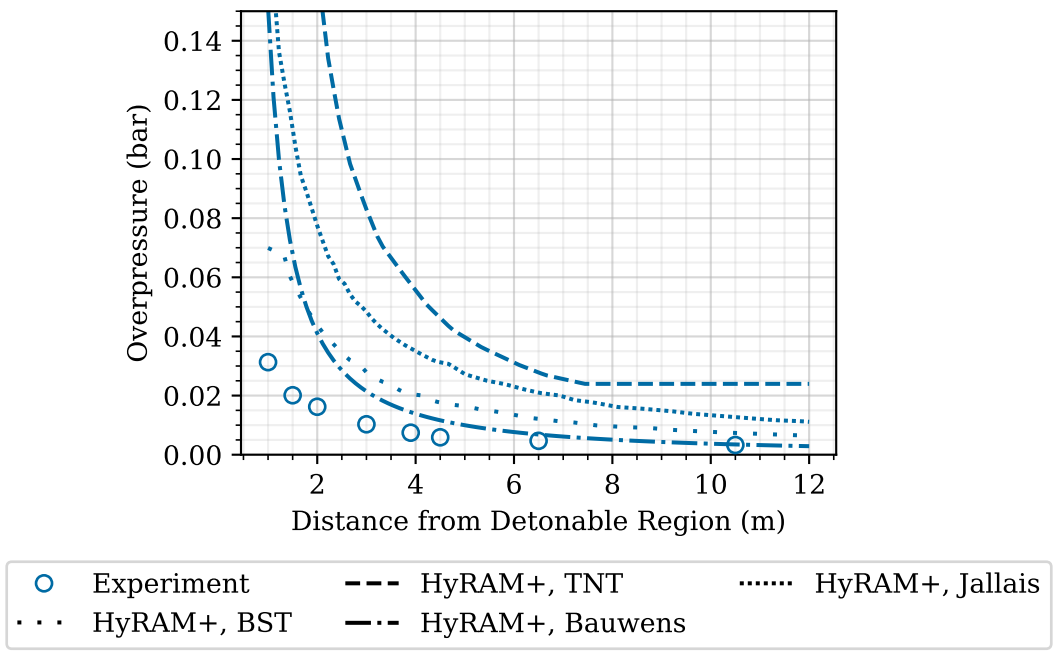


Figure 3-34 Peak unconfined overpressure predictions comparing sensors in Kobayashi et al. [45] (circles) to HyRAM+ predictions (lines)

The comparison in Figure 3-34 shows all HyRAM+ methods tend to overpredict the test data, with the nearest distances showing the greatest difference and the furthest sensor locations showing only marginal difference as overpressure diminishes and pressures approach ambient levels. Again, the Bauwens method predicts the lowest overpressures of the four models included in HyRAM+, albeit still overpredicting the experimental data. The BST method is much closer to the experimental data than in Figure 3-33 due to the selection of a different Mach flame speed in the HyRAM+ testing.

Table 3-10 compares the distances to a 1 kPa overpressure in the [45] versus the analogous predictions in HyRAM+. Note that the table does not include results from the Bauwens method, as the nozzle diameter and pressure differentials are too small for the Bauwens method to calculate any flammable mass.

Table 3-10 Comparison of distances to a 1 kPa overpressure found in Kobayashi et al. [45] to the unconfined overpressure methods in HyRAM+. The HyRAM+ calculations use the calculated origin assumption. These data exclude the Bauwens method, which is unable to calculate overpressure for these inputs

Nozzle Dia. [mm]	Pressure [kPa]	Temp. [K]	Distance, Test [m]	Distance, BST [m]	Distance, TNT [m]	Distance, Jallais [m]
0.2	39.6	60	0.12	0.22	0.22	0.40
0.2	80	67	0.28	0.22	0.22	0.39
0.4	39	62	0.6	0.43	0.42	0.77
0.4	62	67	0.58	0.43	0.42	0.76
0.4	80	70	0.83	0.43	0.42	0.76
0.4	81.5	70.5	0.95	0.43	0.42	0.76
0.4	20.5	63.5	0.22	0.41	0.40	0.73
0.4	41	58.5	0.5	0.46	0.44	0.81
0.4	60.5	61	0.66	0.46	0.45	0.82
0.4	81.2	69.5	0.7	0.43	0.42	0.77
0.7	20	78	0.79	0.62	0.60	1.09
0.7	39.5	71	1.85	0.69	0.67	1.23
0.7	60	70	2.95	0.72	0.70	1.29
0.7	64	66	2.9	0.76	0.74	1.36
0.7	59	65	3.1	0.76	0.74	1.36
0.7	20.2	76	0.9	0.63	0.61	1.12
0.7	39	65	1.85	0.73	0.71	1.31
0.7	48	61	2.22	0.78	0.76	1.39
0.7	62	61.5	3.55	0.80	0.78	1.42
0.7	49	75	1.89	0.67	0.66	1.20
0.7	66	70	3.24	0.73	0.71	1.30
0.7	40	64	1.75	0.74	0.72	1.33
0.7	40	64	1.75	0.74	0.72	1.33
0.7	40	64	1.78	0.74	0.72	1.33
1	19.8	66	2.2	0.99	0.97	1.77
1	39	61.5	4.2	1.09	1.06	1.94
1	19.4	58	2	1.09	1.06	1.94
1	36.7	57	3.48	1.15	1.12	2.05
1	29	65	3.55	1.03	1.00	1.83
1	36	61	3.64	1.09	1.06	1.94

The trends in Table 3-10 show HyRAM+ predicts a longer distance to 1 kPa for the 0.2 mm nozzle diameters, then generally a shorter distance for all the larger diameters. This again indicates HyRAM+ significantly overpredicts overpressure for close distances within a few meters of the origin. Exceptions occur with the lower relative pressures near 20 kPa. The Jallais method is generally the closest to experimental values for larger nozzle diameters, though it still

underpredicts the distance by at least 50% for all pressures above 20 kPa. The BST and TNT equivalence methods give nearly the same predictions across all inputs.

3.6.3. Jallais et al. (2018)

Jallais et al. [19] contains results from experiments conducted by DNV-GL (now DNV), again based on the test setup from Miller et al. [49]. Additionally, the authors estimated overpressure for a free unconfined jet explosion from a 2 in. (5.1 cm) leak in a hydrogen process plant at 30 barg derived using the Jallais method, assuming the detonable region begins at the nozzle. For completeness, this HyRAM+ report assesses the predictions against the other three methods available in the software. The data from the experimental test and the Jallais method predictions from the publication are combined in Figure 3-35 below since the two datasets use the same nozzle sizes in the same experimental conditions.

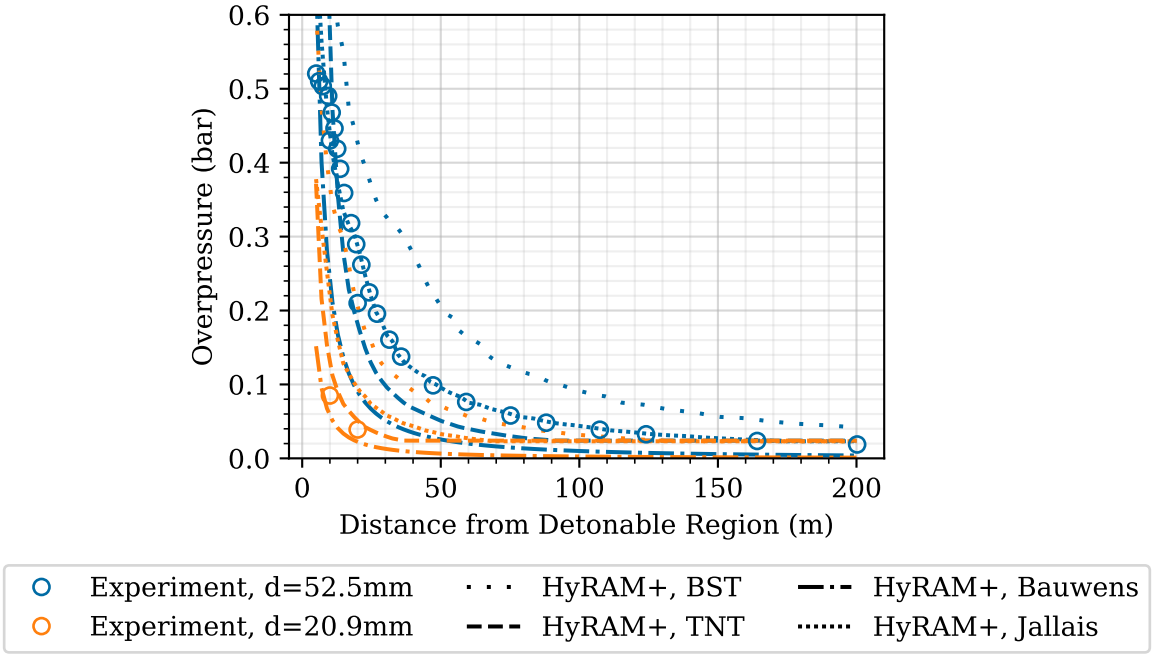


Figure 3-35 Peak unconfined overpressure predictions comparing calculations from Jallais et al. [19] matching the Jallais method (circles) to HyRAM+ predictions (lines)

The results from all HyRAM+ methods align relatively well to the experimental data, though the BST method again has the largest overprediction. The Jallais method is an exact match for the 52.5 mm diameter[2], but the method overpredicts the smaller nozzle diameter. The Bauwens method matches the test data much better for the 20.9 mm diameter than the 52.5 mm diameter.

[2]This is expected since this experiment is used to calibrate the Jallais method presented in [19], although the flammable mass is still calculated with HyRAM+.

3.6.4. Royle and Willoughby (2011)

Royle and Willoughby [46] performed tests as part of the EU Hyper project, and focused on fuel cell systems with larger pipe diameters than available in literature at the time of publication. The authors tested with a variety of flow restrictors creating a release nozzle of 1.5 mm, 3.2 mm, 6.4 mm, and full bore diameter of 9.5 mm. The 1.5 mm diameter nozzle could not detect any readable overpressure, thus the corresponding data are excluded here. Hydrogen was released at 1.2 m elevation from a 205 bar tank at ambient temperature with either a 400 or 800 ms ignition delay after release, with the nearest sensor 2.8 m downstream and 1.5 m lateral of the nozzle. Table 3-11 shows the comparison from the test results to HyRAM+ overpressure calculations.

Table 3-11 Comparison of peak unconfined overpressure (abbreviated as "OP") predictions from tests in Royle and Willoughby [46] with HyRAM+ calculations. The HyRAM+ calculations consider both the "origin at orifice" (OAO) and "calculated origin" (CO) options for origin location, separated by a "|"

Test #	Nozzle dia. [mm]	Ignition delay [ms]	OP, Test [mbar]	OP, BST [mbar] (OAO|CO)	OP, TNT [mbar] (OAO|CO)	OP, Bauwens [mbar] (OAO|CO)	OP, Jallais [mbar] (OAO|CO)
13	3.2	800	35	32 | 41	97 | 144	24 | 35	53 | 69
20	3.2	400	21	32 | 41	97 | 144	24 | 35	53 | 69
14	6.4	800	152	58 | 70	268 | 719	88 | 188	107 | 173
19	6.4	400	27	58 | 70	268 | 719	88 | 188	107 | 173
22	6.4	400	37	58 | 70	268 | 719	88 | 188	107 | 173
15	9.5	800	165	224 | 218	540 | 2304	179 | 492	152 | 225
16	9.5	400	49	224 | 218	540 | 2304	179 | 492	152 | 225
18	9.5	400	54	224 | 218	540 | 2304	179 | 492	152 | 225
23	9.5	400	33	224 | 218	540 | 2304	179 | 492	152 | 225

HyRAM+ shows identical results for identical nozzle diameter tests, since HyRAM+ assumes the jet flow is fully developed at time of ignition without explicitly considering ignition delay. The different HyRAM+ overpressure models vary drastically compared to each other and to the experimental data. Notably, the TNT equivalence method predicts extremely high overpressure for the "calculated origin" (CO) option. This is because the TNT equivalence method and (to a lesser degree) Bauwens method increases overpressure asymptotically when approaching the origin point, and the HyRAM+ calculated origin is very close to the sensor location for this test, resulting in the extreme predictions presented here. Alternatively, the predictions using the BST and Jallais methods are much closer to the experimental data, although both methods still significantly overpredict for the 9.5 mm nozzle, by up to 400% for the 400 ms ignition delay. The 800 ms ignition delay results in far higher overpressures than the 400 ms delay, though both ignition delays are very short compared to other literature. The very large discrepancies in HyRAM+ are likely due to the assumption that the jet is fully developed at ignition time. The physics of less developed flows immediately following ignition are complex and requires high

fidelity computational fluid dynamics (CFD) models, which extends beyond the fidelity HyRAM+ is designed to simulate.

3.6.5. Takeno et al. (2007)

Takeno et al. [47] conducted early experiments emulating the rupture of a high-pressure pipe carrying hydrogen at a fuel cell refueling station for small vehicles. Hydrogen was released from nozzles at a 1 m elevation with diameters ranging from 1 mm to 10 mm from a stainless steel cylinder at 40 MPa. The comparisons to HyRAM+ results are split into two figures (Figure 3-36 and Figure 3-37) for improved readability due to the scale differences in the overpressure results. The data from [47] includes points from Figures 13 and 16 from the original manuscript, which are combined here due to their identical test conditions.

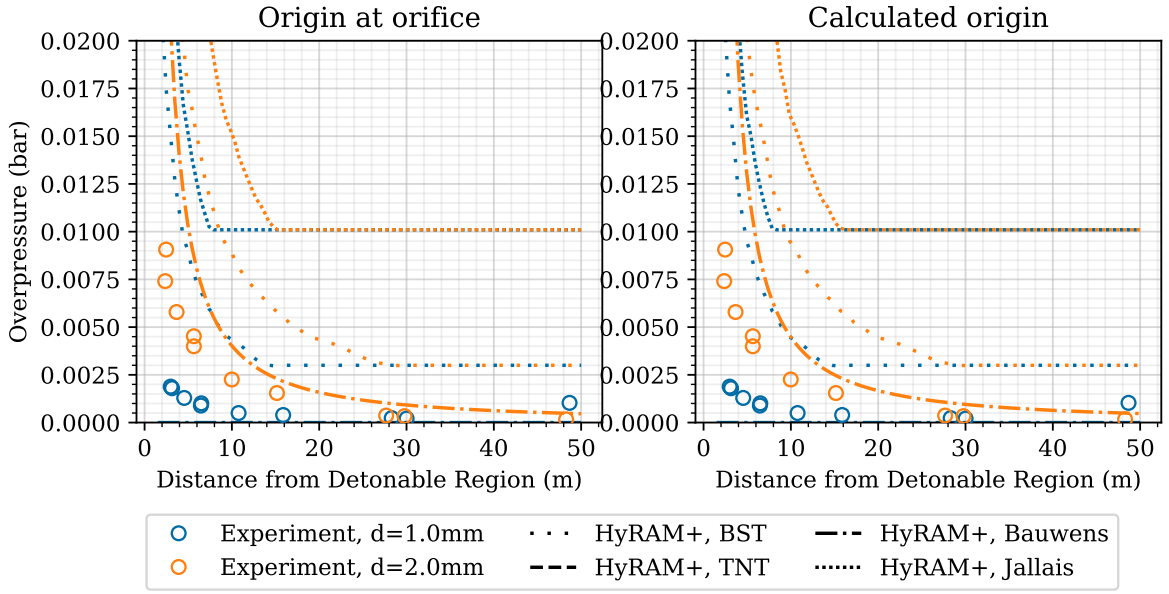


Figure 3-36 Peak unconfined overpressure predictions comparing sensors in Takeno et al. [47] (circles) to HyRAM+ predictions (lines) for 1.0 mm and 2.0 mm nozzle diameters

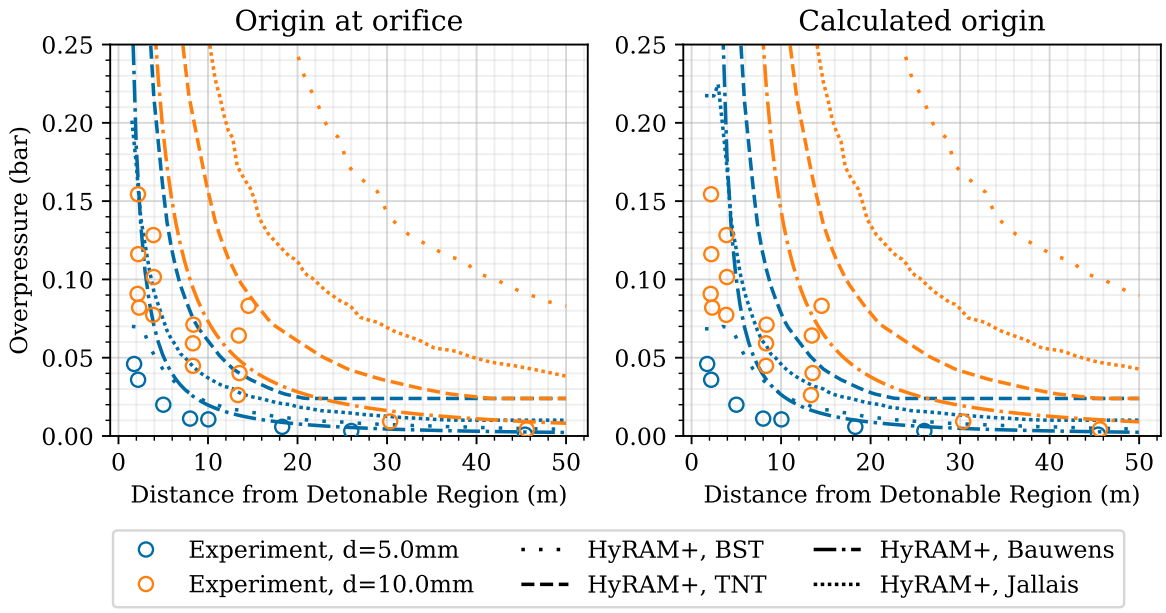


Figure 3-37 Peak unconfined overpressure predictions comparing sensors in Takeno et al. [47] (circles) to HyRAM+ predictions (lines) for 5.0 mm and 10.0 mm nozzle diameters

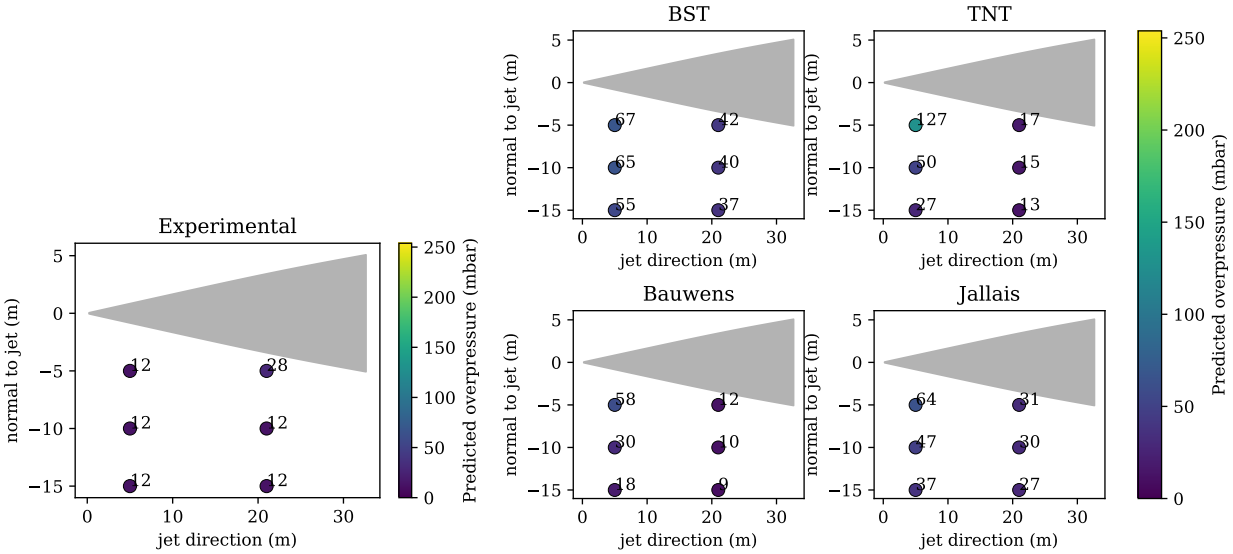
This comparison shows the largest variations between the experimental data and HyRAM+ predictions across all the gathered literature, suggesting the unconfined overpressure models in HyRAM+ are less accurate for small releases. The TNT equivalence method overpredicts the overpressure to the point of not being visible on Figure 3-36. The BST and Jallais methods overpressure predictions become constant at longer distances due to the limitation of the flame speed curves in [17]. This is because HyRAM+ holds overpressure predictions constant at the closest (lowest) value if the environmental conditions extend beyond the curves available in the literature. The Bauwens method predicts overpressures close to experimental data for 2.0 mm nozzle diameters, but cannot calculate any overpressure for the 1.0 mm nozzle, again due to calculating zero flammable mass due to the release being small and low intensity. Larger diameters are still generally overpredicted in HyRAM+ across all methods, albeit to a lesser extent than the smaller nozzle diameters. The "origin at orifice" selection aligns somewhat better than the "calculated origin" selection, particularly for the two larger nozzles, though the effects are relatively minor. Interestingly, the BST method aligns relatively closely to the experimental data for the 5.0 mm nozzle diameter data, but drastically overpredicts for the 10.0 mm diameter nozzle, likely due to the HyRAM+ test model selecting a different Mach flame speed. Overall, the Bauwens method is the only method that is generally close for both the 5.0 mm and 10.0 mm nozzles.

3.6.6. Huéscar Medina et al. (2020)

Huéscar Medina et al. [48] reported tests from seven large steady state releases of cryogenic hydrogen (to simulate a liquid hydrogen leak) oriented horizontally and vertically downward. Overpressures were measured for two of the tests: Test 05 (vertically downward release) and Test

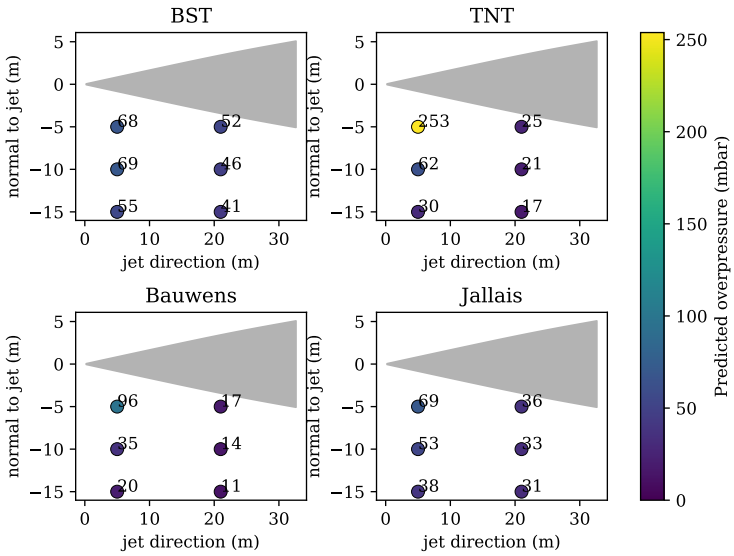
06 (horizontal release), though only Test 06 data are compared here. The vertical release in Test 05 results in a complex mixing field due to impingement of the release on the ground, which affects the flammable mass that would generate overpressure. The unconfined overpressure model in HyRAM+ assumes unconfined plume ignition, so data from Test 05 is excluded from this comparison.

Test 06 has a horizontal release at 0.49 m elevation with nozzle pressures ranging from 0.18 barg to 2.53 barg from a 1 in. (2.5 cm) diameter nozzle. Six sensors are positioned lateral to the release direction. A visualization of the experimental and HyRAM+ overpressures at these sensors is given in Figure 3-38.



(a) Experiment

(b) Origin at orifice



(c) Calculated origin

Figure 3-38 Visualization of the sensor positions and the measured and calculated peak overpressures (circles) with the gray triangle showing the release direction; data from Huéscar Medina et al. [48]

The results show a difference in the overpressure propagation between the experiment and HyRAM+. In HyRAM+, sensor 1 (top left) experiences the largest overpressures, while sensor 4 (top right) measured the largest overpressures in the test data. All models in HyRAM again overpredict the experimental data, with the TNT equivalence method having the largest error. This error is exaggerated more for the calculated origin selection; the origin location only makes a modest impact on the results for the other methods. The Bauwens method has the least error for this test, particularly for the sensors further away from the jet.

3.6.7. Unconfined Overpressure Summary

Overall, HyRAM+ moderately to severely overpredicts unconfined overpressures compared to experimental data, with more severe errors occurring compared to tests with sensors located very close (< 5 m) from the ignition location. Additionally, HyRAM+ generally overpredicts overpressure for small release nozzles (< 1.0 mm diameter), although this was not true for all experiments. HyRAM+ also shows severe overpredictions when ignition occurs very soon (< 1 s) after release, as the software assumes the jet to be fully developed at time of ignition, although short ignition delays were only from a single data source. The two origin selection strategies vary in accuracy between the different experiments from literature without a clear pattern. The accuracy of the four models vary based on the test setups in the literature:

- The Bauwens method typically best matches data from experiments with measurements 5 m or more from the origin, though limitations in the detonable mass calculation prevent the model from computing any overpressures for very small releases.
- The Jallais method best match data from experiments with measurements less than 5 m from the origin, though still substantially overpredict overpressures for larger releases at these distances.
- The BST method predictions vary widely based on the Mach flame speed selected by the user, though there does not appear to be clear guidance on which flame speeds to select when comparing to the experimental data, beyond the adjustments made for the Jallais method.
- The TNT equivalence method overpredicts the experimental data by the greatest amount of the four models.

The HyRAM+ unconfined overpressure models will generally provide moderate conservatism for predictions more than a few meters from the ignition position. Due to the variation across the different tests and methods, more experiments are needed to provide greater confidence in the HyRAM+ predictions for more diverse overpressure scenarios. Additionally, improved overpressure models–particularly for small and cryogenic releases–would be valuable towards bringing the HyRAM+ predictions closer to experiments.

It is also important to note that some measures of physical harm due to overpressure blast waves consider the impulse of the blast wave in addition to the peak overpressure. Most of the models implemented in HyRAM+ can calculate an impulse, but validation data for impulse are harder to collect and thus less likely to be reported in the literature. Future improvements to this validation effort could include a more detailed analysis of experimental data to incorporate impulse comparisons, and future experiments should report impulse or pressure-time history in more detail.

This page intentionally left blank.

4. CONCLUSIONS

HyRAM+ 5.1 features changes to the physics capabilities since the last validation report was published following the release of HyRAM 3.1, including modeling of alternative fuels and mixtures and prediction of unconfined overpressure events from delayed jet ignitions. This report serves to update the analysis from the previous HyRAM validation report to use the most recent version of the software at time of writing. Additionally, a new section has been added to validate the four new unconfined overpressure physics models: Baker-Strehlow-Tang (BST), TNT equivalence, Bauwens, and Jallais methods. These models were compared to experimental data from literature to demonstrate and compare their accuracy.

The blowdown (emptying) of high-pressure, room-temperature tanks predicted by HyRAM+ are compared to four literature sources in Section 3.1. Data were gathered for hydrogen tanks with initial pressures of 13.45 MPa, 15.5 MPa, 43.1 MPa, and 90 MPa. HyRAM+ predicts very similar times to empty to the experiments, though the flow rates are initially overpredicted slightly before leveling off to line up with the experimental data. The tank temperature was also monitored in one experiment, and HyRAM+ predicted much lower tank temperatures than the experimental measurements. This is likely due to gas mixing within the tank and heat loss through the tank walls, which are ignored in HyRAM+.

Mean concentrations (mole and mass fractions) during the dispersion of hydrogen are compared for a range of release scenarios in Section 3.2. HyRAM+ provides very good agreement with experimental data at predicting the mean centerline mole fractions, although far narrower Gaussian dispersion profiles are predicted than observed in experiments. Improved tuning of empirical parameter values within HyRAM+ may improve this agreement.

Flame lengths and heat fluxes for ignited high-pressure hydrogen diffusion flames are predicted and compared to a variety of literature data in Section 3.3. HyRAM+ accurately predicts the flame lengths of hydrogen diffusion flames up to 900 bar, with some minor conservatism for the corresponding heat flux predictions, particularly for releases from larger nozzles.

Accumulation within an enclosure and the overpressure that would result if the accumulated hydrogen were to ignite are compared to several literature sources in Section 3.4. HyRAM+ predicts concentrations and overpressures that are similar to literature data, but there is considerable variability in accuracy depending on the experimental setup. HyRAM+ also conservatively predicts the overpressure that would result from the ignition of an accumulated mixture within an enclosure both with and without ventilation, though there was only a single literature source for this comparison.

HyRAM+ is compared to literature data for cryogenic releases of hydrogen in Section 3.5. Similar to the room-temperature blowdown simulations, HyRAM+ predicts the pressure decay from the tank emptying fairly accurately, but predicts temperatures in the tank that are much lower than the measured experimental data. HyRAM+ also predicts significant differences in the pressure and temperature in the orifice versus the tank despite experiments measuring similar pressures and temperatures at the two locations. HyRAM+ predicts centerline concentration decay and even two-dimensional near-field concentration fields of unignited jets accurately. HyRAM+ tends to slightly overpredict concentration in most cases, while some temperature measurements were

higher and some lower than those predicted. In most of the experiments, the temperature measurements had more uncertainty than the concentration measurements. Similar to the warm releases, HyRAM+ also predicts slightly longer visible flame lengths and heat fluxes than were measured experimentally.

Finally, overpressures resulting from the ignition of unconfined jet releases of hydrogen are compared to literature in Section 3.6. The test conditions from the experiments vary considerably, complicating comparisons across literature sources and to HyRAM+ results. However, HyRAM+ generally shows moderate overprediction against the majority of the validation data, providing some conservatism to the calculations. HyRAM+ severely overpredicts overpressure within about 5 m of the ignition point and for some release from nozzles less than 1.0 mm in diameter, though the latter finding is based on a small number of data sources and requires further investigation. The Bauwens method generally performs the best except for very small nozzle sizes, while the TNT equivalence method consistently has the greatest amount of overprediction. HyRAM+ predicts large differences for most overpressures for very short delay ignitions (< 1 s) due to the assumption that the jet is fully developed at time of ignition.

Overall, the validation results are generally unchanged between HyRAM 3.1 and HyRAM+ 5.1 for the physics models published in the previous HyRAM validation report. The new unconfined overpressure models generally provide a reasonable amount of conservatism compared to most experimental test data, though there are more significant differences for predictions with very short ignition delays and/or within about 5 m of the ignition location. Further validation and model improvements should be performed as additional literature emerges for these releases to reduce the amount of conservatism and provide greater precision in the models.

REFERENCES

[1] K. M. Groth, E. S. Hecht, and J. T. Reynolds, "Methodology for assessing the safety of Hydrogen Systems: HyRAM 1.0 technical reference manual," Sandia National Laboratories, Albuquerque, NM, SAND2015-10216, 2015. DOI: 10.2172/1814840.

[2] K. M. Groth, E. S. Hecht, J. T. Reynolds, M. L. Blaylock, and E. E. Carrier, "Methodology for assessing the safety of Hydrogen Systems: HyRAM 1.1 technical reference manual," Sandia National Laboratories, Albuquerque, NM, SAND2017-2998, 2017. DOI: 10.2172/1365456.

[3] G. Feliciano Morales, B. D. Ehrhart, and A. B. Muna, "HyRAM V2.0 User Guide," Sandia National Laboratories, Albuquerque, NM, SAND2019-8940, 2019. DOI: 10.2172/1762969.

[4] B. D. Ehrhart and E. S. Hecht, "Hydrogen Risk Assessment Models (HyRAM) Version 3.0 Technical Reference Manual," Sandia National Laboratories, Albuquerque, NM, SAND2020-10600, 2020. DOI: 10.2172/1673177.

[5] B. D. Ehrhart and E. S. Hecht, "Hydrogen Risk Assessment Models (HyRAM) Version 3.1 Technical Reference Manual," Sandia National Laboratories, Albuquerque, NM, SAND2021-5812, 2021. DOI: 10.2172/1784842.

[6] E. Hecht, B. Ehrhart, and K. M. Groth, "Hydrogen Plus Other Alternative Fuels Risk Assessment Models (HyRAM+) Technical Reference Manual V.4," Sandia National Laboratories, Tech. Rep. SAND2021-14813, Nov. 2021. DOI: 10.2172/1832082.

[7] B. D. Ehrhart and E. S. Hecht, "Hydrogen Plus Other Alternative Fuels Risk Assessment Models (HyRAM+) Version 4.1 Technical Reference Manual," Sandia National Laboratories, Tech. Rep. SAND2022-5649, Apr. 2022. DOI: 10.2172/1865723.

[8] B. D. Ehrhart and E. S. Hecht, "Hydrogen Plus Other Alternative Fuels Risk Assessment Models (HyRAM+) Version 5.0 Technical Reference Manual," Sandia National Laboratories, Tech. Rep. SAND2022-16425, Nov. 2022. DOI: 10.2172/1900089.

[9] B. D. Ehrhart, E. S. Hecht, and B. B. Schroeder, "Hydrogen Plus Other Alternative Fuels Risk Assessment Models (HyRAM+) Version 5.1 Technical Reference Manual," Sandia National Laboratories, Tech. Rep. SAND2023-14224, Dec. 2023. DOI: 10.2172/2369637.

[10] W. Houf and R. Schefer, "Analytical and experimental investigation of small-scale unintended releases of hydrogen," *International Journal of Hydrogen Energy*, vol. 33, no. 4, pp. 1435–1444, 2008. DOI: 10.1016/j.ijhydene.2007.11.031.

[11] W. S. Winters, "Modeling Leaks from Liquid Hydrogen Storage Systems," Sandia National Laboratories, SAND2009-0035, 2009. DOI: 10.2172/986606.

[12] W. Houf and W. Winters, "Simulation of high-pressure liquid hydrogen releases," *International Journal of Hydrogen Energy*, vol. 38, no. 19, pp. 8092–8099, 2013. DOI: 10.1016/j.ijhydene.2013.01.052.

[13] I. Ekoto, A. Ruggles, L. Creitz, and J. Li, "Updated jet flame radiation modeling with buoyancy corrections," *International Journal of Hydrogen Energy*, vol. 39, no. 35, pp. 20 570–20 577, 2014. DOI: 10.1016/j.ijhydene.2014.03.235.

[14] G. Hankinson and B. J. Lowesmith, "A consideration of methods of determining the radiative characteristics of jet fires," *Combustion and Flame*, vol. 159, no. 3, pp. 1165–1177, 2012. DOI: 10.1016/j.combustflame.2011.09.004.

[15] B. D. Ehrhart, E. S. Hecht, and J. A. Mohmand, "Validation and comparison of hyram physics models," Sandia National Laboratories, Tech. Rep. SAND2021-5811, May 2021. DOI: 10.2172/1813659.

[16] Q. Guo, E. S. Hecht, M. L. Blaylock, J. G. Shum, and C. Jordan, "Physics model validation of propane and methane for hydrogen plus other alternative fuels risk assessment models (hyram+)," *Process Safety and Environmental Protection*, vol. 173, pp. 22–38, 2023. DOI: 10.1016/j.psep.2023.02.073.

[17] M. Tang and Q. Baker, "A new set of blast curves from vapor cloud explosion," *Process Safety Progress*, vol. 18, no. 4, pp. 235–240, 1999. DOI: 10.1002/prs.680180412.

[18] C. R. Bauwens and S. B. Dorofeev, "Quantifying the potential consequences of a detonation in a hydrogen jet release," in *Proceedings of the International Conference on Hydrogen Safety (ICHS 2019)*, Adelaide (Australia): Hydrogen Knowledge Centre, 2019, pp. 612–623.

[19] S. Jallais, E. Vyazmina, D. Miller, and J. K. Thomas, "Hydrogen jet vapor cloud explosion: A model for predicting blast size and application to risk assessment," *Process Safety Progress*, vol. 37, no. 3, pp. 397–410, 2018. DOI: 10.1002/prs.11965.

[20] A. Rohatgi. "Webplotdigitizer. "[Online]. Available: https://automeris.io/WebPlotDigitizer.

[21] I. W. Ekoto, W. G. Houf, G. H. Evans, E. G. Merilo, and M. A. Groethe, "Experimental investigation of hydrogen release and ignition from fuel cell powered forklifts in enclosed spaces," *International Journal of Hydrogen Energy*, vol. 37, no. 22, pp. 17 446–17 456, 2012. DOI: 10.1016/j.ijhydene.2012.03.161.

[22] R. Schefer, W. Houf, T. Williams, B. Bourne, and J. Colton, "Characterization of high-pressure, underexpanded hydrogen-jet flames," *International Journal of Hydrogen Energy*, vol. 32, no. 12, pp. 2081–2093, 2007. DOI: 10.1016/j.ijhydene.2006.08.037.

[23] C. Proust, D. Jamois, and E. Studer, "High pressure hydrogen fires," *International Journal of Hydrogen Energy*, vol. 36, no. 3, pp. 2367–2373, 2011. DOI: 10.1016/j.ijhydene.2010.04.055.

[24] R. Schefer, W. Houf, B. Bourne, and J. Colton, "Spatial and radiative properties of an open-flame hydrogen plume," *International Journal of Hydrogen Energy*, vol. 31, no. 10, pp. 1332–1340, 2006. DOI: 10.1016/j.ijhydene.2005.11.020.

[25] V. Molkov, *Fundamentals of Hydrogen Safety Engineering I*. bookboon.com, 2012.

[26] A. Ruggles and I. Ekoto, "Ignitability and mixing of underexpanded hydrogen jets," *International Journal of Hydrogen Energy*, vol. 37, no. 22, pp. 17 549–17 560, 2012. DOI: 10.1016/j.ijhydene.2012.03.063.

[27] S. H. Han, D. Chang, and J. S. Kim, "Release characteristics of highly pressurized hydrogen through a small hole," *International Journal of Hydrogen Energy*, vol. 38, no. 8, pp. 3503–3512, 2013. DOI: 10.1016/j.ijhydene.2012.11.071.

[28] J. Chaineaux, G. Mavrothalassitis, and J. Pineau, "Modelization and validation of the discharge in air of a vessel pressurized by flammable gas," *Progress in Astronautics and Aeronautics*, vol. 134, pp. 104–137, 1991. DOI: 10.2514/5.9781600866074.0104.0137.

[29] M. Kuznetsov, "Hydrogen distribution tests in free turbulent jet," FZK, SBEP V4, 2006.

[30] K. Okabayashi, T. Nonaka, N. Sakata, K. Takeno, H. Hirashima, and K. Chitose, "Characteristics of dispersion for leakage of high-pressurized hydrogen gas," *Japan Society for Safety Engineering*, vol. 44, pp. 391–397, 2005.

[31] E. Ruffin, Y. Mouilleau, and J. Chaineaux, "Large scale characterization of the concentration field of supercritical jets of hydrogen and methane," *Journal of Loss Prevention in the Process Industries*, vol. 9, no. 4, pp. 279–284, 1996. DOI: 10.1016/0950-4230(96)00018-6.

[32] L. Shirvill, P. Roberts, T. Roberts, C. Butler, and M. Royle, "Dispersion of hydrogen from high-pressure sources," in *Proceedings of the IChemE Symposium Hazards XIX*, Manchester, UK, 2006.

[33] A. Veser *et al.*, "The structure and flame propagation regimes in turbulent hydrogen jets," in *Proceedings of the Third International Conference on Hydrogen Safety*, Ajaccio, France, 2009. DOI: 10.1016/j.ijhydene.2010.03.123.

[34] W. Houf and R. Schefer, "Predicting radiative heat fluxes and flammability envelopes from unintended releases of hydrogen," *International Journal of Hydrogen Energy*, vol. 32, no. 1, pp. 136–151, 2007. DOI: doi.org/10.1016/j.ijhydene.2006.04.009.

[35] T. Imamura *et al.*, "Experimental investigation on the thermal properties of hydrogen jet flame and hot currents in the downstream region," *International Journal of Hydrogen Energy*, vol. 33, no. 13, pp. 3426–3435, 2008. DOI: 10.1016/j.ijhydene.2008.03.063.

[36] T. Mogi, H. Nishida, and S. Horiguchi, "Flame characteristics of high-pressure hydrogen gas jet," in *Proceedings of the first International Conference on Hydrogen Safety (ICHS 2005)*, 2005.

[37] S. Giannissi *et al.*, "CFD benchmark on hydrogen release and dispersion in a ventilated enclosure: Passive ventilation and the role of an external wind," *International Journal of Hydrogen Energy*, vol. 40, no. 19, pp. 6465–6477, 2015. DOI: 10.1016/j.ijhydene.2015.03.072.

[38] E. Merilo, M. Groethe, J. Colton, and S. Chiba, "Experimental study of hydrogen release accidents in a vehicle garage," *International Journal of Hydrogen Energy*, vol. 36, no. 3, pp. 2436–2444, 2011. DOI: 10.1016/j.ijhydene.2010.04.056.

[39] G. Bernard-Michel and D. Houssin-Agbomson, "Comparison of helium and hydrogen releases in 1 m^3 and 2 m^3 two vents enclosures: Concentration measurements at different flow rates and for two diameters of injection nozzle," *International Journal of Hydrogen Energy*, vol. 42, no. 11, pp. 7542–7550, 2017. DOI: 10.1016/j.ijhydene.2016.05.217.

[40] J. Xiao, J. Travis, and W. Breitung, "Hydrogen release from a high pressure gaseous hydrogen reservoir in case of a small leak," *International Journal of Hydrogen Energy*, vol. 36, no. 3, pp. 2545–2554, 2011. DOI: 10.1016/j.ijhydene.2010.05.069.

[41] A. Friedrich *et al.*, "Ignition and heat radiation of cryogenic hydrogen jets," *International Journal of Hydrogen Energy*, vol. 37, no. 22, pp. 17 589–17 598, 2012. DOI: 10.1016/j.ijhydene.2012.07.070.

[42] A. Friedrich, A. Vesser, and T. Jordan, *PRESLHY experiment series E3.1 (cryogenic hydrogen blow-down/discharge) results*, 2019. DOI: 10.5445/IR/1000096833.

[43] P. P. Panda and E. S. Hecht, "Ignition and flame characteristics of cryogenic hydrogen releases," *International Journal of Hydrogen Energy*, vol. 42, no. 1, pp. 775–785, 2017. DOI: 10.1016/j.ijhydene.2016.08.051.

[44] E. S. Hecht and P. P. Panda, "Mixing and warming of cryogenic hydrogen releases," *International Journal of Hydrogen Energy*, vol. 44, no. 17, pp. 8960–8970, 2019. DOI: 10.1016/j.ijhydene.2018.07.058.

[45] H. Kobayashi *et al.*, "Experimental study on cryo-compressed hydrogen ignition and flame," *International Journal of Hydrogen Energy*, vol. 45, no. 7, pp. 5098–5109, 2020. DOI: 10.1016/j.ijhydene.2019.12.091.

[46] M. Royle and D. Willoughby, "Consequences of catastrophic releases of ignited and unignited hydrogen jet releases," *International Journal of Hydrogen Energy*, vol. 36, no. 3, pp. 2688–2692, 2011. DOI: 10.1016/j.ijhydene.2010.03.141.

[47] K Takeno, K. Okabayashi, A Kouchi, T Nonaka, K Hashiguchi, and K Chitose, "Dispersion and explosion field tests for 40 mpa pressurized hydrogen," *International Journal of Hydrogen Energy*, vol. 32, no. 13, pp. 2144–2153, 2007. DOI: 10.1016/j.ijhydene.2007.04.018.

[48] C. Huéscar Medina, A. Halford, and J. Stene, "Liquid hydrogen safety data report: Outdoor leakage studies," DNV, Brampton, UK, Tech. Rep. 853182, rev. 2, 2020.

[49] D. Miller, C. Eastwood, and J. Thomas, "Hydrogen jet vapor cloud explosion: Test data and comparison with predictions," in *11th Global Congress on Process Safety, AIChE Annual Meeting*, Austin, TX, 2015.

[50] R. Schefer, W. Houf, and T. Williams, "Investigation of small-scale unintended releases of hydrogen: Momentum-dominated regime," *International Journal of Hydrogen Energy*, vol. 33, no. 21, pp. 6373–6384, 2008. DOI: 10.1016/j.ijhydene.2008.05.041.

APPENDIX A. VALIDATION DATA INPUT PARAMETERS

This section contains a summary of all inputs used in HyRAM models for comparison to experimental data. For each set of inputs, the value and unit for each parameter is given, along with the location within the cited source from which the input was obtained.

A.1. Blowdown Input Parameters

Table A-1 Ekoto et al. [21] Figure 3 Input Parameters

Parameter	Value	Units	Location
Ambient Temperature	297	K	Table 1
H_2 Tank Pressure	13.45	MPa	Table 1
H_2 Tank Volume	0.00363	m^3	Table 1
Leak Diameter	0.00356	m	Table 1
Discharge Coefficient-Orifice	0.75	N/A	Table 1

Table A-2 Schefer et al. [22] Figure 4 Input Parameters

Parameter	Value	Units	Location
Tank Temperature	290	K	Figure 4
Tank Pressure	43.1	MPa	Figure 4
Volume H_2	1234	L	Section 3.1
Leak Diameter	5.08	mm	Section 3.1

Table A-3 Proust et al. [23] Figure 4 Input Parameters

Parameter	Value	Units	Location
Orifice Diameter	2	mm	Figure 4
Tank Pressure	90	MPa	Section 2
Tank Volume	25	L	Proust Section 2.0 Page 2
Initial Tank Temperature	315.15	K	Table 1

Table A-4 Schefer et al. [24] Figure 3b Input Parameters

Parameter	Value	Units	Location
Tank Temperature	270	K	Section 2.1, range between 258–284
Tank Pressure	15.5	MPa	Section 2.1
Leak Diameter	3.175	mm	Figure 3
Volume H_2	0.98	m^3	Figure 3 via Riemann sum

A.2. Unignited Jets/Gas Plumes Input Parameters

Table A-5 Molkov [25] Table 5-3 Input Parameters

Original Authors	Temperature (K)	Pressure (bar)	Diameter (mm)	Location
Chaineaux et al.	207	3.6	6	Table 5-3
Chaineaux et al.	174	1.8	12	Table 5-3
Ruffin et al.	288	3.24	25	Table 5-3
Ruffin et al.	288	1.8	50	Table 5-3
Ruffin et al.	288	0.75	75	Table 5-3
Ruffin et al.	288	0.26	100	Table 5-3
Kuznetsov	287	16.1	0.25	Table 5-3
Kuznetsov	287	10.6	0.75	Table 5-3
Kuznetsov	287	9.7	1	Table 5-3
Kuznetsov	287	5.3	1	Table 5-3
Shirvill et al.	287	10	3	Table 5-3
Shirvill et al.	287	13.5	3	Table 5-3
Shirvill et al.	287	2.5	12	Table 5-3
Okabayashi et al.	288	20	2	Table 5-3
Okabayashi et al.	288	40	0.25	Table 5-3
Okabayashi et al.	288	40	0.5	Table 5-3
Okabayashi et al.	288	40	1	Table 5-3
Okabayashi et al.	288	40	2	Table 5-3
Veser et al.	298	5.43	1	Table 5-3
Veser et al.	80	2.99	1	Table 5-3
Veser et al.	298	1.01	2	Table 5-3
Veser et al.	80	1.81	2	Table 5-3

Table A-6 Houf and Schefer [10] Figure 5 Input Parameters

Parameter	Value	Units	Location
Density Exit	0.0838	kg/m^3	Table 1
Ambient Temperature	294	K	Section 2.1 [50]
Ambient Pressure	100	kPa	Section 5
Orifice Diameter	1.905	mm	Figure 5
Mass Flow Rate (Fr=268)	133.91	m/s	Table 1

Table A-7 Houf and Schefer [10] Figure 8 Input Parameters

Parameter	Value	Units	Location
Density Exit	0.0838	kg/m^3	Table 1
Ambient Temperature	273	K	Section 5
Ambient Pressure	100	kPa	Section 5
Orifice Diameter	1.905	mm	Figure 5
Mass Flow Rate (Fr=268)	133.91	m/s	Table 1

Table A-8 Houf and Schefer [10] Figure 9 Input Parameters

Parameter	Value	Units	Location
Density Exit	0.0838	kg/m^3	Table 1
Ambient Temperature	273	K	Section 5
Ambient Pressure	100	kPa	Section 5
Orifice Diameter	1.905	mm	Figure 5
Mass Flow Rate (Fr=268)	133.91	m/s	Table 1
Volumetric Flow Rate (Fr=268)	22.9	slm	Table 1
Mass Flow Rate (Fr=152)	76.02	m/s	Table 1
Volumetric Flow Rate (Fr=152)	13.08	slm	Table 1
Mass Flow Rate (Fr=99)	49.689	m/s	Table 1
Volumetric Flow Rate (Fr=99)	3.5	slm	Table 1

Table A-9 Ruggles and Ekoto [26] Figure 7 Input Parameters

Parameter	Value	Units	Location
Orifice Diameter	1.5	mm	Section 2.1
H_2 Pressure	983.2	kPa	Section 2.1, 10:1 pressure ratio (stagnation to ambient pressure) dynamic feedback was used to maintain a steady pressure ratio
Tank Temperature	295.4	K	Section 2.1
Discharge Coefficient	0.979	N/A	Section 2.1
Ambient Pressure	98.37	kPa	Section 2.1
Ambient Temperature	296	K	Section 2.1

Table A-10 Han et al. [27] Figure 3 Input Parameters

Sub-Figure	Parameter	Value	Units	Location
All	Orifice Diameter 1	0.5	mm	Figure 3
All	Orifice Diameter 2	0.7	mm	Figure 3
All	Orifice Diameter 3	1	mm	Figure 3
All	Initial H_2 Temperature	293	K	Section 3.2
A	Initial Pressure	100	bar	Figure 3a
B	Initial Pressure	200	bar	Figure 3b
C	Initial Pressure	300	bar	Figure 3c
D	Initial Pressure	400	bar	Figure 3d

Table A-11 Han et al. [27] Figure 6 Input Parameters

Sub-Figure	Parameter	Value	Units	Location
All	Initial Pressure 1	100	bar	Figure 6
All	Initial Pressure 2	200	bar	Figure 6
All	Initial Pressure 3	300	bar	Figure 6
All	Initial Pressure 4	400	bar	Figure 6
All	Initial H_2 Temperature	293	K	Section 3.2
A	Orifice Diameter	0.5	mm	Figure 6a
B	Orifice Diameter	0.7	mm	Figure 6b
C	Orifice Diameter	1	mm	Figure 6c

Table A-12 Han et al. [27] Figure 7 Input Parameters

Sub-Figure	Parameter	Value	Units	Location
All	Initial Pressure	300	bar	Figure 7
All	Initial H_2 Temperature	293	K	Section 3.2
A	Orifice Diameter	0.5	mm	Figure 7a
B	Orifice Diameter	0.7	mm	Figure 7b
C	Orifice Diameter	1	mm	Figure 7c

Table A-13 Han et al. [27] Figure 8 Input Parameters

Sub-Figure	Parameter	Value	Units	Location
All	Orifice Diameter	0.7	mm	Figure 8
All	Initial H_2 Temperature	293	K	Section 3.2
A	Initial Pressure	100	bar	Figure 8a
B	Initial Pressure	200	bar	Figure 8b
C	Initial Pressure	300	bar	Figure 8c
D	Initial Pressure	400	bar	Figure 8d

A.3. Ignited Jet Fires Input Parameters

Table A-14 Ekoto et al. [13] Table 2 Input Parameters

Parameter	Value	Units	Location
Flame 1			
Orifice Diameter	20.9	mm	Table 1
Mass Flow Rate	1	kg/s	Table 1
Initial Pressure	59.8	bar_g	Table 1
Initial Temperature	308.7	K	Table 1
Relative Humidity	94.3	%	Table 1
Ambient Temperature	280	K	Table 1
Ambient Pressure	1.022	bar	Table 1
Wind Speed	2.84	m/s	Table 1
Wind Angle	68.5	degrees	Table 1
Visible Flame Length	17.1	m	Table 1
Flame 2			
Orifice Diameter	52.5	mm	Table 1
Mass Flow Rate	7.4	kg/s	Table 1
Initial Pressure	62.1	bar_g	Table 1
Initial Temperature	287.8	K	Table 1
Relative Humidity	94.5	%	Table 1
Ambient Temperature	280	K	Table 1
Ambient Pressure	1.011	bar	Table 1
Wind Speed	0.83	m/s	Table 1
Wind Angle	34	degrees	Table 1
Visible Flame Length	45.9	m	Table 1

Table A-15 Schefer et al. [24] Figure 8 Input Parameters

Parameter	Value	Units	Location
Orifice Diameter	7.94	mm	Schefer and Houf [34]
Tank Temperature	270	K	Section 2.1, range between 258–284
5 s			
Exit Velocity	1233	m/s	Table 1
Volumetric Flow Rate	41026	slm	Table 1
Mass Flow Rate	57.3	g/s	Table 1
20 s			
Exit Velocity	1231	m/s	Table 1
Volumetric Flow Rate	16589	slm	Table 1
Mass Flow Rate	23.17	g/s	Table 1
40 s			
Exit Velocity	1078	m/s	Table 1
Volumetric Flow Rate	4954	slm	Table 1
Mass Flow Rate	6.92	g/s	Table 1
60 s			
Exit Velocity	644	m/s	Table 1
Volumetric Flow Rate	1482	slm	Table 1
Mass Flow Rate	2.07	g/s	Table 1
70 s			
Exit Velocity	446	m/s	Table 1
Volumetric Flow Rate	810	slm	Table 1
Mass Flow Rate	1.13	g/s	Table 1

Table A-16 Houf and Schefer [34] Figure 5 Input Parameters

Parameter	Value	Units	Location	Note
Initial Tank Pressure	2250	psi	Section 3.1	Range of 2000–2500 psi for tank pressure took the midpoint of 2250, blowdown over time
Orifice Diameter	7.94	mm	See note	Schefer and Houf [34]
Tank Temperature	294	K	Section 4	Temperature assumed in paper
Ambient Temperature	294	K	Section 4	Temperature assumed in paper

Table A-17 Houf and Schefer [34] Figure 6 Input Parameters

Parameter	Value	Units	Location	Note
Orifice Diameter	7.94	mm	See Note	Schefer and Houf [34]
Initial Tank Pressure	2250	psi	Section 3.1	Range of 2000–2500 psi for tank pressure, took the midpoint of 2250
Tank Temperature	294	K	Section 4	Temperature assumed in paper
Ambient Temperature	294	K	Section 4	Temperature assumed in paper
Pressure at 5 s	N/A	N/A	N/A	Use exit jet information
Exit Velocity	1233	m/s	Table 1	Schefer and Houf [34]
Volumetric Flow Rate	41026	slm	Table 1	Schefer and Houf [34]
Mass Flow Rate	57.3	g/s	Table 1	Schefer and Houf [34]

Table A-18 Imamura et al. [35] Table 2 Input Parameters

Parameter	Value	Units	Location
Data Set 1			
Orifice Diameter	1	mm	Figure 3
Spouting Pressure 1	1.09	MPa	Figure 3
Spouting Pressure 2	2.17	MPa	Figure 3
Spouting Pressure 3	3.26	MPa	Figure 3
Data Set 2			
Orifice Diameter	2	mm	Figure 3
Spouting Pressure 1	0.47	MPa	Figure 3
Spouting Pressure 2	0.93	MPa	Figure 3
Spouting Pressure 3	1.40	MPa	Figure 3
Spouting Pressure 4	1.87	MPa	Figure 3
Spouting Pressure 5	2.34	MPa	Figure 3
Spouting Pressure 6	2.80	MPa	Figure 3
Data Set 3			
Orifice Diameter	3	mm	Figure 3
Spouting Pressure 1	0.36	MPa	Figure 3
Spouting Pressure 2	0.73	MPa	Figure 3
Spouting Pressure 3	1.09	MPa	Figure 3
Spouting Pressure 4	1.46	MPa	Figure 3
Spouting Pressure 5	1.82	MPa	Figure 3
Spouting Pressure 6	2.19	MPa	Figure 3
Data Set 4			
Orifice Dia.	4	mm	Figure 3
Spouting Pressure 1	0.23	MPa	Figure 3
Spouting Pressure 2	0.47	MPa	Figure 3
Spouting Pressure 3	0.70	MPa	Figure 3
Spouting Pressure 4	0.94	MPa	Figure 3
Spouting Pressure 5	1.17	MPa	Figure 3
Spouting Pressure 6	1.41	MPa	Figure 3

Table A-19 Imamura et al. [35] Table 2 Input Parameters

Parameter	Value	Units	Location
Orifice Diameter	1.0, 2.0, 3.0, and 4.0	mm	Table 2
Spouting Pressure	0.36–3.26	MPa	Table 2

Table A-20 Mogi et al. [36] Figure 9 Input Parameters

Parameter	Value	Units	Location
Orifice Diameter 1	0.002	mm	Figure 9
Orifice Diameter 2	0.0008	mm	Figure 9
Orifice Diameter 3	0.0004	mm	Figure 9
Pressure	35	MPa	Section 3.3
Tank Volume	0.184	m^3	Section 2

Table A-21 Proust et al. [23] Figure 8 Input Parameters

Parameter	Value	Units	Location
Tank Pressure	90	MPa	Section 2
Tank Volume	25	L	Proust Section 2.0 Page 2
Initial Tank Temperature	315.15	K	Table 1
Orifice Diameter 1	3	mm	Figure 8
Orifice Diameter 2	2	mm	Figure 8
Orifice Diameter 3	1	mm	Figure 8

Table A-22 Proust et al. [23] Figure 10 Input Parameters

Parameter	Value	Units	Location
Orifice Diameter	2	mm	Figure 10
Tank Pressure	90	MPa	Figure 10
Tank Volume	25	L	Proust Section 2.0 Page 2
Initial Tank Temperature	315.15	K	Table 1
Flux number 1	(1, 1.41)	m	Figure 3
Flux number 2	(1.5,2.12)	m	Figure 3
Flux number 3	(2, 2.83)	m	Figure 3
Flux number 4	(3, 4.24)	m	Figure 3
Flux number 5	(4, 5.65)	m	Figure 3

A.4. Indoor Accumulation and Overpressure Input Parameters

Table A-23 Ekoto et al. [21] Figure 9 Input Parameters

Parameter	Value	Units	Location
Ambient Pressure	101325	Pa	Assumed
Ambient Temperature	297	K	Assumed
H_2 Tank Pressure	13450000	Pa	Table 1
H_2 Tank Temperature	297	K	Table 1
H_2 Tank Volume	0.00363	m^3	Table 1
Leak Diameter	0.00356	m	Table 1
Discharge Coefficient-Orifice	0.75	N/A	Table 1
Discharge Coefficient-Release	1	N/A	Assumed
Release Area	0.0171	m^2	Figure 2, Section 2.2
Release Height	0.2495	m	Figure 2, Section 2.2
Enclosure Height	2.72	m	Figure 2, Section 2.2
Floor/Ceiling Area	16.722	m^2	Figure 2, Section 2.2
Distance from Release to Wall	2.1255	m	Figure 2, Section 2.2
Angle of Release (0=Horizontal)	0	Radians	Picture
No Ventilation			
Vent 1 (Ceiling Vent) Cross-Sectional Area	0.00865	m^2	Table 3
Vent 1 (Ceiling Vent) Height from Floor	2.42	m	Picture
Vent 2 (Floor Vent) Cross-Sectional Area	0	m^2	Picture
Vent 2 (Floor Vent) Height from Floor	0	m	Picture
Vent Volumetric Flow Rate	0	m^3/min	Picture
With Ventilation			
Vent 1 (Ceiling Vent) Cross-Sectional Area	0.1	m^2	Table 3
Vent 1 (Ceiling Vent) Height from Floor	2.42	m	Picture
Vent 2 (Floor Vent) Cross-Sectional Area	0	m^2	Picture
Vent 2 (Floor Vent) Height from Floor	0	m	Picture
Vent Volumetric Flow Rate	6.5	m^3/min	Table 3

Table A-24 Ekoto et al. [21] Figure 9 Sensor Locations

Sensor	Location Coordinates	Units	Location
S04	(1.97, 1.25, 2.68)	(m, m, m)	Table and Figure 2: Ceiling location distances from vent
S08	(4.16, 1.27, 2.67)	(m, m, m)	Table and Figure 2: Ceiling location, distances from vent
S11	(4.15, 2.83, 2.68)	(m, m, m)	Table and Figure 2: Ceiling location, distances from vent
S04	(0.327, 0, 2.68)	(m, m, m)	Table and Figure 2: Ceiling location, in relation to release point
S08	(-1.86, 0, 2.67)	(m, m, m)	Table and Figure 2: Ceiling location, in relation to release point
S11	(-1.85, 1.58, 2.68)	(m, m, m)	Table and Figure 2: Ceiling location, in relation to release point

Table A-25 Ekoto et al. [21] Figure 14 Input Parameters

Parameter	Value	Units	Location
Ambient Pressure	101325	Pa	Assumed
Ambient Temperature	297	K	Assumed
H_2 Tank Pressure	13450000	Pa	Table 1
H_2 Tank Temperature	297	K	Table 1
H_2 Tank Volume	0.00363	m^3	Table 1
Leak Diameter	0.00356	m	Table 1
Discharge Coefficient-Orifice	0.75	N/A	Table 1
Discharge Coefficient-Release	1	N/A	Assumed
Release Area	0.0171	m^2	Figure 2, Section 2.2
Release Height	0.2495	m	Figure 2, Section 2.2
Enclosure Height	2.72	m	Figure 2, Section 2.2
Floor/Ceiling Area	16.722	m^2	Figure 2, Section 2.2
Distance from Release to Wall	2.1255	m	Figure 2, Section 2.2
Angle of Release (0=Horizontal)	0	Radians	Picture
Test 12			
Vent 1 (Ceiling Vent) Cross-Sectional Area	0.00368	m^2	Figure 14
Vent 1 (Ceiling Vent) Height from Floor	2.42	m	Figure 14
Vent 2 (Floor Vent) Cross-Sectional Area	0	m^2	Figure 14
Vent 2 (Floor Vent) Height from Floor	0	m	Figure 14
Vent Volumetric Flow Rate	0	m^3/min	Figure 14
Ignition Location	Near Forklift	N/A	Table 3
Ignition Delay	3	s	Table 3
Test 11			
Vent 1 (Ceiling Vent) Cross-Sectional Area	0.09716	m^2	Figure 14
Vent 1 (Ceiling Vent) Height from Floor	2.42	m	Figure 14
Vent 2 (Floor Vent) Cross-Sectional Area	0	m^2	Figure 14
Vent 2 (Floor Vent) Height from Floor	0	m	Figure 14
Vent Volumetric Flow Rate	0	m^3/min	Figure 14
Ignition Location	Near Forklift	N/A	Table 3
Ignition Delay	3	s	Table 3
Test 10			
Vent 1 (Ceiling Vent) Cross-Sectional Area	0.09716	m^2	Figure 14
Vent 1 (Ceiling Vent) Height from Floor	2.42	m	Figure 14
Vent 2 (Floor Vent) Cross-Sectional Area	0	m^2	Figure 14
Vent 2 (Floor Vent) Height from Floor	0	m	Figure 14
Vent Volumetric Flow Rate	0	m^3/min	Figure 14
Vent Volumetric Flow Rate	6.3	m^3/min	Figure 14
Ignition Location	Near Forklift	s	Table 3
Ignition Delay	3	m^2	Table 3

Table A-26 Giannissi et al. [37] Figure 7 Input Parameters

Parameter	Value	Units	Location
Ambient Pressure	101325	Pa	Assumed
Ambient Temperature	287	K	Assumed
H_2 Tank Pressure	1700000	Pa	Experimental Description
H_2 Tank Temperature	285	K	Experimental Description
H_2 Tank Volume	N/A	m^3	Mass Flow Controller used
Leak Diameter	0.00055	m	Experimental Description
Release Area	N/A	m^2	Hooker 2013 conference paper, H_2 released from leak diameter directly
Release Height	0.5	m	Experimental Description
Enclosure Height	2.5	m	Figure 1
Floor/Ceiling Area	12.5	m^2	Figure 1
Distance from Release to Wall	2.5	m	Figure 1 and abstract
Vent 1 (Ceiling Vent) Cross-Sectional Area	0.2241	m^2	Table 1
Vent 1 (Ceiling Vent) Height from Floor	2.13	m	Distance to the bottom of the vent
Vent 2 (Floor Vent) Cross-Sectional Area	N/A	m^2	Picture
Vent 2 (Floor Vent) Height from Floor	N/A	m	Picture
Angle of Release (0=Horizontal)	1.5708	Radians	Straight up, Figure 1
Vent Height	0.27	m	Figure 1
Vent Width	0.83	m	Figure 1
Vent Height from Floor (bottom)	2.13	m	Figure 1
Vent Height from Floor (middle)	2.265	m	Figure 1
Vent Height from Floor (top)	2.4	m	Figure 1

Table A-27 Merilo et al. [38] Figure 2 Overall Input Parameters

Parameter	Value	Units	Location
Ambient Pressure	101325	Pa	Assumed
Ambient Temperature	285	K	Assumed
H_2 Tank Pressure	N/A	Pa	Mass Flow Controller used
H_2 Tank Temperature	285	K	Assumed
H_2 Tank Volume	N/A	m^3	Mass Flow Controller used
Leak Diameter	0.00775	m	Section 2, page 3
Release Area	0	m^2	From figure 4, H_2 released from leak diameter directly
Enclosure Height	2.72	m	Section 2, page 2
Floor/Ceiling Area	22.204	m^2	Section 2, page 2
Distance from Release to Wall	0	m	depends on test, see below
Vent 1 (Ceiling Vent) Cross-Sectional Area	0.11	m^2	Section 2
Vent 1 (Ceiling Vent) Height from Floor	2.42	m	Section 2, center of vent
Vent 2 (Floor Vent) Cross-Sectional Area	0.11	m^2	Section 2
Vent 2 (Floor Vent) Height from Floor	0.17	m	Section 2, center of vent 0.08 meters to bottom of vent
Angle of Release (0=Horizontal)	1.5708	Radians	Vertical release, section 2 page 3 and figure 4
Ignition Delay	0	s	depends on test, see below

Table A-28 Merilo et al. [38] Figure 2 Sub-Figure Specific Input Parameters

Parameter	Value	Units	Location
Test 1 - Left			
Release Rate	9.22	kg/h	Table 2
Mass Released	3.07	kg	Table 2
Calculated Exit Velocity	688	m/s	Table 2
Release Duration	20	min	Table 2
Release Height	0.25	m	Table 2
Distance to Wall	4.85	m	Section 2
Vent Flow Rate	0	m^3/s	Table 2
Test 2 - Middle			
Release Rate	9.04	kg/h	Table 2
Mass Released	3.01	kg	Table 2
Calculated Exit Velocity	653	m/s	Table 2
Release Duration	20	min	Table 2
Release Height	1	m	Table 2
Distance to Wall	4.85	m	Section 2
Vent Flow Rate	0	m^3/s	Table 2
Test 3 - Right			
Release Rate	0.88	kg/h	Table 2
Mass Released	0.44	kg	Table 2
Calculated Exit Velocity	63	m/s	Table 2
Release Duration	30	min	Table 2
Release Height	1	m	Table 2
Distance to Wall	4.85	m	Section 2
Vent Flow Rate	0	m^3/s	Table 2

Table A-29 Merilo et al. [38] Figure 6a Input Parameters

Parameter	Value	Units	Location
Ambient Pressure	101325	Pa	Assumed
Ambient Temperature	285	K	Assumed
H_2 Tank Pressure	N/A	Pa	Mass Flow Controller used
H_2 Tank Temperature	285	K	Assumed
H_2 Tank Volume	N/A	m^3	Mass Flow Controller used
Leak Diameter	0.00775	m	Section 2, page 3
Release Area	0	m^2	From figure 4, H_2 released from leak diameter directly
Enclosure Height	2.72	m	Section 2, page 2
Floor/Ceiling Area	22.204	m^2	Section 2, page 2
Distance from Release to Wall	0	m	depends on test, see below
Vent 1 (Ceiling Vent) Cross-Sectional Area	0.11	m^2	Section 2
Vent 1 (Ceiling Vent) Height from Floor	2.42	m	Section 2, center of vent
Vent 2 (Floor Vent) Cross-Sectional Area	0.11	m^2	Section 2
Vent 2 (Floor Vent) Height from Floor	0.17	m	Section 2, center of vent 0.08 meters to bottom of vent
Angle of Release (0=Horizontal)	1.5708	Radians	Straight up, section 2 page 3 and figure 4
Ignition Delay	0	s	depends on test, see below
Release Rate	6.7	kg/h	Table 2
Mass Released	4.47	kg	Table 2
Calculated Exit Velocity	502	m/s	Table 2
Release Duration	40	min	Table 2
Release Height	0.25	m	Table 2
Distance to Wall	3.04	m	Section 2
Vent Flow Rate	0.1	m^3/s	Table 2

Table A-30 Bernard-Michel and Houssin-Agbomson [39] Figure 7 Input Parameters

Parameter	Value	Units	Location
Ambient Pressure	101325	Pa	Assumed
Ambient Temperature	286	K	Table 2
H_2 Tank Pressure	N/A	Pa	Mass Flow Controller
H_2 Tank Temperature	286	K	Mass Flow Controller
H_2 Tank Volume	N/A	m^3	Not Listed, 1E6 used in code
Leak Diameter 1	0.0272	m	Section 3.1
Leak Diameter 2	0.004	m	Section 3.1
Release Area	N/A	m^2	H_2 released from leak diameter directly
Release Height	0.27	m	Section 3.1
Enclosure Height	2.1	m	Section 3.1
Floor/Ceiling Area	0.9216	m^2	Section 3.1
Distance from Release to Wall	0.48	m	Section 3.1
Vent 1 (Ceiling Vent) Cross-Sectional Area	0.1862	m^2	Section 3.1
Vent 1 (Ceiling Vent) Height from Floor	1.7	m	Rough estimation
Vent 2 (Floor Vent) Cross-Sectional Area	0.1862	m^2	Section 3.1
Vent 2 (Floor Vent) Height from Floor	0.02	m	Figure 2
Vent Volumetric Flow Rate	0	m^3/s	Natural Vent
Angle of Release (0=Horizontal)	1.5708	Radians	Figure 1

Table A-31 Bernard-Michel and Houssin-Agbomson [39] Figure 9 Input Parameters

Parameter	Value	Units	Location
Parameter	Value	Units	Location
Ambient Pressure	101325	Pa	Assumed
Ambient Temperature	286	K	Table 2
H_2 Tank Pressure	N/A	Pa	Mass Flow Controller
H_2 Tank Temperature	286	K	Mass Flow Controller
H_2 Tank Volume	N/A	m^3	Not Listed, 1E6 used in code
Leak Diameter 1	0.0272	m	Section 3.1
Leak Diameter 2	0.004	m	Section 3.1
Release Area	N/A	m^2	H_2 released from leak diameter directly
Release Height	0.08	m	Section 3.1
Enclosure Height	1	m	Section 3.1
Floor/Ceiling Area	0.990025	m^2	Section 3.1
Distance from Release to Wall	0.4975	m	Section 3.1
Vent 1 (Ceiling Vent) Cross-Sectional Area	0.1728	m^2	Section 3.1
Vent 1 (Ceiling Vent) Height from Floor	0.75	m	Rough estimation
Vent 2 (Floor Vent) Cross-Sectional Area	0.1728	m^2	Section 3.1
Vent 2 (Floor Vent) Height from Floor	0.02	m	Figure 2
Vent Volumetric Flow Rate	0	m^3/s	Natural Vent
Angle of Release (0=Horizontal)	1.5708	Radians	Figure 1

A.5. Cryogenic Hydrogen Input Parameters

A.5.1. Blowdown

Table A-32 Friedrich et al. [42] Dataset Input Parameters

Graph	Pressure (bar)	Temperature (K)	Diameter (mm)	Location
A	5	80	1	Directly from dataset, see Tables 2 and 3
B	20	80	1	Directly from dataset, see Tables 2 and 3
C	100	80	1	Directly from dataset, see Tables 2 and 3
D	200	80	0.5	Directly from dataset, see Tables 2 and 3
E	200	80	1	Directly from dataset, see Tables 2 and 3
F	200	80	2	Directly from dataset, see Tables 2 and 3
G	200	80	4	Directly from dataset, see Tables 2 and 3
H	200	300	1	Directly from dataset, see Tables 2 and 3

A.5.2. Unignited Jet Plumes

Table A-33 Xiao et al. [40] Figure 3 Input Parameters

Case	Pressure (bar)	Temperature (K)	Diameter (mm)	Location
1	17	298	2	Table 1
2	68.5	298	1	Table 1
3	8.25	80	2	Table 1
4	32	80	1	Table 1

Table A-34 Friedrich et al. [41] Figure 5 Input Parameters

Experiment number	Pressure (bar)	Temperature (K)	Diameter (mm)	Location
3000	19	37	1	Table 1
3002	15	38	1	Table 1
3004	29	36	1	Table 1
3005	18	36	1	Table 1
5001	29.85	43.59	0.5	Table 1
5002	29.85	43.59	0.5	Table 1

Note that the below graph location numbers are from Figures 3-26 and 3-27 in the main body of the report in conventional matrix notation.

Table A-35 Hecht and Panda [44] Figure 10 Input Parameters

Graph Location Number	Pressure (bar)	Temperature (K)	Diameter (mm)	Location
11	2	58	1	Table 1
12	3	56	1	Table 1
13	4	53	1	Table 1
21	5	50	1	Table 1
22	2	61	1.25	Table 1
23	2.5	51	1.25	Table 1
31	3	51	1.25	Table 1
32	3.5	55	1.25	Table 1
33	4	54	1.25	Table 1
41	4	45	1.25	New data
42	2	58	1	New data
43	2	82	1	New data
51	2.5	55	1	New data
52	3	40	1	New data
53	3	63	1	New data

Refer to Table A-32 for the Friedrich et al. [42] input parameters, they are the same for both blowdown and jet plumes.

A.5.3. Ignited Jet Fires

Table A-36 Panda and Hecht [43] Table 3 Input Parameters

Test ID	Pressure (bar-gauge)	Temperature (K)	Diameter (mm)	Location
1	2	163	0.75	Table 3
2	5	179	0.75	Table 3
3	6	205	0.75	Table 3
4	2	215	0.75	Table 3
5	2	46	1.0	Table 3
6	2	55	1.0	Table 3
7	2	62	1.0	Table 3
8	4	78	1.0	Table 3
9	5	81	1.0	Table 3
10	3	113	1.0	Table 3
11	4	124	1.0	Table 3
12	2	127	1.0	Table 3
13	3	163	1.0	Table 3
14	3	175	1.0	Table 3
15	6	295	1.0	Table 3
16	2	46	1.25	Table 3
17	2	53	1.25	Table 3
18	2	64	1.25	Table 3
19	3	70	1.25	Table 3
20	5	91	1.25	Table 3
21	2	144	1.25	Table 3
22	5	155	1.25	Table 3
23	2	185	1.25	Table 3
24	6	200	1.25	Table 3
25	5	272	1.25	Table 3

A.6. Unconfined Overpressure Input Parameters

Table A-37 Bauwens and Dorofeev [18] Figure 9 Input Parameters

Parameter	Value	Units	Location
20mm Nozzle			
Orifice Diameter	19.05	mm	Figure 9
Orifice Temperature	300	K	Section 3.1
Orifice Pressure	6E+6	Pa	Section 3.1
Ambient Temperature	297	K	Section 3.1
Ambient Pressure	101325	Pa	Assumed
Locations	(11.319, 0, 0) (20.685, 0, 0)	m	Figure 9
50mm Nozzle			
Orifice Diameter	50.8	mm	Figure 9
Orifice Temperature	300	K	Section 3.1
Orifice Pressure	6E+6	Pa	Section 3.1
Ambient Temperature	297	K	Section 3.1
Ambient Pressure	101325	Pa	Assumed
Locations	(12.925, 0, 0) (20.685, 0, 0)	m	Figure 9

Table A-38 Kobayashi et al. [45] Figure 8 Input Parameters

Parameter	Value	Units	Location
Orifice Diameter	0.7	mm	Figure 8
Orifice Temperature	65	K	Figure 8
Orifice Pressure	5.91E+7	Pa	Figure 8
Ambient Temperature	297	K	Assumed
Ambient Pressure	101325	Pa	Assumed
Locations	(1.0, 0, 0) (1.5, 0, 0) (2.0, 0, 0) (3.0, 0, 0) (3.9, 0, 0) (4.5, 0, 0) (6.5, 0, 0) (10.5, 0, 0)	m	Figure 8

Table A-39 Kobayashi et al. [45] Table 1 Input Parameters (orifice properties and locations provided in Table 3-10)

Parameter	Value	Units	Location
Ambient Temperature	297	K	Assumed
Ambient Pressure	101325	Pa	Assumed

Table A-40 Royle and Willoughby [46] Table 1 Input Parameters (orifice diameters provided in Table 3-11)

Parameter	Value	Units	Location
Orifice Temperature	293.15	K	Section 3
Orifice Pressure	2.05E+7	Pa	Table 1
Ambient Temperature	297	K	Assumed
Ambient Pressure	101325	Pa	Assumed
Locations	(2.8, 1.5, 0.5)	m	Figure 1

Table A-41 Huéscar Medina et al. [48] Figure 148 Input Parameters

Parameter	Value	Units	Location
Orifice Diameter	25.4	mm	Section 3
Tank Phase	Liquid	–	Section 5
Orifice Pressure	3.543E+5	Pa	Table 13
Ambient Temperature	275.15	K	Figure 127
Ambient Pressure	101325	Pa	Assumed
Locations	(5, 1.2, -5) (5, 1.2, -10) (5, 1.2, -15) (21, 1.2, -5) (21, 1.2, -10) (21, 1.2, -15)	m	Table 12

Table A-42 Jallais et al. [19] Figure 22 & Table 2 Input Parameters

Parameter	Value	Units	Location
20.9mm Nozzle			
Orifice Diameter	20.9	mm	Table 1
Orifice Temperature	279.45	K	Table 1
Orifice Pressure	6.101E+6	Pa	Section "DNV GL Experiment" [19]
Ambient Temperature	297.45	K	Table 1
Ambient Pressure	101325	Pa	Assumed
Locations	(10, 0, 0) (20, 0, 0)	m	Table 2
52.5mm Nozzle			
Orifice Diameter	52.5	mm	Table 1
Orifice Temperature	279.95	K	Table 1
Orifice Pressure	6.101E+6	Pa	Section "DNV GL Experiment" [19]
Ambient Temperature	279.95	K	Table 1
Ambient Pressure	101325	Pa	Assumed
Locations	(5.074, 0, 0) (6.134, 0, 0) (7.416, 0, 0) (9.380, 0, 0) (10.645, 0, 0) (11.652, 0, 0) (12.638, 0, 0) (13.709, 0, 0) (15.140, 0, 0) (17.653, 0, 0) (19.496, 0, 0) (21.339, 0, 0) (24.213, 0, 0) (26.984, 0, 0) (35.698, 0, 0) (47.227, 0, 0) (59.185, 0, 0) (88.051, 0, 0) (124.089, 0, 0) (164.166, 0, 0) (200.238, 0, 0) (31.459, 0, 0) (75.183, 0, 0) (107.400, 0, 0) (10, 0, 0) (20, 0, 0)	m	Table 2 + Figure 22

Table A-43 Takeno et al. [47] Figures 13 & 16 Input Parameters, 1.0 & 2.0mm Nozzles

Parameter	Value	Units	Location
1.0mm Nozzle			
Orifice Diameter	1	mm	Figure 13
Orifice Temperature	297	K	Assumed
Orifice Pressure	4e+7	Pa	Figure 13
Ambient Temperature	297	K	Assumed
Ambient Pressure	101325	Pa	Assumed
Locations	(2.991, 0, 0) (3.148, 0, 0) (4.539, 0, 0) (6.497, 0, 0) (6.451, 0, 0) (10.770, 0, 0) (15.872, 0, 0) (28.301, 0, 0) (30.010, 0, 0) (48.672, 0, 0)	m	Figure 13
2.0mm Nozzle			
Orifice Diameter	2	mm	Figure 13
Orifice Temperature	297	K	Assumed
Orifice Pressure	4e+7	Pa	Figure 13
Ambient Temperature	297	K	Assumed
Ambient Pressure	101325	Pa	Assumed
Locations	(2.467, 0, 0) (2.362, 0, 0) (3.663, 0, 0) (5.641, 0, 0) (5.642, 0, 0) (9.987, 0, 0) (15.158, 0, 0) (27.667, 0, 0) (29.769, 0, 0) (48.279, 0, 0)	m	Figure 13

Table A-44 Takeno et al. [47] Figures 13 & 16 Input Parameters, 5.0 & 10.0mm Nozzles

Parameter	Value	Units	Location
5.0mm Nozzle			
Orifice Diameter	5	mm	Figure 13
Orifice Temperature	297	K	Assumed
Orifice Pressure	4e+7	Pa	Figure 13
Ambient Temperature	297	K	Assumed
Ambient Pressure	101325	Pa	Assumed
Locations	(1.745, 0, 0) (2.190, 0, 0) (5.006, 0, 0) (8.000, 0, 0) (10.036, 0, 0) (18.292, 0, 0) (26.006, 0, 0) (45.420, 0, 0)	m	Figure 13
10.0mm Nozzle			
Orifice Diameter	10	mm	Figure 16
Orifice Temperature	297	K	Assumed
Orifice Pressure	4e+7	Pa	Figure 16
Ambient Temperature	297	K	Assumed
Ambient Pressure	101325	Pa	Assumed
Locations	(2.177, 0, 0) (2.205, 0, 0) (2.134, 0, 0) (2.307, 0, 0) (3.900, 0, 0) (3.950, 0, 0) (3.873, 0, 0) (8.374, 0, 0) (8.319, 0, 0) (8.317, 0, 0) (13.340, 0, 0) (13.520, 0, 0) (13.438, 0, 0) (14.529, 0, 0) (30.350, 0, 0) (45.618, 0, 0)	m	Figure 16

DISTRIBUTION

Email—Internal

Name	Org.	Sandia Email Address
Ethan Hecht	8367	ehecht@sandia.gov
Kristin Hertz	8367	klhertz@sandia.gov
Brian Ehrhart	8854	bdehrha@sandia.gov
Chris LaFleur	8854	aclafle@sandia.gov
Michael Devin	8921	mcdevin@sandia.gov
Technical Library	1911	sanddocs@sandia.gov

Email—External

Name	Company Email Address	Company Name
Laura Hill	laura.hill@ee.doe.gov	DOE EERE HFTO
Christine Watson	christine.watson@ee.doe.gov	DOE EERE HFTO

This page intentionally left blank.

This page intentionally left blank.



Sandia National Laboratories is a multimission laboratory managed and operated by National Technology & Engineering Solutions of Sandia LLC, a wholly owned subsidiary of Honeywell International Inc., for the U.S. Department of Energy's National Nuclear Security Administration under contract DE-NA0003525.